STARS

Electronic Theses and Dissertations, 2004-2019

2014

Cascaded plasmon resonances for enhanced nonlinear optical response

Seyfollah Toroghi

University of Central Florida

Showcase of Text, Archives, Research & Scholarship

CASCADED PLASMON RESONANCES FOR ENHANCED NONLINEAR OPTICAL RESPONSE

by

SEYFOLLAH TOROGHI
B.S. University of Tabriz, Iran, 2002
M.S. University of Shahid Beheshti, Iran, 2005

A dissertation submitted in partial fulfillment of the requirements
for the degree of Doctor of Philosophy
in College of Optics and Photonics, CREOL,
at the University of Central Florida
Orlando, Florida

Fall Term
2014

Major Professor: Pieter G. Kik

ABSTRACT

The continued development of integrated photonic devices requires low-power, small volume all-optical modulators. The weak nonlinear optical response of conventional optical materials requires the use of high intensities and large interaction volumes in order to achieve significant light modulation, hindering the miniaturization of all-optical switches and the development of lightweight transmission optics with nonlinear optical response. These challenges may be addressed using plasmonic nanostructures due to their unique ability to confine and enhance electric fields in sub-wavelength volumes. The ultrafast nonlinear response of free electrons in such plasmonic structures and the fast thermal nonlinear optical response of metal nanoparticles, as well as the plasmon enhanced nonlinear Kerr-type response of the host material surrounding the nanostructures could allow ultrafast all-optical modulation with low modulation energy.

In this thesis, we investigate the linear and nonlinear optical response of engineered effective media containing coupled metallic nanoparticles. The fundamental interactions in systems containing coupled nanoparticles with size, shape, and composition dissimilarity, are evaluated analytically and numerically, and it is demonstrated that under certain conditions the achieved field enhancement factors can exceed the single-particle result by orders of magnitude in a process called cascaded plasmon resonance. It is demonstrated that these conditions can be met in systems containing coupled nanospheres, and in systems containing non-spherical metal nanoparticles that are compatible with common top-down nanofabrication methods such as electron beam lithography and nano-imprint lithography. We show that metamaterials based on

such cascaded plasmon resonance structures can produce enhanced nonlinear optical refraction and absorption compared to that of conventional plasmonic nanostructures. Finally, it is demonstrated that the thermal nonlinear optical response of metal nanoparticles can be enhanced in carefully engineered heterogeneous nanoparticle clusters, potentially enabling strong and fast thermal nonlinear optical response in system that can be produced in bulk through chemical synthesis.

This work is dedicated to my family, specially my parents,

for their love, support, and encouragement.

ACKNOWLEDGEMENTS

TABLE OF CONTENTS

LIST OF FIGURES

xvi

1. INTRODUCTION

The invention of the laser in 1960 [1] opened the opportunity to experimentally observe nonlinear optical phenomena, starting with the generation of second harmonic radiation inside a quartz crystal illuminated by ruby laser in 1961[2]. Nonlinear optical phenomena occur when the electronic motion in the material in the presence of a strong electromagnetic field is not just linearly related to the strength of the electric field, and instead higher nonlinear orders of the material susceptibility are required to describe the electronic motion [3]. One of the important accomplishments of nonlinear optics is the ability to control light using light itself at the same frequency, through effects known as nonlinear absorption and refraction as a result of the optical Kerr effect or the photo-thermal effect. The optical Kerr effect occurs when a strong optical field causes a near-instantaneous modification in the refractive index of the material. The photo-thermal effect on the other hand occurs when optical absorption increases the temperature inside a material leading to a modification in the refractive index of the material. The optical Kerr effect is typically weak, requiring the use of extremely strong excitation fields which can be achieved using short high-energy pulses [4, 5], spatial focusing of high-power beams [6], and field enhancement in dielectric resonators such as fiber Bragg gratings [7], fiber ring resonators [8], microdisk resonators[9], and photonic crystal cavities[10].

An alternative way of achieving enhanced electric fields and subsequently enhanced absorption and scattering is the use of plasmon resonant metallic nanostructures. In recent years, metallic nanoparticles have attracted enormous attention due to their ability to convert far-field radiation to the localized and strong external and internal fields in the vicinity of their surfaces.

This occurs through the coupling of the incident electromagnetic field to oscillating free-electrons near the metal surface, called *localized surface plasmons*. Strongly enhanced and confined near-fields in plasmonic nanoparticles can improve the performance of many photonic applications such as optical scattering spectroscopy [11-14], chemical and biological sensing [15-18], high resolution imaging [19, 20], ultrafast and compact photo-detectors [21, 22] and modulators [23-25], light emitters [26, 27], solar cells [28, 29], photo-thermal imaging [30-32], optoacoustic imaging[33, 34], photo-thermal therapy and drug delivery [35-42], nano-welding [43, 44] and nonlinear optical phenomena [25, 45-73].

The strong field enhancement inside the metal and in the vicinity of the plasmonic nanoparticle can enhance the nonlinear optical response of a medium in which the inherent nonlinearity is very small, resulting in enhanced effective electronic susceptibilities. Such effects have already been investigated in randomly distributed metallic nanoparticles on films [45, 46], metallic thin films [47-51], metallic aggregates [52-55], metallic gratings [25, 56], metallic nano-patterned arrays [57-67], metallic tips [68, 69] and metallic nanoparticles [70-73]. In addition to enhancing Kerr-type nonlinear susceptibilities, the presence of strong field enhancement inside and around plasmonic nanoparticles can also introduce strong power dissipation and heat generation. Plasmon resonant nanoparticles can therefore also be used as nanoscale heat generators. Nanoscale heat generation using metallic nanoparticles has found applications in photothermal imaging [30-32], optoacoustic imaging [33, 34], biophotonics [35-42], bubble formation for nanosurgery [74-78] and purifying liquids[79, 80], material growth [81], nano-welding [43, 44], heat-assisted magnetic recording[82] and photothermal control of fluidics[83,

84]. This enhanced and localized absorption corresponding abrupt temperature changes could produce a large photothermal response in short time scales.

In this thesis, we study the linear and nonlinear optical response of media containing coupled metallic nanoparticles, initially with a focus on producing large field enhancement (Chapters 2,3 and 5), and ultimately determining non-linear optical performance of materials with Kerr type response (Chapter 4) and photothermal response (chapter 6). The following sections briefly describe the fundamental concepts needed to gain a thorough understanding of the work presented in this thesis.

1.1. Nonlinear optical response

Light-matter interaction can be described by the induced polarization in the material due to the electric field of the light. In the case of weak optical fields, the induced polarization is linearly dependent on the electric field strength. However in the case of strong optical fields, higher order susceptibilities are required to achieve an accurate description of the induced polarization, which in the case of instantaneous nonlinear response leads to a polarization of the form $\boldsymbol{P}(t) = \varepsilon_0[\chi^{(1)}\boldsymbol{E}(t) + \chi^{(2)}\boldsymbol{E}(t)\boldsymbol{E}(t) + \chi^{(3)}\boldsymbol{E}(t)\boldsymbol{E}(t)\boldsymbol{E}(t)],$ as described in more detail in appendix A. Generally, the optical response of matter includes linear polarization which is responsible for linear refractive index, second order nonlinear polarization which leads to processes such as second harmonic generation (SHG), sum and difference frequency generation, optical rectification and optical parametric amplification and oscillation, and the third order nonlinear polarization which involves processes like third harmonic generation, four-wave mixing, nonlinear refraction and

absorption. Higher order polarizations (4th, 5th,…) can be induced in matter, however the corresponding optical response is typically weak and consequently they have few applications.

Generally, a nonlinear medium can develop a nonlinear response at new frequencies that are not present in the incident field, as well as at the original frequency of the incident wave. The latter effect follows from third order nonlinear response which is the lowest-order nonlinear term in macroscopically centrosymmetric and isotropic media. If we consider only nonlinear interactions that produce a polarization response at the same frequency as the incident field, the induced susceptibility in a nonlinear medium depends on the square of the electric field which leads to an irradiance-dependent refractive index in the presence of the strong optical fields. This nonlinear effect causes several phenomena such as self-phase modulation and cross-phase modulation, optical phase conjugation, optical bistability, optical switching and optical limitation. For a more detailed description of nonlinear refraction, see Appendix A.

An irradiance-dependent refractive index not only occurs in optical materials with third-order nonlinear susceptibility, but also in materials with thermal nonlinear optical response. In these materials the refractive index changes as the temperature is raised due to absorbed optical power. The induced refractive index change related to the thermal nonlinear optical response is often larger than the Kerr-type nonlinear optical response. However, the response time of Kerr-type nonlinearities is much shorter than that of optical thermal nonlinearity, which make Kerr-type nonlinear response more appealing in ultrafast nonlinear optical applications.

1.2. Localized Surface Plasmons

Both Kerr-type nonlinear optical response and thermal nonlinear optical response can be modified by structures that enhance the optical field strength. One way to achieve enhanced optical fields is through the use of surface plasmons. Surface plasmons are collective charge density oscillations near the interface of a metal and a dielectric or vacuum due to the coupling of the electromagnetic field to the metal's free charges. Surface plasmons can exist as propagating modes at planar metal-dielectric interfaces, called propagating surface plasmons or surface plasmon polaritons (SPP), as well as on metal nanoparticles, where they are typically referred to as localized surface plasmons [85]. In this thesis, we discuss only the latter type of the surface plasmons.

Free electrons in a metal nanoparticle can be moved from their equilibrium configuration by the electric field of an incident optical wave, inducing positive and negative surface charge on opposing sides of the nanoparticle. An electric field will develop inside the nanoparticle due to the charge cloud displacement which leads to a restoring force on the free electrons. The free electrons will oscillate under this restoring force at their natural oscillation frequency. This type of localized surface plasmon resonance mode can be optically excited when the frequency of the incident light matches this natural oscillation frequency. A schematic representation of a localized surface plasmon on a metal nanosphere is presented in Figure 1.1, showing an electromagnetic wave propagating to right. The maximum electron cloud displacement is seen to occur with a 90 degree phase delay compared to the force applied by the incident electromagnetic field.

The resonance frequency of the localized surface plasmon oscillation depends on different parameters such as the dielectric function of the metal and of the material surrounding the metal, the nanoparticle shape, and the nanoparticle size [86].
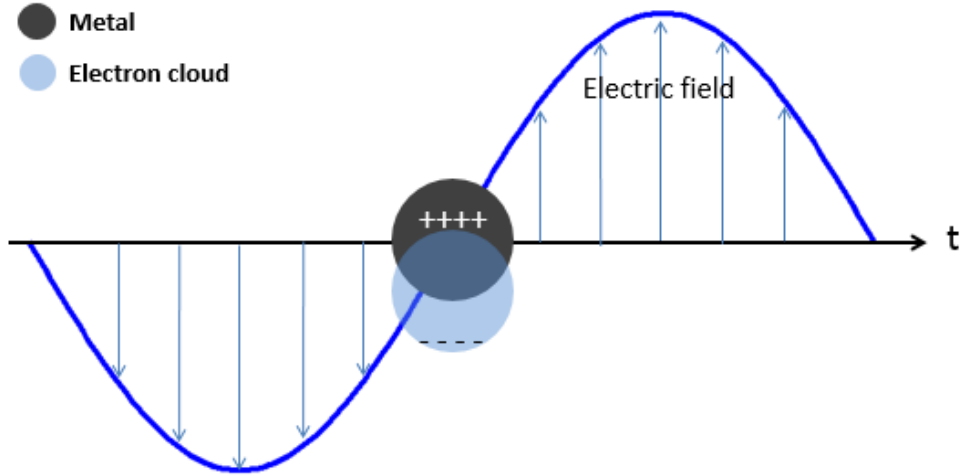
Figure 1.1: Schematic diagram of a localized plasmon oscillation for a metal nanosphere under illumination at the localized plasmon resonance frequency.

As mentioned before, two key features of surface plasmons is their ability to confine electromagnetic energy in volumes, around $(100 \text{ nm})^3$, smaller than the diffraction limit $(\lambda_0/2n_0)^3$, around $(200 \text{ nm})^3$ in glass in visible range, and to enhance the electric component of incident light. For a sphere illuminated by an optical field in quasi-electrostatic limit, a dipolar resonance occurs at frequencies where $\varepsilon_m(\omega) \approx -2\varepsilon_h(\omega)$, known as the localized surface plasmon resonance frequency. Here $\varepsilon_m(\omega)$ and $\varepsilon_h(\omega)$ are the frequency-dependent dielectric function of the metal and the surrounding material, respectively. At this frequency both internal and external electric fields will be enhanced. The ratio of the plasmon enhanced electric field and the incident electric field is

called the field enhancement factor in plasmonic nanostructures, which for isolated spherical noble metal particles can reach values as high as 40. The dipolar plasmon resonance mode typically occurs at frequencies ranging from the ultraviolet to the visible for metals.

The quasi-electrostatic regime ceases to be valid when the size of nanoparticle becomes either too large or too small. In the large nanoparticle case, phase retardation leads to the excitation of higher order plasmon modes while the skin depth limits the penetration of the electromagnetic field into the particle. On the other hand, when the nanoparticle size becomes similar to or smaller than the electron mean free path, additional electron scattering from the surface of nanoparticle introduces additional dissipative loss in the metal (details in appendix B). To illustrate these effects Figure 1.2 shows the electric field enhancement factors for silver nanoparticles with different sizes calculated by a finite integration method [87], in which the dielectric function of silver nanoparticles has been described using the modified Drude model used in Chapter 4. Larger metal nanoparticles show a redshift of the resonance frequency and an increase in the resonance linewidth, which is the combined result of the reduced field penetration at larger sizes and the appearance of the higher order plasmon modes as described above. Very small nanoparticles on the other hand show a highly damped plasmon resonance due to the increased electron scattering described above. Consequently, an optimum particle size exists for maximizing the strength of the surface plasmon resonance of isolated metal nanoparticles.
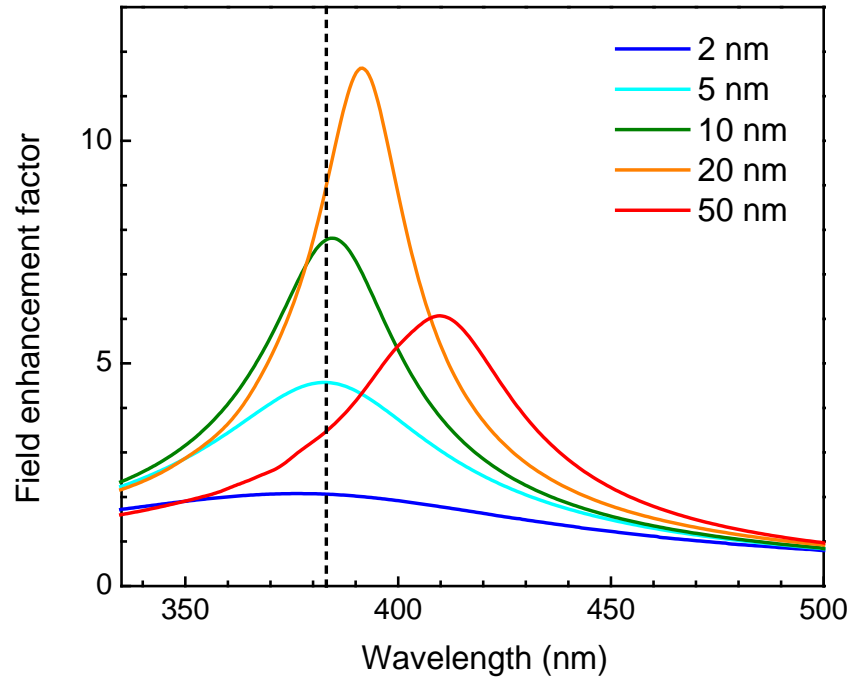
Figure 1.2: Simulated internal field enhancement in silver nanoparticles in water (n=1.33). The dashed black line shows the predicted plasmon resonance wavelength of this system in the quasi-electrostatic regime.

While isolated spherical nanoparticles can produce large field enhancement factors, field enhancement factors can be further increase by using electromagnetic far-field and near-field interactions between closely spaced nanoparticles. The origin of this additional field enhancement can be understood from the viewpoint of coupled resonators. For closely spaced particles the response of one particle can be affected by the electric fields associated with a nearby particle with an oscillating dipole moment. This can lead to resonance frequency shifts, the excitation of multipolar plasmon modes, and strongly modified field enhancement factors [88-93]. A more detailed description of coupled modes in nanoparticle clusters in the point-dipole limit can be

found in appendix B. When introducing size differences in coupled nanoparticles, modified resonance shifts and larger field enhancement factors can be obtained, in an effect called 'cascaded plasmon resonance' [89, 94, 95].

1.3. Localized Plasmon Enhanced Nonlinear Effects

The strong localized electric field that develops inside and around the metallic nanoparticle when excited at the plasmon resonance frequency can nonlinearly change the refractive index of the particle itself and of the surrounding medium, through Kerr-type third-order nonlinearity. The plasmon-enhanced modification of the refractive index of the metal or the host material leads to modified dipole moments and a shift in the frequency at which the dipolar localized plasmon resonance condition where $\varepsilon_m(\omega) = -2\varepsilon_h(\omega)$ is satisfied. These coupled effects appear as an enhanced modification of the Kerr-type nonlinear optical response of the nanostructure. In addition to Kerr-type nonlinear optical response, temperature changes inside and around the nanoparticles due to heat dissipation at frequencies near the plasmon resonance may introduce an additional thermal nonlinear optical response in the plasmonic nanostructures. The heating and temperature evolution responsible for these nonlinearities follows three steps in metallic nanoparticles. In the first step, optical absorption under illumination of the structure heats the free electron gas through electron-electron scattering on a time scale of ~100 fs[96]. The increased electron temperature leads to a non-equilibrium electron energy distribution function, an effect known as Fermi smearing, resulting in an ultrafast nonlinear optical response[55, 97-99]. In the second step, the hot electron gas exchanges energy with the relatively cold metal lattice through electron-phonon

scattering on a time scale of picoseconds[100] which leads to a thermal equilibration of the electronic and vibrational temperature in the metallic nanoparticle. In the final step, the heat diffuses from the hot metallic nanoparticle to the cooler medium surrounding the nanoparticle over hundreds of picoseconds, depending on the thermal conductivity of surrounding medium. This is a notably short time for a thermal effect as a result of the highly confined heat generation and the large surface-to-volume ratio of typical nanometric plasmonic structure, which might allow the use of plasmon-mediated thermal nonlinear optical effects for fast (ps) switching applications.

1.4. Effective Medium Theory

Individual plasmonic nanoparticles can produce enhanced nonlinear response, however to achieve a large nonlinear optical response, interaction of incident light with many such resonant particles may be required. The modeling of the optical response in such cases requires methods that can describe light propagation in complex inhomogeneous media. This can be done using effective medium theory, EMT, provided that the largest feature sizes in the inhomogeneous medium are much smaller than the wavelength of the light in that medium, as shown in Figure 1.3. In fact, the concept of a refractive index itself can be considered an effective medium theory, since it disregards the atomic structure of materials.
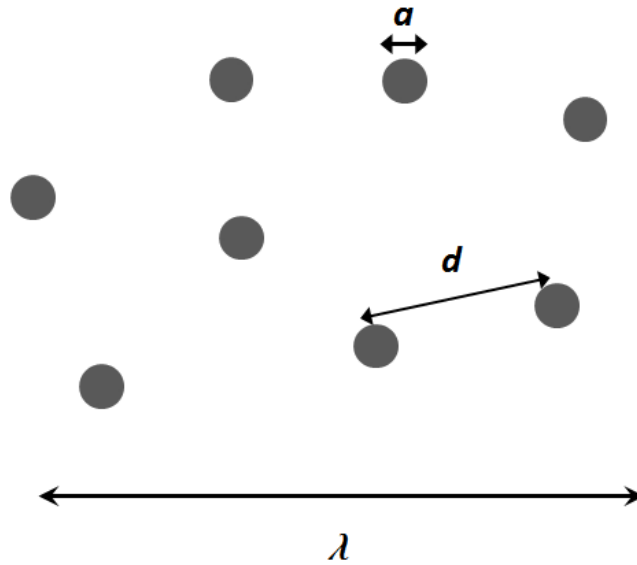
Figure 1.3: Length scales for an effective medium composed of embedded nanoparticles in a host medium, where *a* and *d* are particle size and interparticle spacing, respectively. For effective medium theory to apply, both are required to be much smaller than the wavelength λ of the incident light.

Effective medium theory has been widely used to describe the linear and nonlinear optical properties of nanocomposites [52, 67]. EMT describes the complex and inhomogeneous structure as a homogeneous medium with an effective linear and nonlinear refractive index. Broadly, effective medium theory calculates the average polarization inside an inhomogeneous medium and compares it to the average electric field in this medium. From the ratio of these two quantities an effective susceptibility can be derived. A related approach considers the average energy dissipation in a medium and compares it to the average energy density in the medium to extract an effective refractive index. Two well-known analytical effective medium approximations are the Maxwell-

Garnett model and the Bruggeman model. These assume approximately spherical inclusions, and are therefore not generally applicable. A detailed description and calculation of optical properties using effective medium theory related to the approaches taken in this Thesis is provided in appendix C.

1.5. This Thesis

In this Thesis we analytically and numerically investigate the conditions to achieve large electric field enhancement factors in coupled metallic nanoparticle structures and their potential use in improving the Kerr-type and thermal nonlinear optical response when used as building blocks for nonlinear optical effective media.

In Chapter 2, we theoretically discuss the governing rules in the optical response of the size-symmetric and size-asymmetric dimer structures using a point dipole interaction model. The field enhancement factors of nanoparticle dimers are evaluated as a function of the particle size difference and inter-particle spacing, showing distinct regimes of field enhancement that are labeled hindered cascading and multiplicative cascading. A formula is derived for the ultimate limit of the field enhancement in such coupled asymmetric dimers. We show that a maximum internal field enhancement of 2.9×10^3, a factor of 75 larger than that of an isolated silver nanoparticle, can be achieved. Such coupling effects can be used to enhance the Kerr type nonlinear response and thermal nonlinear optical response, as discussed in later chapters.

In Chapter 3, we discuss control of the near-field coupling between plasmon resonant nanoparticles using the shape of the individual nanoparticles. We demonstrate that cascaded

plasmon resonances can be achieved in coupled ellipsoidal particles with identical thickness which leads to cascaded antenna designs that are compatible with common top-down nanofabrication methods such as electron beam lithography and nano-imprint lithography. We evaluate field enhancement factors as a function of the particle volume ratio and spacing and find that strong cascaded field enhancement can be achieved in planar antenna structures.

In Chapter 4, we take the elements discussed in prior chapters and theoretically study the linear and nonlinear optical responses of a plasmonic metamaterial consisting of closely spaced nanoparticles with different sizes, using the finite integration method [87] and effective medium theory. We show that the effective nonlinear absorption in such structures can be controlled and enhanced by the interplay between different plasmon resonance modes. By varying the size difference between adjacent particles, it is shown that the plasmonic nanostructure can be gradually adjusted from the non-cascaded to the cascaded coupling regime, leading to an enhanced nonlinear susceptibility and figure of merit for nonlinear absorption.

In Chapter 5, we analytically and numerically describe the optical response of heterogeneous plasmonic trimer structures composed of a silver nanoparticle dimer and a central gold nanoparticle. We use a point dipole model to show that the plasmon resonance of the silver dimer can be controlled through near-field coupling, allowing for a frequency overlap of the plasmon resonance of the silver dimer and the gold monomer. The resulting coupled plasmon resonance in the heterogeneous trimer structure is found to lead to an enhanced energy dissipation per unit volume which exceeds that of a single-particle system by two orders of magnitude. This

enhanced energy dissipation may have practical applications in photothermal therapy, fast thermal nonlinear optical modulation, and could enable new thermal studies at picosecond time scales.

In Chapter 6, we numerically investigate the thermal nonlinear optical response of composite plasmonic nanostructures using full-field three-dimensional electromagnetic and transient thermal calculations. We demonstrate that in addition to the magnitude of the field enhancement and related heat dissipation, the specific location where heat is generated has a major impact on the attainable temperature changes and thermo-optic response. It is shown that the thermal nonlinear optical response of properly designed heterogeneous trimer structures is 40 times larger than that of isolated gold nanoparticles.

Finally, in Chapter 7, we summarize the results presented in this Thesis and discuss future research opportunities.

2. CASCADED PLASMON RESONANT FIELD ENHANCEMENT IN NANOPARTICLE DIMERS IN THE POINT DIPOLE MODEL

2.1. Introduction

In 2003, Li *et al.* demonstrated a specific type of coupled nanoparticle structure in which extremely large field enhancement factors can be produced due to a phenomenon called *cascaded plasmon resonance* [89]. In cascaded plasmon resonance, the enhanced near-field of a larger nanoparticle acts as the driving electric field for a nearby smaller nanoparticle, leading to additional field confinement and enhancement. Cascaded plasmon resonance can enhance broad variety of optical effects, including SERS [101], nonlinear optical response [73], and stimulated emission[102]. Subsequently Sun and Khurgin presented an analytical model that describes the field enhancement in coupled asymmetric particle systems [94, 95], focusing on the external field enhancement that could be achieved in the presence of multipolar interactions.

Here we discuss the coupling regimes in a nanostructure consisting of two silver nanospheres when the relative particle sizes are varied, with the ultimate goal of using cascaded field enhancement for improving the nonlinear refractive index of composites containing such structures. Studying inter-particle interactions in a coupled dimer system can lead to a better understanding of the fundamental interaction mechanisms in cascaded plasmon resonance, and provide a prediction of the maximum field enhancement factors that can be achieved in the cascaded dimer structure. We evaluate the coupling strength and resultant cascaded field enhancement as a function of the particle size difference and inter-particle spacing using a point-dipole description of asymmetric silver dimers. We will describe different coupling regimes based

of the mutual interaction strength between the two nanoparticles. Figure 2.1 shows a schematic of the type of dimer structure under investigation.
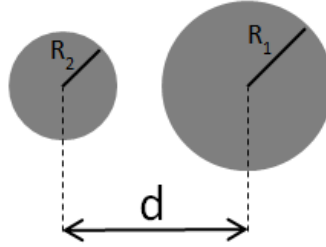
Figure 2.1: A schematic of the type of asymmetric plasmon resonant dimer structure under investigation.

2.2. Dipole-Dipole Interaction Model

In the point dipole model, each nanosphere is considered as a point dipole with a polarizability α_i given by

$$\alpha_i = 3\varepsilon_0\varepsilon_h \, V_i \frac{\varepsilon_m - \varepsilon_h}{\varepsilon_m + 2\varepsilon_h} \tag{2.1}$$

where V_i, is the volume of nanosphere i. ε_0, ε_m and ε_h are the vacuum permittivity, the dielectric function of the metal and the dielectric function of the host, respectively. The dipole moment of an illuminated nanosphere located at position $\mathbf{r}_i$ in the presence of fields from neighboring particles can be written as

16

$$\mathbf{p}_i = \alpha_i \mathbf{E}_{loc}(\mathbf{r}_i) \tag{2.2}$$

where $\mathbf{E}_{loc}(\mathbf{r}_i)$ is the sum of the incident field $\mathbf{E}_{inc}(\mathbf{r}_i)$ and the local electric fields generated by all

the neighbor dipoles at locations $\mathbf{r}_i$, which itself is given by

$$\mathbf{E}_{loc}(\mathbf{r}_i) = \mathbf{E}_{inc}(\mathbf{r}_i) + \mathbf{E}_{dipole,j}(\mathbf{r}_i) = \mathbf{E}_0\, e^{i\mathbf{k}_i.\mathbf{r}_i} - \sum_{i \neq j} \mathbf{A}_{ij}\mathbf{p}_j \tag{2.3}$$

where $\mathbf{A}_{ij}\,\mathbf{p}_j$ is the electric field contribution of dipole j at the position of dipole i and is given by

$$\mathbf{A}_{ij}\mathbf{p}_j = \frac{e^{ikr_{ij}}}{4\pi\varepsilon_0\varepsilon_h r_{ij}^3}\left[k^2 \mathbf{r}_{ij} \times \left(\mathbf{r}_{ij} \times \mathbf{p}_j\right) + \frac{(1-ikr_{ij})}{r_{ij}^2}\left(r_{ij}^2 \mathbf{p}_j - 3\mathbf{r}_{ij}\left(\mathbf{r}_{ij}.\,\mathbf{p}_j\right)\right)\right] \quad \text{for } i \neq j \tag{2.4}$$

where $\mathbf{r}_{ij} = \mathbf{r}_i - \mathbf{r}_j$, $r_{ij} = |\mathbf{r}_{ij}|$ and k is the magnitude of the wavevector in the host medium. For a

dimer system illuminated with light polarized along the dimer axis, A_{12} and A_{21} are equal and given

by

$$A_{12} = A_{21} = \frac{e^{ikd}}{2\pi\varepsilon_0\varepsilon_h}\left(\frac{ik}{d^2} - \frac{1}{d^3}\right) \tag{2.5}$$

where *d* is the center-to-center separation of the two nanospheres in the dimer structure.

Substitution of Equation (2.3) into Equation (2.2) and considering a dimer structure excited with

longitudinal polarization in the quasi-electrostatic regime, leads to

$$p_1 = \alpha_1[E_{inc} - A_{12}p_2] \; and \; p_2 = \alpha_2[E_{inc} - A_{21}p_1]. \tag{2.6}$$

The dipole moment of both nanoparticles can be obtained by solving these two linear

Equations, leading to

$$p_1 = \alpha_1 \frac{1-\alpha_2 A_{12}}{1-\alpha_1\alpha_2 A_{12}^2} E_{inc} \; and \; p_2 = \alpha_2 \frac{1-\alpha_1 A_{12}}{1-\alpha_1\alpha_2 A_{12}^2} E_{inc}. \tag{2.7}$$

The second term in the denominator, $\alpha_1 \, \alpha_2 \, A_{12}^2$, represents a coupling parameter that describes the effective mutual interaction strength between the dipoles. With the known dipole moment for each nanoparticle, the electric field in every position can be evaluated. Assuming that the structures remain in the quasi-electrostatic limit, the internal electric field of the nanoparticles can be obtained using the following formula,

$$E_{in} = \frac{3\varepsilon_h}{\varepsilon_m + 2\varepsilon_h} E_{loc}. \tag{2.8}$$

The local electric field in Equation (2.8) can be obtained using the obtained dipole moment in Equation (2.7) together with Equation (2.2) which states $E_{loc} = p/\alpha$. The internal electric field of the small nanoparticle in the dimer structure thus becomes:

$$E_{in,1} = \frac{3\varepsilon_h}{\varepsilon_m + 2\varepsilon_h} E_{loc,1} = \frac{3\varepsilon_h}{\varepsilon_m + 2\varepsilon_h} \frac{1-\alpha_2 A_{12}}{1-\alpha_1\alpha_2 A_{12}^2} E_{inc}. \tag{2.9}$$

The internal field enhancement factor is defined as $g_{in} = E_{in}/E_{inc}$, which for particle 1 becomes:

$$g_{in,1} = \frac{3\varepsilon_h}{\varepsilon_m + 2\varepsilon_h} \frac{1-\alpha_2 A_{12}}{1-\alpha_1\alpha_2 A_{12}^2}. \tag{2.10}$$

Using the continuity of the normal electric displacement at the metal surface, $\varepsilon_h E_{out} = \varepsilon_m E_{in}$, and Equation (2.10), the external field enhancement factor at the surface of the small nanoparticle in the dimer structure can be written as

$$g_{out,1} = \frac{\varepsilon_m}{\varepsilon_h} \, g_{in,1}. \tag{2.11}$$

We introduce a parameter called the multiplicative field enhancement factor g_{MFE} which is the product of the external field enhancement factor of an isolated large nanoparticle measured at the position of the small nanoparticle (i.e. at a distance d from the center of the large nanoparticle) and the internal field enhancement of the isolated small nanoparticle, *i.e.*

$$g_{MFE,1} = g_{out,2}(d) \, g_{in,1} \tag{2.12}$$

where $g_{out,2}$ (*d*) represents the field contribution of the large nanoparticle at a distance *d* from the center of that nanoparticle.

2.3. Results

Figure 2.2 shows the internal field enhancement spectra, $|g_{in}| = |E_{in}/E_0|$, in each particle for four silver nanoparticle dimers with different volume ratios, V_2/V_1, at a fixed center-to-center separation d = 15 nm. The radius of the small nanoparticle is varied while that of the large nanoparticle is kept constant at 5 nm. The particles are embedded in a host with ε_h = 2.25, and literature data were used for the dielectric function of silver [103].
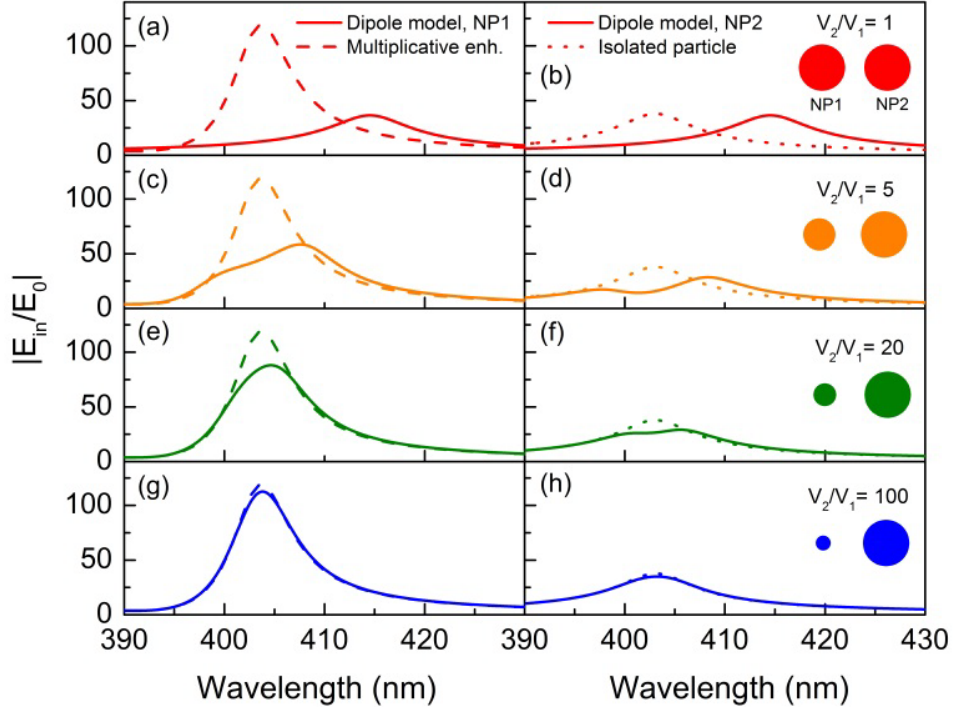
Figure 2.2: Internal field enhancement spectra for silver nanoparticle dimers at a constant center-to-center distance of 15 nm, for the small particle (left panels) and the large particle (right panels) for volume ratios $V_2/V_1 = 1, 5, 20, 100$ as indicated in the insets. The dashed lines (left panels) show multiplicative cascaded field enhancement while the dotted lines (right panel) show the analytical single particle field enhancement.

Figure 2.2(a) and Figure 2.2(b) show the field enhancement in the center of the left and right particle respectively for a dimer of particles with identical volume. For comparison, Figure 2.2(b) includes the internal field enhancement $|g_{in,iso}|$ of an isolated silver nanosphere (dotted line). The maximum field enhancement values in the dimer are similar to those of the isolated sphere but occur at longer wavelength due to near-field coupling between the particles [104]. The

enhancement factors are much weaker than expected for cascaded field enhancement: in the simplest interpretation of cascading, particle 1 is driven by a modified local field $E_{\text{loc},1}$, leading to a predicted multiplicative field enhancement magnitude of $|g_{\text{in,iso}} \times E_{\text{loc},1}|$. This response is shown in Figure 2.2(a) (dashed line), showing a peak enhancement of 119, compared to an actual peak enhancement of 36.5. Figure 2.2(c) and Figure 2.2(d) show the results for a dimer with a volume ratio of 5. The field enhancement in the large particle shows two resonance peaks, with the low-frequency resonance corresponding to a symmetric mode where the dipole moments in both particles oscillate in-phase (phase data not shown), and the high-frequency resonance corresponding to an anti-symmetric mode where the dipole moments in both particles oscillate in anti-phase[105]. At this larger volume ratio, the peak field enhancement in the small particle has increased, but is still substantially lower than the multiplicative cascading response. Figure 2.2(e) and (f) show the results for a volume ratio of 20, showing less pronounced splitting, indicative of a reduced interaction. Note that the internal field enhancement in the small particle approaches the multiplicative cascading response. Finally, Figure 2.2(g) and Figure 2.2(h) show the results for a volume ratio of 100. No clear frequency splitting is observed, the response of the large nanoparticle is almost identical to that of an isolated nanoparticle, and the internal field enhancement of the small particle is virtually identical to the calculated multiplicative cascading response. These results demonstrate that multiplicative cascading requires weak mutual interaction, corresponding to $\alpha_1 \alpha_2 A_{12}^2 \ll 1$ in Equation (2.7). For strong interaction we observe reduced field enhancement, a coupling regime that we will call *hindered cascading*.

Figure 2.3 shows the field enhancement spectra in silver nanoparticle dimers with $V_2/V_1 = 100$ for different center-to-center separations. Figure 2.3(a) and Figure 2.3(b) show the results for a center-to-center separation of 40 nm for the small and large particle respectively. At this separation, the magnitude of the internal field enhancement of the large nanoparticle is approximately equal to that of an isolated nanoparticle $|g_{in,iso}|$ (Figure 2.3(b), dotted line). The field enhancement of the small particle is a factor ~1.5 larger than observed in the large particle, and its spectrum is nearly identical to the multiplicative cascading result (Figure 2.3(a), dashed line), indicating that the particles are weakly coupled. Figure 2.3(c) and Figure 2.3(d) show the results for a center-to-center separation of 15 nm. The smaller separation leads to an increased field enhancement in the small particle due to the larger near field provided by the large particle at this distance, while the internal field enhancement of the small particle is close to the multiplicative field enhancement result. At a center-to-center separation of 12 nm (Figure 2.3(e) and Figure 2.3(f)) clear splitting is observed in the field enhancement spectra, while the peak value of the field enhancement of the small nanoparticle is approximately 200, significantly below the predicted multiplicative field enhancement. Finally, for a center-to-center separation of 10 nm (Figure 2.3(g) and Figure 2.3(h)), a large mode splitting is observed while the maximum internal field enhancement of the small nanoparticle remains approximately the same, with a value well below the theoretical multiplicative field enhancement due to the strong mutual interaction.
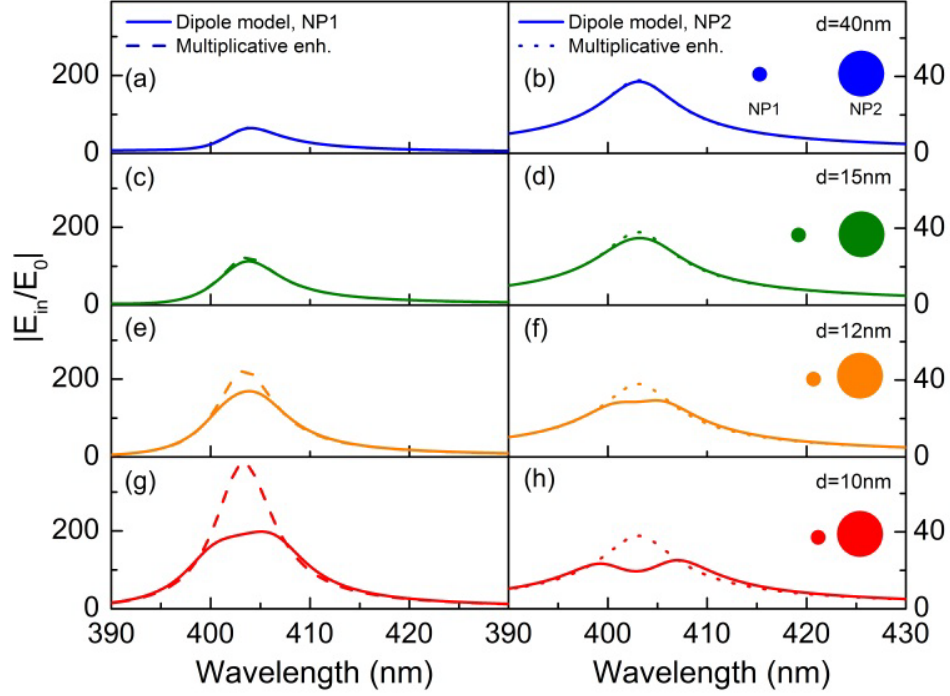
Figure 2.3: Internal field enhancement spectra for silver nanoparticle dimers at a fixed volume ratio of 100 for the small particle (left panels) and the large particle (right panels) for interparticle separations of d = 10 nm, 12 nm, 15 nm, and 40 nm as indicated in the insets. The dashed lines (left panels) show multiplicative cascaded field enhancement while the dotted lines (right panel) show the analytical single particle field enhancement.

The observations in Figure 2.2 and Figure 2.3 indicate the existence of an *ultimate cascading limit*, corresponding to a situation in which the smaller particle is sufficiently close to the large nanoparticle to experience its maximum external field enhancement of $|3\varepsilon_m(\omega_{LSP})/(\varepsilon_m(\omega_{LSP})+2\varepsilon_h)|$. In this case multiplicative cascading would produce an ultimate internal field enhancement of magnitude $|g_{ucl,in}| = |g_{1,in}(\omega_{LSP}) \times 3\varepsilon_m(\omega_{LSP})/(\varepsilon_m(\omega_{LSP}) + 2\varepsilon_h)| = 2$

$(3\varepsilon_h/\text{Im}(\varepsilon_m))^2$. Similarly we can obtain an ultimate external cascaded field enhancement limit near the small particle given by $|g_{ucl,ext}| = 2 |g_{ucl,in}|$, which matches the result obtained by Ref. [95]. In the following we investigate the evolution of the cascaded field enhancement as a function of geometry and compare the obtained values to the theoretical ultimate cascading limit.
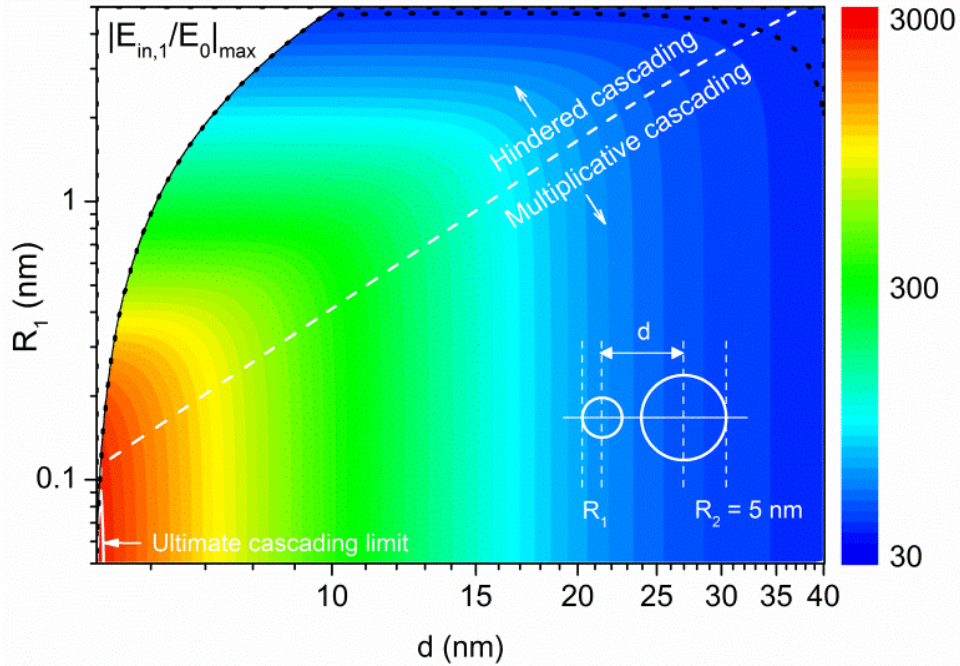
Figure 2.4: Maximum internal field enhancement in silver nanoparticle dimers calculated by a point-dipole interaction model. The dotted black line indicates the field enhancement of an isolated Ag nanosphere. The white dashed line separates the hindered and multiplicative cascading regimes. The white solid line shows field enhancement values that are within 15% of the analytical ultimate cascading limit.

Figure 2.4 shows the maximum internal field enhancement in silver nanoparticle dimer as a function of center-to-center distance and particle radius calculated using the dipole interaction model. The radius of the large nanoparticle is held at 5 nm while the radius of the small particle R_1 is varied. For small size difference (large R_1) or large inter-particle spacing, low field enhancement values are observed. For most geometries the field enhancement exceeds that of an isolated silver nanoparticle (black dotted contour line), with the exception of dimers with small volume ratio or large inter-particle spacing. The former exception is due to a significant redshift in the main resonance frequency (see Figure 2.2(a) and Figure 2.2(b)), which is accompanied by an increase of the imaginary part of the Au dielectric function. The latter exception is due to the oscillatory nature of the dipole interaction term in Equation (2.5), in particular the term e^{ikd}, allowing for both constructive and destructive interaction between the particles in the dimer depending on the inter-particle spacing. The largest field enhancement values are observed at small spacing and large size difference. To indicate the transition from hindered cascading to multiplicative cascading, the white dashed line shows geometries that produce a field enhancement that is 95% of the multiplicative cascaded field enhancement. Note that multiplicative cascaded field enhancement requires weak coupling, which can be achieved either for large separation, or for small separation and large size difference. Only for extremely large volume ratios and small separation, field enhancements are observed that approach the calculated ultimate cascading limit of $|g_{ucl}| = 2.9 \times 10^3$ for these materials. The corresponding maximum external field enhancement is 5.8×10^3, which is a factor ~19 larger than that calculated for the asymmetric gold dimers studied in Ref. [95] due to the higher surface plasmon damping in gold and the inclusion of radiative damping in Ref. [95].

The white solid contour shows the geometries in which the field enhancement is 85% of the ultimate cascading limit. It should be pointed out that the point dipole analysis presented here neglects surface scattering, which is known to introduce significant damping at the sizes considered here, and consequently reduced field enhancement factors can be expected in experiments on similarly sized particles.

The results shown in Figure 2.4 have several implications. First, for most geometries shown, asymmetric nanoparticle dimers produce field enhancement factors that significantly exceed those of isolated particles, even in the case of hindered cascading. Second, approaching the ultimate cascading limit to within 15% requires extremely large volume ratios, providing a significant challenge for experiments aimed at demonstrating this limit. Third, reaching the ultimate cascading limit requires extremely small edge-to-edge spacing. Finally, it should be pointed out that the dipole interaction model does not include multipolar plasmon modes, which are expected to occur for small inter-particle spacing at intermediate volume ratios. However, for coupling conditions that lead to large near-multiplicative enhancement factors, the mutual interaction is necessarily weak. Since multipolar modes on these particles are predominantly excited due to the inhomogeneous near-field from neighboring particles, weak interaction implies the relatively weak excitation of multipolar modes. Consequently, our simplified model provides surprisingly accurate results especially for systems that produce large field enhancement. To illustrate this point, Figure 2.5(a) includes internal field enhancement spectra $|g_{in,1}|$ calculated using the dipole interaction method for a dimer with volume ratio 1000, R_1=0.5 nm, R_2=5 nm and d=9 nm, and using full numerical simulation[87]. The results show remarkable agreement, and demonstrate the usefulness of the dipole model even for finite sizes structures in the presence of

26

significant cascading under weak mutual interaction. Figure 2.5(b) shows the corresponding spatial distribution of the electric field enhancement at the plasmon resonance wavelength, demonstrating the extremely localized nature of the field enhancement.
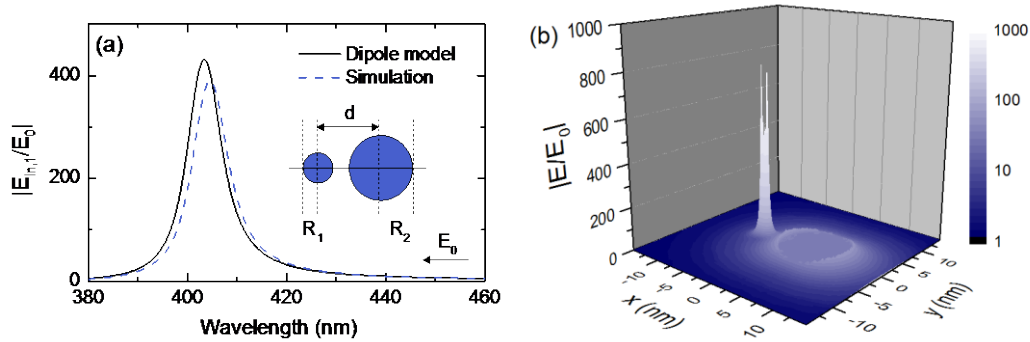
Figure 2.5: (a) Field enhancement spectra in the smaller of two particles in a silver dimer with particle radii of 0.5 nm and 5 nm at a center-to-center spacing of 9 nm calculated using a dipole-dipole interaction model (solid line) and using full electromagnetic simulation (dashed line). (b) Simulated electric field enhancement distribution around the same structure at a wavelength of 404 nm.

2.4. Summary

A dipole-dipole interaction model was used to evaluate cascaded field enhancement in asymmetric silver nanosphere dimers. Field enhancement spectra were evaluated as a function of the particle size difference and inter-particle spacing. We observe three distinct regimes of cascaded field enhancement: hindered cascading, multiplicative cascading, and the ultimate cascading limit, depending on the dimer interaction strength. In the limit of weak-mutual coupling,

27

analytical formulas were derived for the ultimate internal and external field enhancement factors in coupled nanosphere dimers. For silver dimers in a host with index 1.5 we obtain a maximum internal field enhancement of 2.9×10^3, a factor of 75 larger than that of an isolated silver nanoparticle.

3. CASCADED FIELD ENHANCEMENT IN PLASMON RESONANT DIMER NANOANTENNAS COMPATIBLE WITH TWO-DIMENSIONAL NANOFABRICATION METHODS

3.1. Introduction

As discussed in Chapter 2, a special class of coupled plasmon resonances called cascaded plasmon resonances can produce unusually strong field enhancement [89, 94]. In cascaded plasmon resonance, near-field coupling of nanoparticles that have the same plasmon resonance frequency but significantly different volume can lead to additional field enhancement due to the fact that the smaller of the particles is excited predominantly by the enhanced near-fields of the larger particle. The simplest system that produces this effect is shown in Figure 3.1(a), consisting of an asymmetric nanosphere dimer, as discussed in Chapter 2. However, it is difficult to fabricate such cascaded nanosphere structures with standard top-down nanofabrication tools such as electron beam lithography or nano-imprint lithography since these methods typically produce structures that have a fixed thickness, determined for example by a thin film deposition step in the process. Under these conditions, changing the volume of nanoparticles requires a modification of the lateral size of and therefore the aspect ratio of the particles, which is known to cause significant resonance shifts [86, 106]. This implies that one of the main requirements for cascaded plasmon resonance cannot be satisfied in top-down nanofabricated structures, posing a significant challenge to the development of technologies that utilize cascaded plasmon resonances. In the present work we demonstrate that cascaded plasmon resonance can be achieved in shape-tuned dimer antennas

with identical maximum thickness (Figure 3.1(b)-(d)) by modifying the in-plane particle aspect ratio to correct for size induced resonance shifts.

(a) $V_r = 1000$ (b) $V_r = 10$

(c) $V_r = 100$ (d) $V_r = 1000$
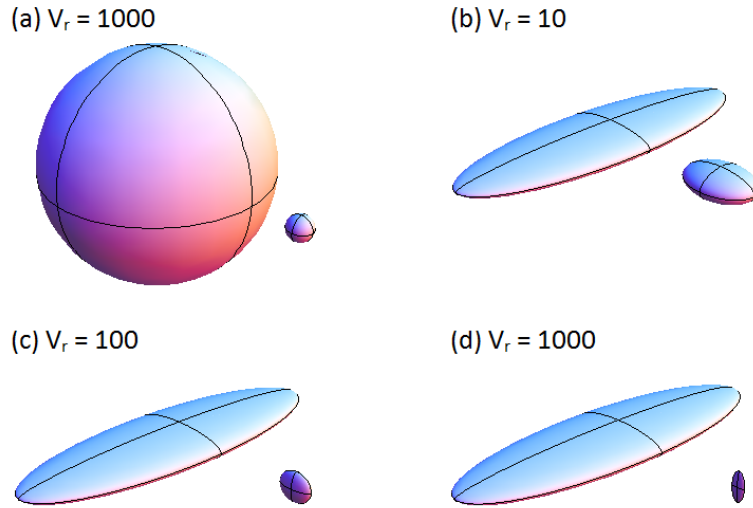
Figure 3.1: (a) Cascaded nanosphere dimer with volume ratio of $V_r = 1000$, and shape-tuned cascaded nanoparticle dimers with volume ratios of (b) 10, (c) 100 and (d) 1000.

In this chapter, we demonstrate cascaded field enhancement in asymmetric plasmon resonant dimer nanoantennas consisting of shape-tuned ellipsoidal nanoparticles. The nanoparticles that make up the dimer have identical thickness, suggesting that the presented approach can be used to design cascaded dimer antennas compatible with standard two-dimensional top-down nanofabrication tools such as electron beam lithography and nano-imprint lithography. Cascaded excitation is achieved by modification of the in-plane particle aspect ratios in a way that keeps the resonance frequency of the individual particles fixed, while significantly

changing their polarizability. The achievable field enhancement is evaluated as a function of the particle volume ratio and spacing.

3.2. Theory

In order to study the feasibility of designing cascaded plasmon resonances using nanoparticles with identical thickness, we consider dimer antennas composed of ellipsoidal particles. Ellipsoidal metal nanoparticles support dipolar localized plasmon resonances with a localized plasmon resonance frequency that is affected by the particle aspect ratio. The plasmon resonance frequency of ellipsoids can be obtained from the expression for the polarizability. In the quasi-electrostatic approximation, the polarizability of an ellipsoid with axes a, b and c, illuminated by a plane wave polarized along the a direction, is given by[106]:

$$\alpha_a = V \frac{\varepsilon_m - \varepsilon_h}{\varepsilon_h + L\,(\varepsilon_m - \varepsilon_h)} \tag{3.1}$$

where ε_m and ε_h are the dielectric function of the metal and the host material respectively, and V is the volume of the ellipsoidal particle given by ($abc\pi/6$). Equation (3.1) assumes that the particle dipole moment relates to the incident field according to $p = \varepsilon_0\,\varepsilon_h\,\alpha\,E$ with ε_0 the permittivity of vacuum. L is a shape-dependent factor ranging from 0 to 1, which can be calculated using the below integral

$$L = \frac{abc}{2} \int_0^\infty (a^2 + q)^{-\frac{3}{2}} (b^2 + q)^{-\frac{1}{2}} (c^2 + q)^{-\frac{1}{2}} dq \tag{3.2}$$

where a, b and c are the semi-axes of the ellipsoid with a being the axis along the incident light polarization, and q is a variable of integration. Shape factors for excitation with the incident field

31

along the *b* and *c* directions can be obtained by exchanging the position of *a* with that of *b* or *c* in Equation (3.2), respectively. In addition, the electric field inside the ellipsoid, in the quasi-electrostatic approximation, is given by [106]:

$$E_{in} = \frac{\varepsilon_h}{\varepsilon_h + L_a(\varepsilon_m - \varepsilon_h)} E_0 \qquad (3.3)$$

where E_0 is the amplitude of the electric field of the incident light. The corresponding maximum external field enhancement is given by $E_{out} = (\varepsilon_m/\varepsilon_h) E_{in}$. The dipolar plasmon resonance occurs when the real part of the denominator of the polarizability, Equation (3.1), becomes a minimum, corresponding to the resonance condition $\varepsilon_m' = - R \varepsilon_h$, where ε_m' is the real part of the dielectric function of the metal and $R = (1/L_a - 1)$. For a sphere $L_a = 1/3$ leading to the well-known resonance requirement $\varepsilon_m' = -2\varepsilon_h$. The imaginary part of the host dielectric function is assumed to be negligible.

3.3. Results

Figure 3.2 shows a contour plot of calculated resonance conditions for a large range of particle shapes. The axis lengths are scaled with respect to the axis that is aligned with the polarization of the incident light. For readability of the graph, the logarithms of the axis ratios and the resonance condition are displayed. Since the resonance condition is not affected by an interchange of axes *b* and *c* in the quasi-electrostatic limit, all unique shapes and resonance conditions with axis ratios between 0.1 and 10 are represented by the data in the upper left side of the graph. Six example shapes and their corresponding aspect ratios have been included and labeled with roman numerals.

32
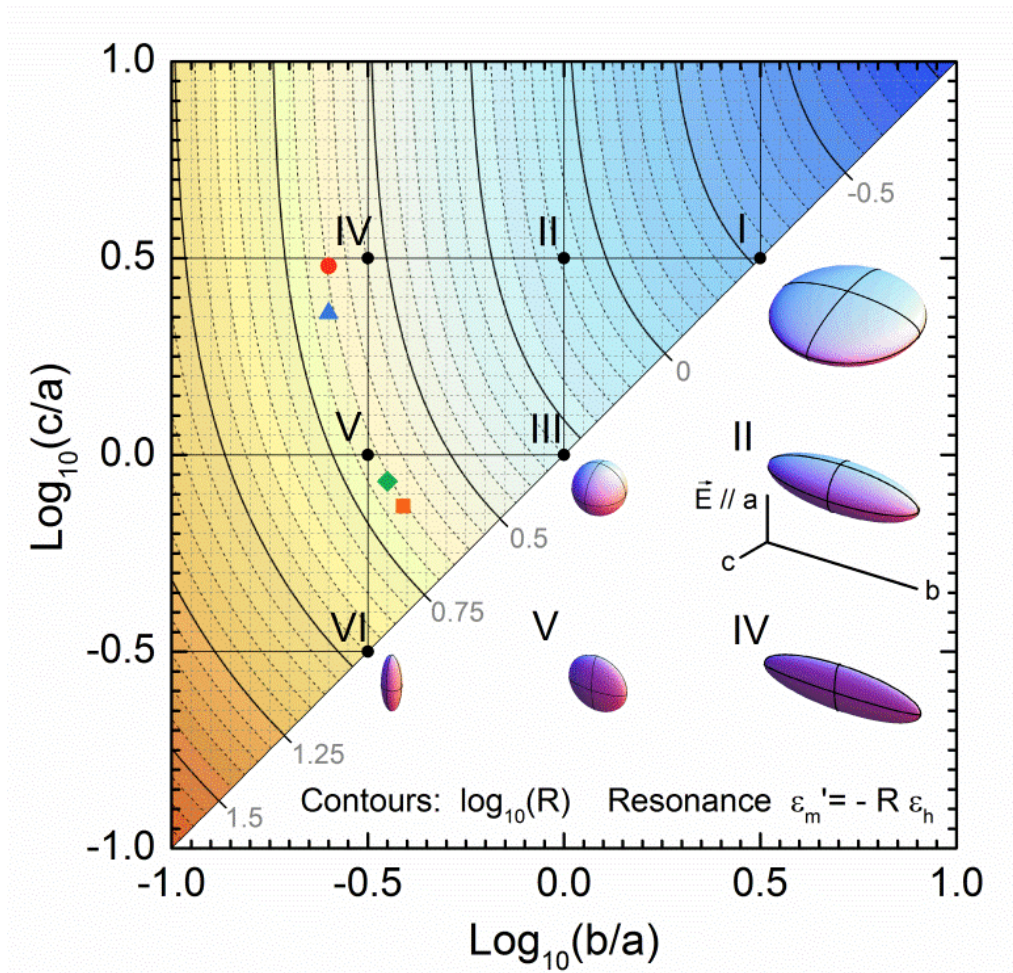
Figure 3.2: Shape dependent dipolar resonance conditions for ellipsoidal nanoparticles with axis lengths a, b, and c, illuminated by an electromagnetic wave polarized along the a-axis. Contour lines represent the logarithm of the resonance prefactor R. The insets show ellipsoids with the axis ratios indicated by the roman numerals. The symbols indicate the aspect ratios used in the cascaded dimer antennas shown in Figure 3.1.

Figure 3.2 demonstrates that it is possible to design nanoparticles with different shape but identical resonance frequency: by choosing shapes that lie on one of the contour lines and scaling

axis *b* or *c* to the desired thickness, we obtain shapes with different volume but the same resonance frequency, which is one of the key requirements for achieving cascaded plasmon resonance.

In this study we consider dimer nanoantennas consisting of silver nanoellipsoids embedded in a host material with $\varepsilon_h = 2.25$. The thickness of all ellipsoids was held constant at 5 nm. The largest particle considered in this study has axis lengths (*a*, *b*, *c*) given by (20 nm, 5 nm, 60 nm). The corresponding aspect ratio is indicated by the red circle in Figure 3.2. From the contour line or through numerical evaluation of Equation (3.1), it can be shown that this shape is expected to exhibit a dipolar resonance when $\varepsilon_m' = - 4.42\ \varepsilon_h$. However the finite size of the ellipsoid is expected to cause small resonance shifts when taking into account retardation effects. To determine the actual resonance wavelength of this ellipsoid, frequency domain electromagnetic simulations[87] were carried out. The ellipsoidal Ag particle was illuminated with a plane wave with electric field amplitude E_0, propagating in the direction corresponding to the thickness of the particle ('normal incidence'), and polarized along the *a* axis of the particle. Figure 3.3 shows the resulting frequency dependent electric field amplitude at the center of the ellipsoid, relative to the incident wave amplitude. The corresponding particle shape is shown as an inset. A clear plasmon resonance is observed at $\lambda=508$ nm, corresponding to a resonance condition $\varepsilon_m' = - 4.5\ \varepsilon_h$, close to the analytically predicted result. Three additional particle shapes were selected with a volume that is respectively a factor 10, 100, and 1000 smaller than that of the largest particle. The corresponding shapes are (12.8 nm, 5 nm, 9.4 nm), (5.8 nm, 2.1 nm, 5 nm), and (2.2 nm, 0.56 nm, 5 nm) as marked in Figure 3.2 respectively by a solid square, diamond, and triangle. Note that these shapes all lie close to the contour line R=0.65, corresponding to a resonance condition $\varepsilon_m' = -4.5\ \varepsilon_h$. The

corresponding simulated internal field enhancement spectra are included in Figure 3.3, all showing

a resonance wavelength of 508 ± 1 nm. The largest simulated internal field enhancement is 35,

corresponding to the analytically predicted result within 1.5 %.
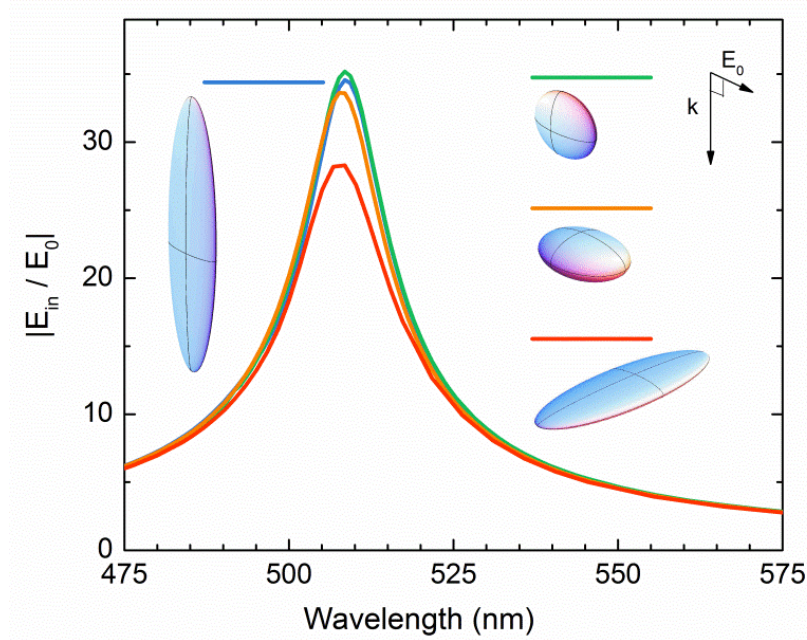
Figure 3.3: Internal field enhancement spectra of isolated silver nanoparticles in a host with

dielectric function $\varepsilon_h = 2.25$ with axes (a,b,c) given by (2.2 nm, 0.58 nm, 5 nm), (5.8 nm, 2.1 nm,

5 nm), (12.8 nm, 5 nm, 9.4 nm) and (20 nm, 5 nm, 60 nm). The legend shows the corresponding

shapes (not to scale).

To investigate the development of cascaded plasmon resonances in shape-tuned dimer

antennas, dimers with three different volume ratios were considered based on the four ellipsoids

shown in Figure 3.3. The corresponding antenna structures are shown in Figure 3.1(b)-(d) for a

center-to-center spacing of d=25 nm. Figure 3.4(a) shows the simulated internal field enhancement

at the center of the small nanoparticle for the three different dimer nanoantennas with d=40 nm. The corresponding volume ratios are 10 (orange line), 100 (green line) and 1000 (blue line). The internal field enhancement of the largest isolated nanoparticle (red line) is included for comparison, corresponding to the red curve in Figure 3.4. The maximum internal field enhancement factors for the coupled dimer antennas occurs at a wavelength that is slightly red-shifted compared to dipole resonance of the isolated particles, indicative of relatively weak inter-particle interaction. The field enhancement factors are slightly larger than observed for the isolated particles in Figure 3.3. Figure 3.4(b) shows the results for the same particle combinations for a smaller center-to-center spacing of d=25 nm. Several notable differences are observed. First, the dimer with a relatively small volume ratio of 10 shows a significant red-shift, indicative of increased mutual interaction. This effect is not observed for the two dimers with larger volume ratios, which is attributed to the lower polarizability of the smaller particles used. Second, the obtained field enhancement factors are significantly larger than in Figure 3.4(a), indicating the appearance of significant cascading. For the largest two volume ratios (smallest particles), the peak enhancement factors are similar despite the very different particle sizes. This is an expected result in the case of weak mutual interaction, and corresponds to a coupling regime called 'multiplicative cascading' in Ref [107] and Chapter 2. Figure 3.4(c) shows the corresponding results for a spacing of d=17 nm. The spectrum for a volume ratio of 10 could not be included as the small center-to-center spacing would lead to overlapping particles. The peak field enhancement of the dimer with volume ratio 100 exhibits a significant redshift compared to the isolated particle response, indicative of stronger inter-particle interaction at this smaller spacing. The dimer with a volume ratio of 1000 shows only a small peak

36

shift of ~2 nm and a strongly improved field enhancement with a peak value of 270, a factor 9.5 larger than that for the larger nanoparticle.
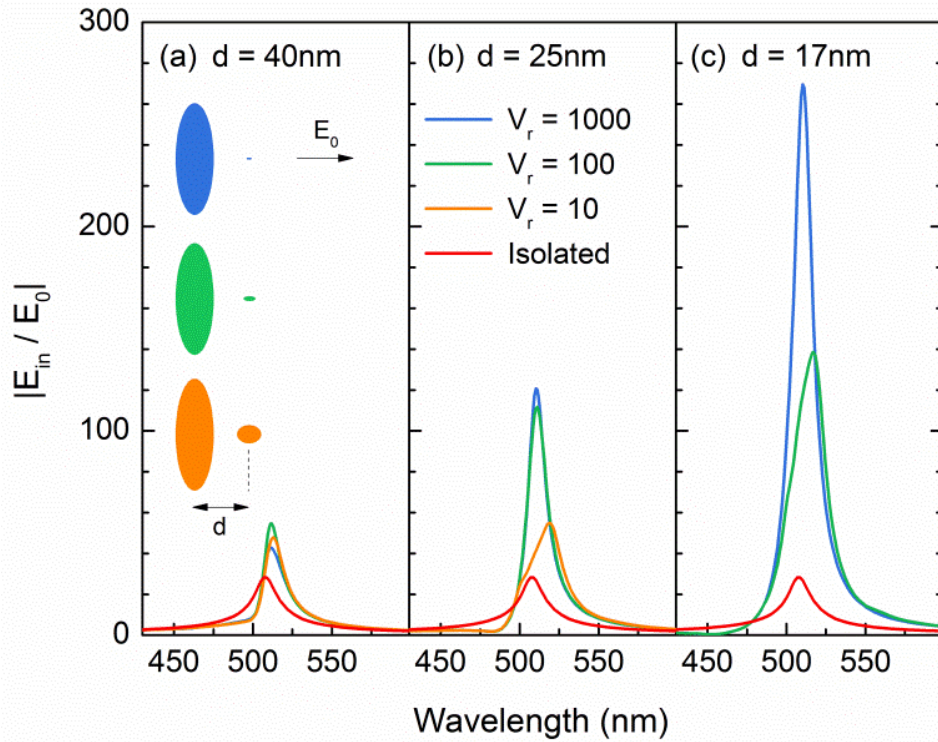
Figure 3.4: Internal field enhancement spectra for the smaller nanoparticle in asymmetric silver dimer nanoantennas at a center-to-center spacing of (a) 40 nm, (b) 25 nm and (c) 17 nm shown for volume ratios V_r of 10, 100 and 1000. The internal field enhancement spectrum of the isolated large nanoparticle with fixed dimensions (20 nm, 5 nm, 60 nm) is included for comparison.

The field enhancement factors observed in Figure 3.4 do not represent the maximum achievable values. Based on an analysis similar to that given in section (2.2) of this thesis or Ref

[107], it can be shown that the maximum field enhancement, i.e. the 'ultimate cascading limit', for internal field enhancement of coupled ellipsoidal dimers in the quasi-electrostatic limit occurs at the localized plasmon resonance frequency ω_{LSP} and is given by

$$\left| g_{in,UCL} \right| = \left| \frac{E_{in}}{E_0} \right| = \frac{Q_{LSP}\sqrt{1+Q_{LSP}^2}}{(1-L_a)L_a} \tag{3.4}$$

where $Q_{LSP} = Re[\varepsilon_m(\omega_{LSP})] / Im[\varepsilon_m(\omega_{LSP})]$. The ultimate external field enhancement follows from $|g_{out,UCL}| \sim |1-1/L_a| \times |g_{in,UCL}|$.

Equation (3.4) predicts a maximum internal field enhancement factor of 5.7×10^3, significantly larger than the results shown in Figure 3.4(c), and a maximum external field enhancement factor of 2.6×10^4. While mathematically and in numerical simulation this result can be achieved, it would require a reduction of the smallest nanoparticle width to below the atomic radius, making such structures experimentally unfeasible. Nevertheless, the results in Figure 3.4, unambiguously demonstrate that a significant degree of cascaded field enhancement can be achieved in shape tuned dimer antennas with fixed thickness and large volume ratios. Such structures could be fabricated e.g. using electron beam lithography, within the resolution limits of the technique. Experimental demonstrations of these effects will need to take into account retardation effects including multipolar excitations, surface scattering for small particle sizes, the asymmetric environment due to the presence of a substrate, and deviations from the ideal ellipsoidal shapes that were considered in the present study. For example, the presence of a high-index substrate is expected to introduce spectral shifts due to a change in the local dielectric environment, and could enable the excitation of multipolar modes not present in the current study

38

due to a modification of the symmetry of the local environment. Depending on the importance of these experimental factors on the ultimate field enhancement factors, the presented dimer antenna design could become a basic building block in top-down nanofabricated cascaded plasmon resonant devices.

3.4. Summary

It was demonstrated through numerical simulation that cascaded plasmon resonances can be achieved in dimer nanoantennas consisting of near-field coupled ellipsoidal particles with identical thickness. The identical thickness for nanoparticles leads to cascaded antenna designs that are compatible with common top-down nanofabrication methods such as electron beam lithography and nano-imprint lithography. A shape optimization method was presented that may be used to design asymmetric dimers consisting of nanoparticles with an identical plasmon resonance frequency. The field enhancement was evaluated as a function of the particle volume ratio and spacing, and shows the strongest cascaded field enhancement for the largest volume ratio. The largest field enhancement factors that can be achieved in the ultimate cascading limit are 5.7×10^3 for the internal field enhancement factor and 2.6×10^4 for the external field enhancement factor.

4. CASCADED PLASMONIC METAMATERIALS FOR PHASE-CONTROLLED ENHANCEMENT OF NONLINEAR ABSORPTION AND REFRACTION

4.1. Introduction

The electric field enhancement in metal-dielectric nanocomposites is expected to lead to a dramatic change in the nonlinear optical response of the composite. It has been demonstrated that harmonic generation, in particular second and third harmonic generation can be enhanced in such nonlinear metamaterials (NLM). In addition, nonlinear optical refraction and absorption is strongly modified in these nanocomposites due to the fact that the enhancement of Kerr-type third-order nonlinearities scales with the fourth power of the electric field enhancement[52]. While large enhancements in nonlinear susceptibility are readily obtained, achieving improved device performance is non-trivial due to the fact that the introduction of plasmon resonant elements necessarily contributes to the linear absorption. For this reason, application specific figures of merit are defined that can take into account any absorption present in the system. This becomes especially important in applications that operate in transmission mode, as is the case in absorptive optical switching [108-110]. The third-order nonlinear response and corresponding figure of merit of several metal dielectric nanocomposites have been investigated as a function of a variety of structural parameters [67, 111-118].

An area of particular current interest involves the nonlinear optical response of systems that exhibit coupled plasmon resonances. The interaction of coupled localized surface plasmons in dimers and particle chains as well as their relevant spectral properties and field enhancement

factors have been studied extensively[119-129]. As discussed in the preceding chapters, a special type of coupled plasmon resonances known as cascaded plasmon resonances, have received significant attention due to their ability to provide unusually large field enhancement factors. The use of cascaded resonances could potentially lead to NLMs that exhibit a stronger nonlinear optical response than can be obtained using isolated plasmonic resonators. However, it is not yet known whether the stronger localized field and the modified frequency response can produce an improved figure of merit for nonlinear absorption or refraction.

In this chapter, we investigate the nonlinear absorptive and refractive response of metamaterials composed of near-field coupled spherical silver nanoparticles with a binary size distribution. An example of the resulting cascaded plasmon resonant nonlinear metamaterial is shown in Figure 4.1.
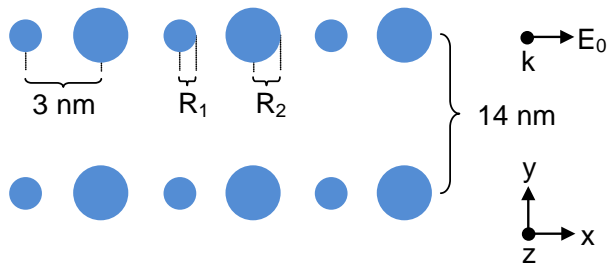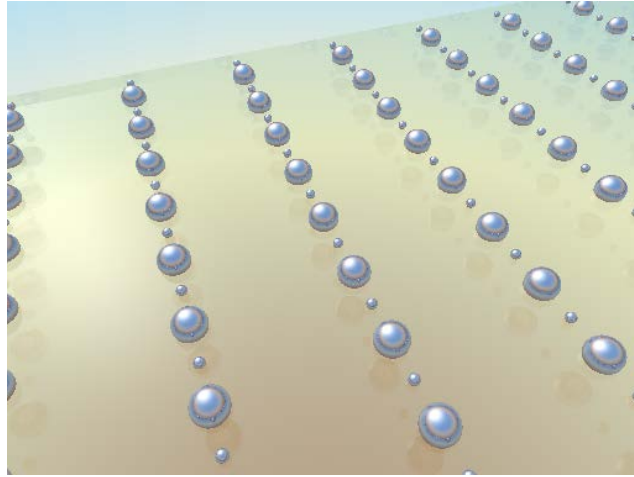
Figure 4.1: Three-dimensional rendering of a cascaded plasmon resonant nonlinear metamaterial, containing regularly spaced silver particles with a binary particle size distribution (top panel), and a cross-section of one of the simulated cascaded plasmon resonant nonlinear metamaterials indicating the relevant size and spacing parameters (lower panel). The structure is excited using an x-polarized plane wave propagating in the z-direction.

4.2. Theory

We consider two-dimensional arrays of silver nanoparticles of alternating sizes, resulting in a set of nanoparticle chains with relatively small inter-particle spacing within each chain and a relatively large spacing between chains, as indicated schematically in Figure 4.1. In order to remain well within the quasi-electrostatic limit, small particle sizes (diameter less than 2.5 nm) have been assumed. However as discussed in more detail below, the approach is not limited to such small sizes, and can be scaled up by at least an order of magnitude with similar results. The center-to-center spacing between adjacent particles is held constant at 3 nm, while the inter-chain spacing is set to 14 nm. The nanoparticles are assumed to be embedded in a host with refractive index of 1.5, representative of e.g. glass or common polymeric optical materials. The linear optical properties of the silver particles are modeled by a Drude fit to literature data given by $\varepsilon_{Ag} = \varepsilon_\infty - \omega_p^2/(\omega^2 + i\omega\Gamma)$ where $\varepsilon_\infty = 5.451$, $\omega_p = 1.474 \times 10^{16}$ rad/s, and $\Gamma = 8.354 \times 10^{13}$ s^{-1}. Similar to the assumptions made in the original publication on cascading by Li and *et al.*[89, 130], this dielectric function does not include the effect of surface scattering that occurs at small particle diameters. The implications of this choice are discussed in greater detail in the results section. Five geometries with different size dissimilarity between adjacent particles are considered, with particle radii [R_1(nm), R_2(nm)] of [1, 1], [0.85, 1.12], [0.7, 1.18], [0.55, 1.22], and [0.4, 1.25], corresponding to particle volume ratios $(R_2/R_1)^3$ of 1, 2.3, 4.8, 11 and 30. At the chosen sample thickness of 10 nm these choices lead a fixed metal fill fraction of 1%, facilitating direct comparison of the results.

Three-dimensional full vectorial electric field distributions were simulated using frequency domain finite integration technique simulations [87]. The nanocomposite is

illuminated at normal incidence (along the z-axis) using plane wave excitation, polarized along the nanoparticle chain direction (x-axis). The obtained frequency dependent electric field distributions are subsequently evaluated numerically to yield effective medium properties[67].

4.3. Results

Figure 4.2 shows the calculated linear absorption spectra of the five different nanocomposites, obtained through the numerical integration of simulated frequency dependent field distributions using the method described in Ref. [67]. For nanoparticle arrays with a single particle size (red line), two absorption maxima are observed. The main resonance at 432 nm is due to the resonant excitation of a predominantly dipolar plasmon resonance in the individual nanoparticles. This resonance occurs red-shifted relative to the predicted resonance wavelength of 404 nm for similarly sized isolated silver nanoparticles in the same host material as a result of near-field coupling between adjacent nanoparticles[104]. The second relatively weak absorption feature at a wavelength of 375 nm is due to the excitation of a multipolar plasmon resonance on the nanoparticles, as indicated schematically in the inset in Figure 4.2. While this mode is not excited significantly in isolated nanoparticles of this size, the inhomogeneous near-field contributions originating from neighboring particles facilitate the excitation of higher order modes. The introduction of a finite size difference between adjacent particles is seen to lead to two main changes in the absorption spectrum. First, the main absorption peak is seen to gradually blue-shift due to modified inter-particle coupling. This effect can be understood by considering the limiting case in which the volume of the smaller particle is reduced to zero at fixed metal fill fraction,

resulting in an array of slightly larger nanoparticles at an increased inter-particle spacing. This leads to a weaker nearest-neighbor coupling, and a corresponding reduced red-shift. Additionally, the introduction of size differences along the array modifies the array periodicity, leading to the appearance of an additional absorption resonance peak around 395 nm. This additional resonance is seen to increase in strength as the size difference grows, while its position gradually red-shifts.
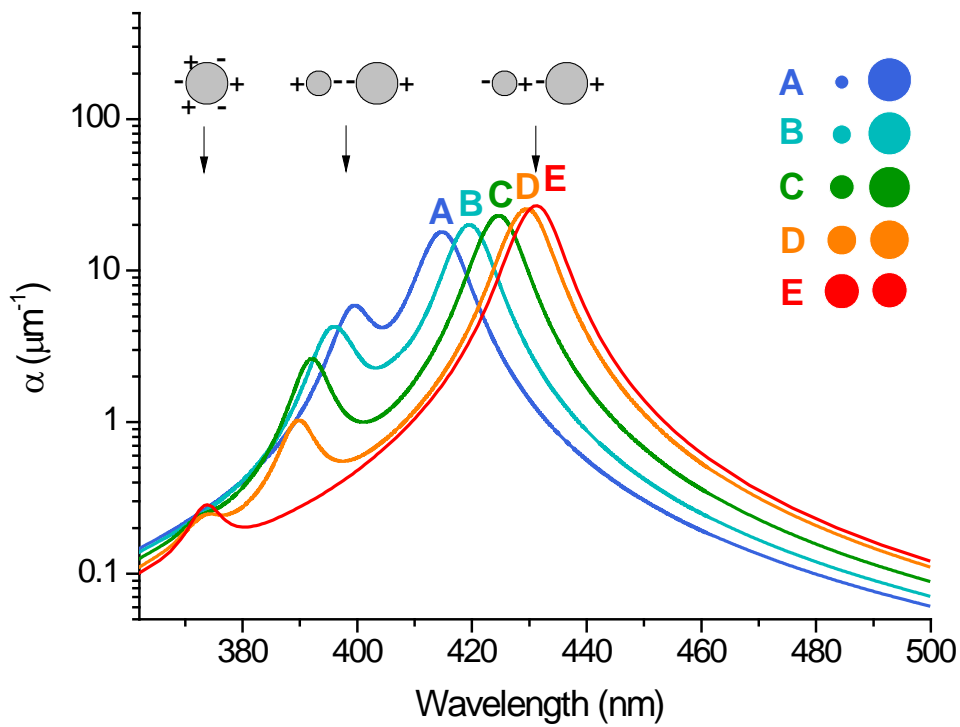
Figure 4.2: Absorption coefficient for five cascaded plasmon resonant metamaterials with nearest-neighbor volume ratios of 1, 2.3, 4.8, 11 and 30. A snapshot of the surface charge distribution corresponding to the three main resonance features is indicated schematically. The legend shows the corresponding unit cell of the periodic metamaterial.

To detect the presence of possible cascaded plasmon resonances, we monitor the frequency dependent electric field enhancement factor (E_x/E_0) at key points in the structure for three of the simulated geometries. Figure 4.3 (a-c) show the magnitude of the electric field enhancement factor at the center of the small nanoparticle (solid line) and of the large nanoparticle (dashed line) for arrays containing particles with a single particle size, Figure 4.3 (a), as well as arrays containing dissimilar particles with a volume ratio of 4.8, Figure 4.3 (b) and 30, Figure 4.3 (c). For the structure with a single particle size, the maximum field enhancement is identical in all particles, and is found to be a factor 33. Introducing a nearest-neighbor size difference is seen to lead to additional field enhancement in the smaller particle across a broad wavelength range. For the structure with the largest volume ratio, Figure 4.3 (c) a maximum field enhancement of $97\times$ is observed, approximately three times that observed in the structure with identically sized particles. This increased enhancement is indicative of a cascaded plasmon resonance, in which the smaller nanoparticle is excited predominantly by the enhanced near-field around the larger nanoparticle, leading to a multiplicative field enhancement.

Figure 4.3 (d-f) show the distribution of magnitude of the electric field enhancement E_x/E_0 at the excitation wavelengths marked λ_S respectively in Figure 4.3 (a-c), shown at a fixed phase in the x-y plane through the centers of the particles in the array. For identically sized particles, Figure 4.3 (d), a moderate field enhancement is observed both inside and outside the particles. Note that at this frequency the field inside adjacent particles has the same sign. This field distribution will be referred to as the 'symmetric mode'. As the size difference increases, Figure 4.3 (e-f), the field enhancement inside and around the smaller nanoparticles is seen to increase, while the field

enhancement in the larger particle is found to be relatively unaffected. These symmetric modes are responsible for the main absorption peak observed in Figure 4.2. Interestingly the peak absorption coefficient for the symmetric mode (see Figure 4.2) is only weakly dependent on the volume ratio, likely due to the fact that the increased internal field in the smaller particle is accompanied by a reduced volume over which the enhanced field is present.

Figure 4.3(g-i) show the spatial distribution of the field enhancement factor for these same structures, for excitation at the wavelengths marked λ_A in Figure 4.3 (a-c). For identically sized particles, Figure 4.3 (g), this wavelength is far from the plasmon resonance wavelength, and consequently only a small internal field enhancement is observed. As the size difference increases, Figure 4.3 (h,i), the field enhancement in and around the smaller nanoparticles is seen to increase. In contrast to the results in Figure 4.3 (e-f), the field inside adjacent particles is opposite in sign. This mode will be referred to as the 'antisymmetric mode'. Note that for evenly spaced arrays with a single particle size this mode cannot be excited by far-field illumination, in which case it represents a dark mode of the system. The introduction of alternating particle sizes introduces a periodicity in the array that matches that of the antisymmetric mode, allowing its far-field excitation of this mode. The appearance of this previously dark mode resembles effects observed in plasmonic electromagnetically induced transparency (EIT), which is due to the interaction of bright and dark modes in coupled metal resonators[131-133]. Similar coupling effects that render dark modes weakly visible lead to the observation of Fano resonances in coupled plasmonic structures[134-138].
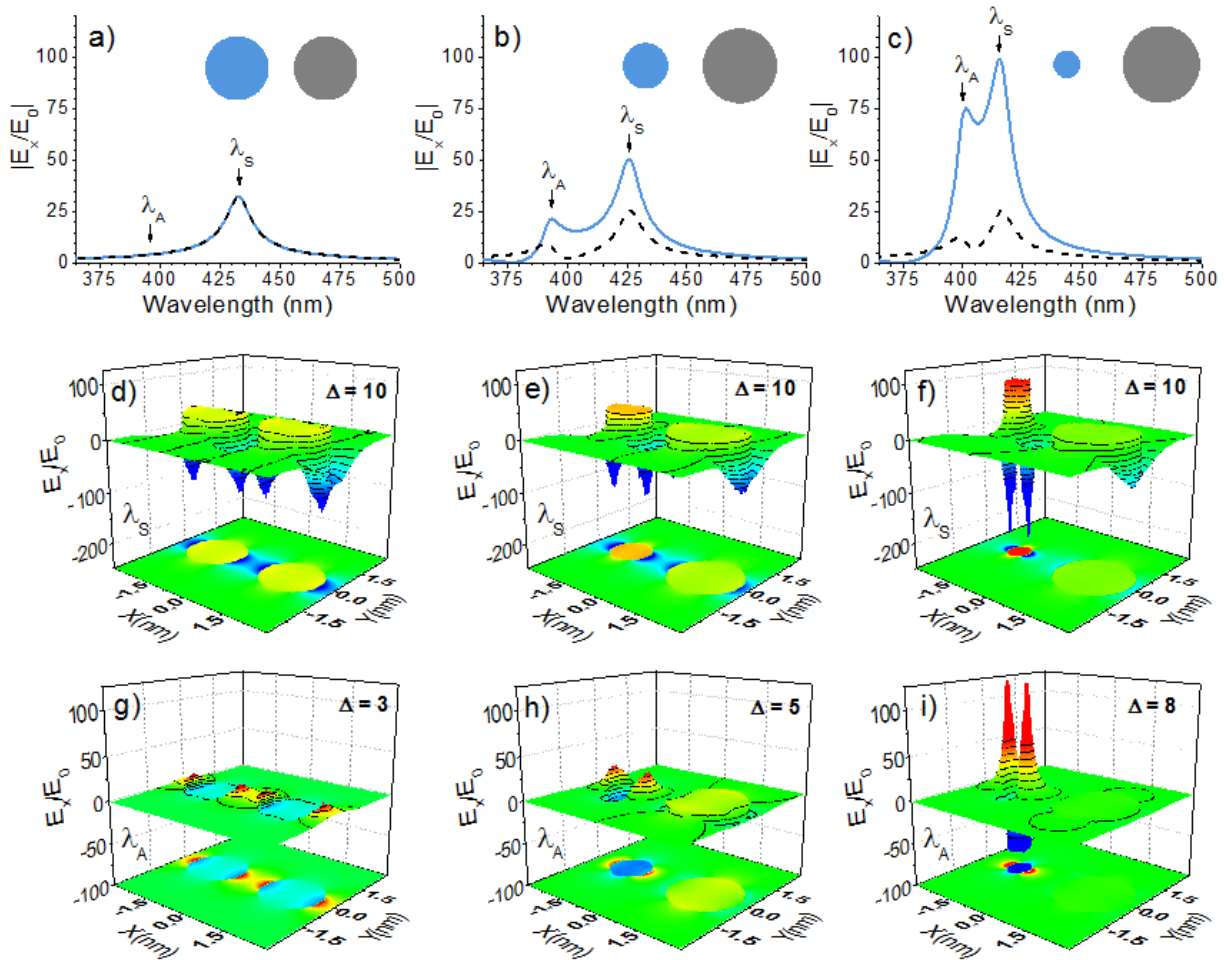
Figure 4.3: Magnitude of the electric field enhancement factor inside adjacent nanoparticles for a) identical sizes, b) a volume ratio of 4.8, and c) a volume ratio of 30, as well as the corresponding field enhancement distributions at a fixed phase for the frequencies labeled λ_S (d-f) and at the frequencies labeled λ_A (g-i). The field enhancement difference Δ between adjacent contour lines is indicated on each contour graph.

48

The cascaded field enhancement observed in Figure 4.3 suggests that these composites will exhibit a strongly enhanced nonlinear optical response at specific excitation wavelengths, at least for material located near the smaller particle. In this study, the complex nonlinear refractive index follows from the third-order nonlinear susceptibility $\chi^{(3)}$, as discussed in the introduction, and the contribution of the higher order susceptibilities in the nonlinear absorption and refraction is neglected. The overall enhancement of the nonlinear refractive and absorptive response of a Kerr-type composite can be extracted based on calculated linear field distributions and knowledge of the nonlinear susceptibilities of the materials in the structure. Under excitation of the structure with x-polarized light at a single frequency, the effective third order nonlinear susceptibility of the composite $\chi_{\text{eff}}^{(3)}$ at the fundamental frequency can be written as

$$\chi_{eff}^{(3)}(\omega) = f g_{in}^{(3)}(\omega)\chi_{in}^{(3)}(\omega) + (1-f)g_h^{(3)}(\omega)\,\chi_h^{(3)}(\omega), \qquad (4.1)$$

where f is the fill fraction of metal, and $g_{in}^{(3)}$ and $g_h^{(3)}$ are the complex nonlinear susceptibility enhancement factors of the metal and host respectively as derived from the simulated frequency dependent linear electric field distribution $\vec{E}(\omega, r)$ through the relation

$$g_j^{(3)} = \frac{\left\langle \vec{E}^2 \left|\vec{E}\right|^2 \right\rangle_{V_j}}{\left\langle \vec{E}\right\rangle_V^2 \left|\left\langle \vec{E}\right\rangle_V\right|^2} \qquad (4.2)$$

where the notations $\langle\quad\rangle_{V_j}$ and $\langle\quad\rangle_V$ indicate spatial averaging over the volume of component j and over the total simulation volume respectively. The derivation of this relation and the associated integration method used in this Chapter are described in detail in Appendix C. Frequency and position arguments have been omitted for simplicity of notation. The complex nature of the

enhancement factors manifests itself predominantly around resonances, where local fields occur with significant phase delays relative to the incident field.

Figure 4.4 shows the phase and magnitude of the obtained third order nonlinear susceptibility enhancement factor $g_{metal}^{(3)}$ of the nonlinear response of the nanoparticles. For identically sized particles (red curve) a maximum enhancement of 2.0×10^6 is obtained at the wavelength corresponding to the symmetric resonance ($\lambda = 432$ nm). Note that the phase of the enhancement at this frequency is close to π. This implies that plasmon resonant particles composed of a metal with large positive imaginary $\chi_{in}^{(3)}$ will produce a composite response $\chi_{eff}^{(3)} = f\, g_{in}^{(3)}\, \chi_{in}^{(3)}$ that is large and negative, resulting in the appearance of saturable absorption at the plasmon resonance wavelength.
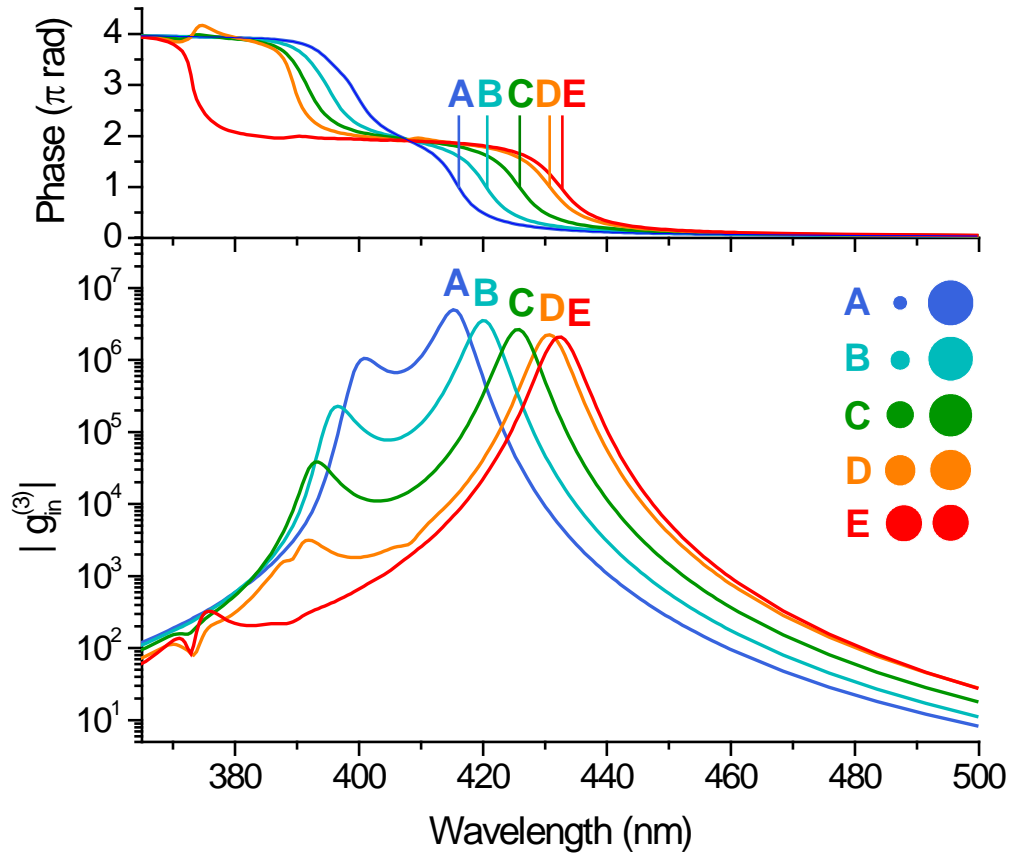
Figure 4.4: Phase (a) and magnitude (b) of the internal complex nonlinear susceptibility enhancement factor for nearest-neighbor volume ratios of 1, 2.3, 4.8, 11, and 30 for a metal fill fraction of 0.01. The legend shows the corresponding unit cell of the periodic metamaterial.

As the size difference between nearest neighbors increases, the magnitude of the enhancement for the symmetric mode gradually increases by a factor 2.4, while the phase at the wavelength for maximum enhancement remains approximately π. Additionally, the introduction of a finite size difference is seen to lead to a nonlinear susceptibility enhancement at wavelengths near the anti-symmetric plasmon resonance. This enhancement is much weaker than that of the

51

symmetric mode, however its magnitude increases rapidly as the size difference is increased. The phase of the enhancement factor reaches values close to 3π at the anti-symmetric resonance frequency, physically equivalent to the phase response at the symmetric mode wavelength. However, at wavelengths in between the symmetric and anti-symmetric resonances, the enhancement factor remains high while exhibiting a phase close to $\sim 2\pi$. This represents a new enhancement regime that does not occur in the composite with only a single particle size. At these wavelengths, plasmon resonant metals with a predominantly imaginary $\chi^{(3)}$ response could be used to obtain composites with a positive imaginary $\chi_{\text{eff}}^{(3)}$, corresponding to *enhanced nonlinear absorption*. Note that this frequency range also corresponds to a region of low linear absorption (see Figure 4.2), suggesting that a simultaneous enhancement of nonlinear absorption and an improvement of the useful interaction length can be achieved in a single composite design.
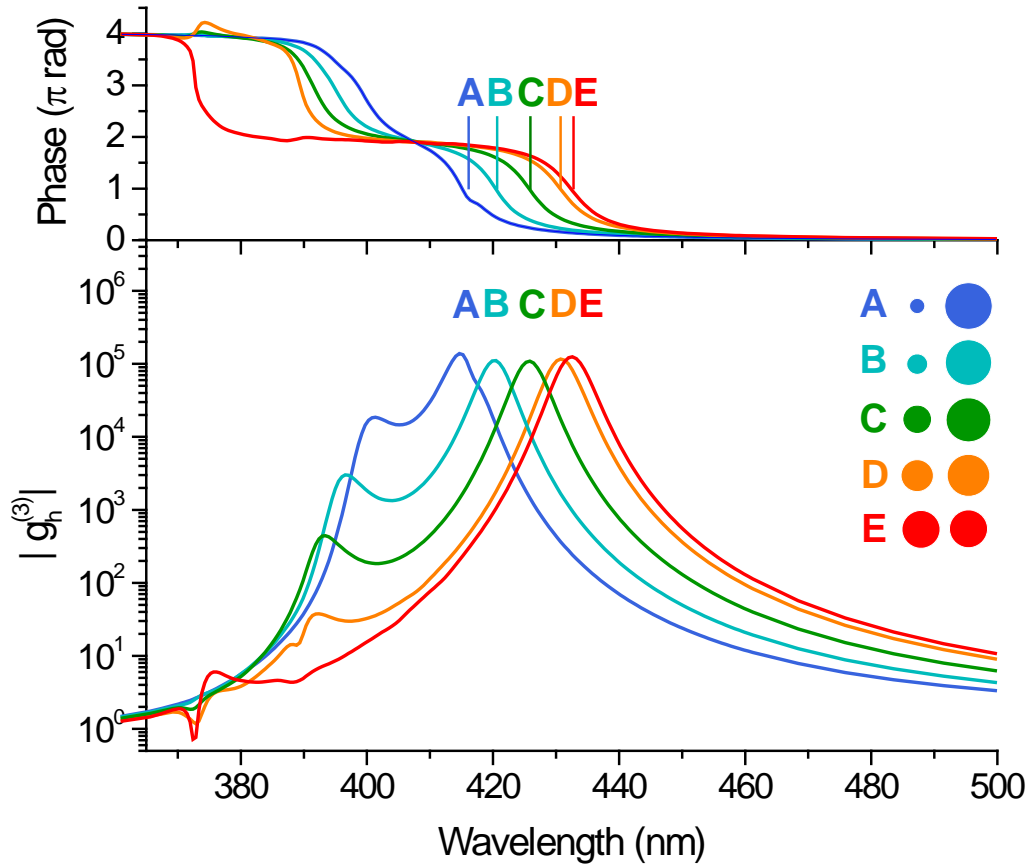
Figure 4.5: Phase (a) and magnitude (b) of the external complex nonlinear susceptibility enhancement factor for nearest-neighbor volume ratios of 1, 2.3, 4.8, 11, and 30 for a metal fill fraction of 0.01. The legend shows the corresponding unit cell of the periodic metamaterial.

Figure 4.5 shows the phase and magnitude of the obtained third order nonlinear susceptibility enhancement factor $g_h^{(3)}$ of the nonlinear response of the host material, here assumed to have a refractive index of n=1.5. The results show similar trends as the nonlinear response enhancement factors of the nanoparticle. The maximum third order nonlinear susceptibility enhancement factor for the metal nanoparticles is 35 times larger than that for host material, but it

53

should be noted that according to Equation (4.1) the total nonlinear susceptibility contribution of the metal must take into account the fill fraction f which in this case is 0.01. More importantly, the third-order susceptibility of metal is often larger than that of common dielectric host materials which is in order of 10^{-20}-10^{-22} m^2/V^2. Therefore, the nonlinear response of metal-dielectric composites will often be dominated by the nonlinear response introduced by the metal inclusions.

To understand the observations in Figure 4.4, we consider the nonlinear optical absorption as the consequence of a perturbed linear response. At high irradiance, the absorption spectrum of the composite is expected to undergo small changes due to a nonlinearly induced modification of the polarizability of the materials involved. The addition of a small imaginary part to the metal dielectric function, which is expected to occur at high irradiance, will lead to a broadening of plasmon resonances in the system. To illustrate this effect, Figure 4.6(a) shows the calculated absorption spectrum of a structure with volume ratio 30 (solid line), and the absorption spectrum of the same structure where the electron scattering rate γ_{Ag} has artificially been increased by 50% (dashed line) to mimic the metal nonlinear response. The resulting change in the dielectric function is seen to lead to a broadening of the symmetric and anti-symmetric modes as well as a change in the peak absorption values. This effect indeed causes a rise in the absorption coefficient in the area between the two resonance peaks, corresponding to the previously predicted composite nonlinear absorption.
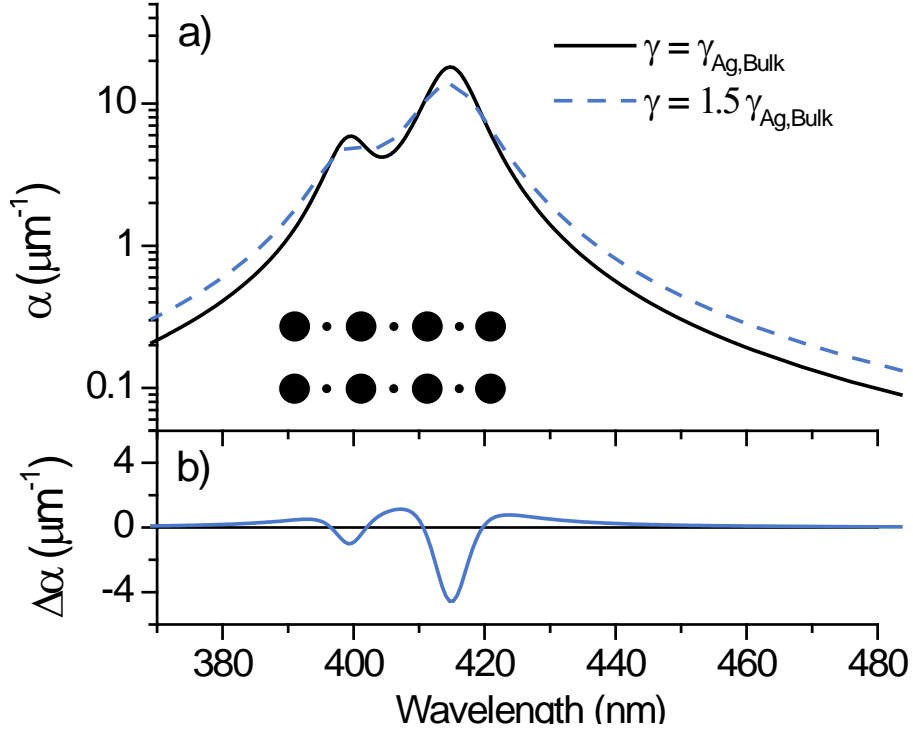
Figure 4.6: a) Absorption coefficient of a cascaded plasmonic metamaterial with a volume ratio of 30 calculated using a Drude fit to the literature data for the silver dielectric function (solid line), and of the same structure with the electron scattering rate γ_{Ag} artificially increased by 50% (dashed line), and b) the difference between the curves in a) indicating reduced absorption at the resonance peaks, and increased absorption at frequencies between the resonances.

The performance of nonlinear optical refractive or absorptive materials is typically evaluated in terms of a figure of merit (FOM), often defined as $|\chi^{(3)}|/\alpha$, or in the specific case of nonlinear absorption as β/α, where β is the nonlinear absorption coefficient. Due to the complex nature of both $\chi^{(3)}$ and the third order susceptibility enhancement factors $g^{(3)}$, it is non-trivial to assign a generally applicable figure of merit. Here we define a complex enhancement FOM given

by $g^{(3)}/\alpha$, which represents the ability of a given cascaded plasmon resonant metamaterial to enhance the nonlinear optical response. Figure 4.7 shows the obtained complex enhancement FOM for the array with a single particle size, and for the array with a nearest-neighbor volume ratio of 30, displayed on the same relative scale. The symbols correspond to simulated data points, while the solid lines provide a guide to the eye. For the structure containing particles with a single size (red curve), the largest enhancement FOM occurs at a complex phase of π corresponding to a predominantly real negative enhancement factor. This occurs at the main dipolar plasmon resonance wavelength of the structure, marked λ_S in Figure 4.3 (a). The cascaded structure with a volume ratio of 30 (blue curve) however shows a completely different range of complex enhancement FOM values. First, at any complex phase the cascaded structure can provide an improved enhancement FOM. Second, a completely real and *positive* enhancement FOM is obtained in the cascaded structure, occurring at frequencies between the symmetric and anti-symmetric modes. This shows that despite the relatively low field enhancement at wavelengths between λ_A and λ_S, the corresponding moderate linear absorption at these intermediate wavelengths enables a figure of merit that dramatically exceeds that of the non-cascaded composite.
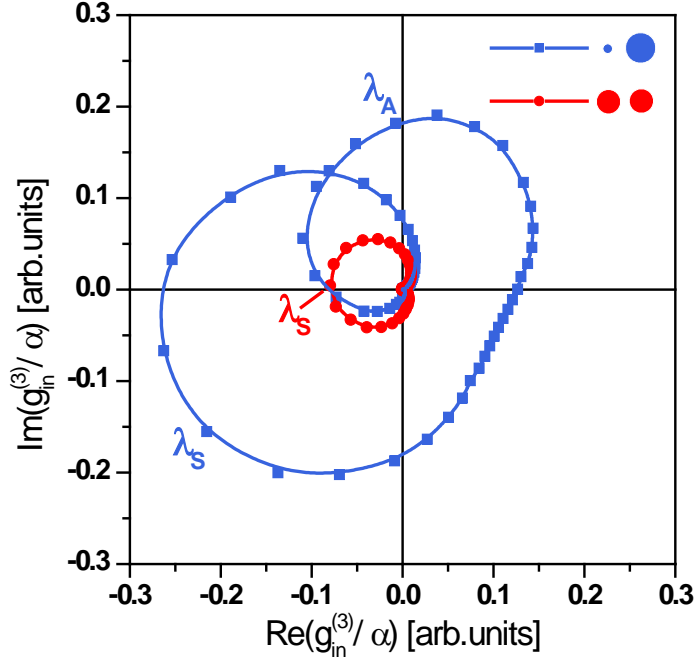
Figure 4.7: Complex enhancement figure of merit of the third order nonlinear optical response of a plasmonic metamaterial containing silver nanoparticles with a single size (radius 1 nm), and of a cascaded plasmonic metamaterial with a nearest-neighbor volume ratio of 30. The legend shows the corresponding unit cell of the periodic metamaterial. The labels λ_A and λ_S correspond to the anti-symmetric and symmetric mode respectively.

To illustrate the effect of the complex enhancement factors that can be achieved in cascaded plasmon resonant structures, Figure 4.8 shows a specific example evaluating the FOM for nonlinear absorption, given by β/α with β the nonlinear absorption coefficient. We assume that the metal $\chi^{(3)}$ response is well described by a Kerr-type response with a predominantly positive imaginary response given by $Im(\chi^{(3)}) = 10^{-16}$ m^2/V^2. For the array with a single particle size, this is seen to lead to a small positive FOM for nonlinear absorption at frequencies above and below

the plasmon resonance, while a large and negative figure of merit is found at the plasmon resonance frequency, indicative of saturable absorption rather than enhanced nonlinear absorption. This behavior can be understood in terms of a nonlinearly induced broadening of the plasmon resonance, using a similar analysis to that shown in Figure 4.6.
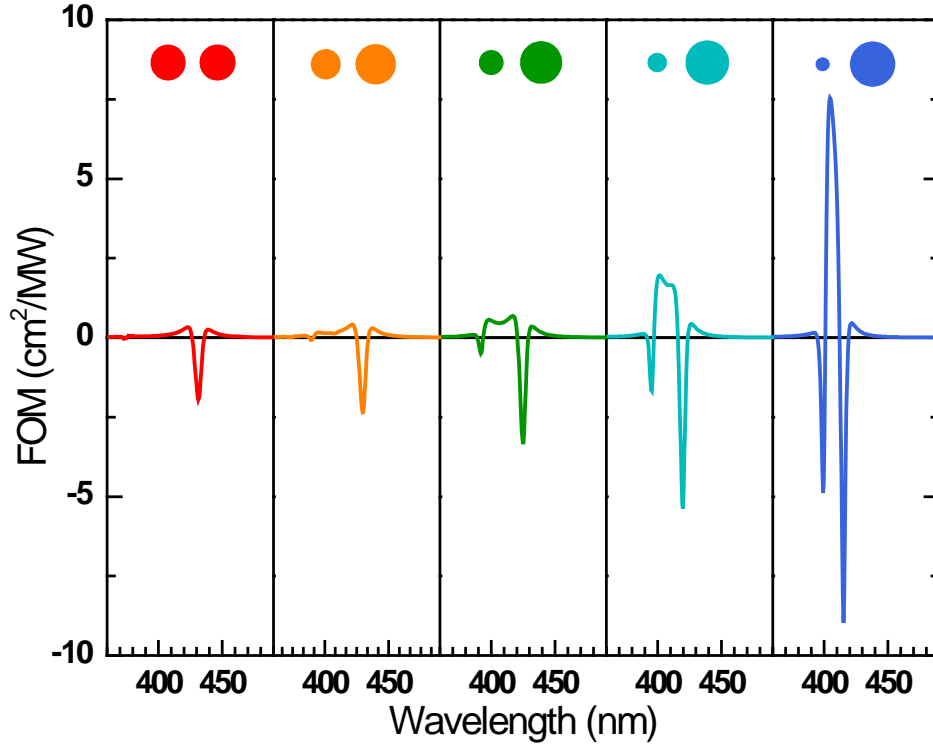
Figure 4.8: Calculated figure of merit for nonlinear absorption assuming $Im(\chi^{(3)}) = 10^{-16}$ m^2/V^2 for cascaded plasmon resonant metamaterials with different nearest neighbor particle volume ratios of 1, 2.3, 4.8, 11, and 30. The corresponding unit cell of the period structures is indicated schematically. An improvement of the figure of merit for nonlinear absorption by a factor 20 is observed as the nearest-neighbor volume ratio is increased from 1 to 30.

As the particle size difference within the array increases, both the anti-symmetric and symmetric modes produce an increasingly strong negative FOM. However at wavelengths between the two resonances, a rapidly increasing positive figure of merit develops, ultimately reaching a value that is a factor 20 larger than the maximum value observed using a single particle size. It should be pointed out that depending on the excitation pulse length and frequency, $\chi_{in}^{(3)}$ itself can

take on various complex phases and magnitudes, and as such Figure 4.8 should be taken primarily as a demonstration of the practical implications of the complex nature of the enhancement factors. Nevertheless, effects such as those in Figure 4.8 are predicted to be observable in frequency dependent nonlinear optical measurements on cascaded plasmon resonant structures.

It is important to stress that the results shown above were obtained in the quasi-electrostatic limit in the absence of surface scattering. At the small particle sizes simulated here, surface scattering would significantly alter the surface plasmon damping, leading to reduced field enhancement factors and lower figures of merit for nonlinear refraction and absorption, albeit over a larger frequency bandwidth. For this reason any experimental implementation of the discussed approach would require larger particle sizes and likely larger inter-particle spacing. Similar calculations in which all dimensions are scaled up by a factor 10 (not shown) yield very similar results both in linear and nonlinear optical response while remaining in the effective medium limit (no diffractive effects present in the frequency region of interest). These results strongly suggest that the predicted response can be obtained using experimentally viable particle sizes with reduced surface scattering effects.

Finally, while these effects were calculated assuming pure Kerr-type nonlinearities, the fundamental physical interactions that produce the effects discussed here are related to the presence of coupled nonlinear resonators. Consequently, similar enhancement effects are expected to appear in systems that exhibit non-Kerr type third order optical nonlinearities, including thermal nonlinearities.

4.4. Summary

The use of cascaded plasmon resonances for the enhancement of nonlinear optical refraction and absorption was found to lead to complex enhancement factors and a complex enhancement figures of merit that strongly depend on the nearest-neighbor volume ratio. By varying the size difference between adjacent particles the plasmon resonant metamaterial is gradually adjusted from the non-cascaded to the cascaded regime. Cascaded plasmon resonances were found to increase the attainable nonlinear susceptibility enhancement factors and figure of merit for nonlinear absorption using metals with a positive imaginary third order nonlinear optical susceptibility. The complex enhancement factors in the cascaded systems are found to be a large *positive* enhancement factor, despite, the imaginary or negative nature of that in the arrays containing a single particle size. This type of phase-optimized design of the nonlinear optical response enhancement in cascaded plasmon resonant metamaterials could lead to the development of new optical switching materials with a performance that dramatically exceeds that of their non-cascaded counterparts.

5. PHOTOTHERMAL RESPONSE ENHANCEMENT IN HETEROGENEOUS PLASMON RESONANT NANOPARTICLE TRIMERS

5.1. Introduction

As discussed in Chapters 2-4, large field enhancement factors can be achieved in cascaded nanoparticle structures with large polarizability differences. In nanosphere dimers, this leads to the requirement of large volume ratios, leading to the necessity of using very small particles that exhibit large damping due to surface scattering, or using large particles in which the field enhancement is reduced due to retardation effects. This makes the practical achievement of cascaded field enhancement difficult. In this Chapter, we investigate the combination of near-field induced resonance shifts and composition dependent plasmon resonance energies to provide an alternate method for achieving large polarizability differences. In particular, we analytically and numerically investigate the optical response of heterogeneous plasmonic trimer structures composed of a silver nanoparticle dimer and a central gold nanoparticle. The plasmon resonance of the silver dimer is controlled through near-field coupling, allowing for a frequency overlap of the silver and gold plasmon resonances. The resulting increased field enhancement in this multi-material trimer structure makes it possible to increase the energy dissipation per unit volume by over two orders of magnitude compared to a single-particle plasmon resonant system. Furthermore it is predicted that pulsed illumination of a trimer consisting of two 80 nm diameter silver particles and a 10 nm diameter central gold particle can raise the gold particle temperature by 100 K using as little as 20 nJ/mm^2 at a wavelength of 530 nm. This finding may have practical applications in

photothermal therapy, fast thermal nonlinear optical modulation, and could enable new thermal studies at picosecond time scales.

Heat generation in metallic nanoparticles under optical illumination has recently attracted enormous interest, having found applications in photothermal therapy[35, 36, 40-42], drug delivery[37-39],, photothermal imaging [30-32], optoacoustic imaging[33, 34], bubble formation for nanosurgery [74-78] and purifying liquids[79, 80], material growth [81], nano-welding [43, 44], heat-assisted magnetic recording[82] and photothermally controlled fluidics[83, 84]. In metallic nanoparticles, plasmon resonances lead to enhanced optical absorption, followed by heating of the free electron gas through electron-electron scattering on a time scale of ~100 fs[96]. The increased electron temperature leads to a non-equilibrium electron energy distribution function, an effect known as Fermi smearing, resulting in an ultrafast nonlinear optical response[55, 97-99]. Subsequently the electron gas exchanges energy with the metal lattice through electron-phonon scattering on a time scale of 2-3 picoseconds[100] bringing the electronic and vibrational temperature in equilibrium. If the metal nanoparticle is embedded in a medium with moderate thermal conductivity, this is followed by heat transfer to the surrounding medium on a ~100 ps time scale. This is a notably short time for a thermal effect, which is the result of the highly confined heat generation and the large surface-to-volume ratio of typical nanometric plasmonic structures. The combination of plasmon enhanced optical absorption and rapid heat dissipation make metallic nanostructures a candidate for observing fast thermal optical nonlinearities at relatively low irradiance.

Given the broad applicability of the plasmonic photothermal effect, it is of interest to find ways of maximizing the attainable temperature change for a given optical irradiance. In the present

manuscript we achieve this by using a compositionally heterogeneous trimer structure consisting of a relatively high-volume plasmon resonant dimer with a small-volume plasmon resonant monomer. The optical properties of compositionally heterogeneous plasmonic structures have been previously investigated theoretically [139, 140], however these studies did not achieve strongly coupled resonances due to a significant resonance mismatch between the different nanospheres. Related experimental studies in the context of gas sensing [141, 142] and signal routing [143, 144] demonstrated the benefit of combining different materials into coupled systems, but did not achieve large field enhancement factors due to either the presence of a resonance frequency mismatch of the plasmonic elements or the introduction of large damping by one of the materials used (Pd). In contrast to these studies, we demonstrate that a plasmonic trimer composed of a silver dimer and a gold monomer can exhibit strong resonant interactions between the different materials, enabling the achievement of large field enhancement and the generation of a temperature change that exceeds that of isolated gold nanoparticles by over two orders of magnitude. The presented approach uses elements of the 'plasmonic nanolens' introduced by Li *et al*. [89], which relied on coupled resonances between nanospheres with identical composition in order to achieve large field enhancement factors. In the present study we show that judiciously chosen near-field induced resonance shifts can be used to achieve cascaded plasmon resonances in *compositionally heterogeneous* nanosphere structures, something which could not be achieved with the geometry introduced by Li *et al*. The physical principle that makes this possible is illustrated in a point-dipole coupling model, and confirmed by numerical simulations of an experimentally realistic nanoparticle trimer. This general approach presented here can be extended to a broad range of

nanoparticle sizes and compositions, and offers new opportunities for optimizing plasmon enhanced phenomena.

5.2. Theory

To optimize the photothermal response in plasmonic nanostructures we monitor the ratio of the absorption cross-section σ_{abs} to the nanoparticle volume. This choice can be understood by considering the temperature change achieved after short-pulse irradiation, as described briefly in the following. In metallic nanoparticles under pulsed illumination the deposited optical energy $E_{abs}(J)$ causes plasmon mediated heating in the nanoparticle. In the absence of significant heat exchange with the environment, i.e. for short times after the pulse, the resulting particle temperature increase is given by $\Delta T(K) = E_{abs}/(\rho_{NP}V_{NP}c_{NP})$ with $\rho_{NP}(kg \cdot m^{-3})$ the density of the particle, $V_{NP}(m^3)$ the particle volume and $c_{NP}(J.kg^{-1}.K^{-1})$ the specific heat capacity of the particle, assuming that the specific heat is approximately temperature independent. The absorbed energy is $E_{abs} = \sigma_{abs}\,\varphi$ with $\sigma_{abs}(m^2)$ the optical absorption cross-section and $\varphi(J.m^{-2})$ the optical fluence of the pulse. For a given pulse energy the resulting initial temperature rise ΔT of a nanoparticle,

$$\Delta T = \frac{1}{\rho_{NP}c_{NP}} \frac{\sigma_{abs}}{V_{NP}} \phi \tag{5.1}$$

depends only on material properties and the ratio of the absorption cross-section to the nanoparticle volume. The cross-section to volume ratio can be interpreted as a relative absorption coefficient, equivalent to the particle-related absorption coefficient $\alpha = \sigma_{abs}\,N_{NP}$ divided by the volume fill

fraction $f = N_{NP} V_{NP}$ of a suspension containing N_{NP} particles per unit volume. For spherical metallic nanoparticles in the quasi-electrostatic limit the relative absorption coefficient becomes size-independent and peaks at the localized plasmon resonance frequency ω_{LSP} with a magnitude given by

$$\left(\frac{\sigma_{abs}}{V_{NP}}\right)_{\omega_{LSP}} = 9 \frac{\omega_{LSP}}{c} \frac{n_h^3}{\varepsilon_{NP}''} \tag{5.2}$$

where c is the speed of light in vacuum, n_h is the refractive index of the host and ε_{NP}'' is the imaginary part of the dielectric function of the metal particle at ω_{LSP}. For gold nanoparticles in an aqueous host the peak relative absorption coefficient is ~0.083 nm^{-1} at a wavelength of 515 nm, leading to a $\Delta T/\varphi = 33$ K / (μJ/mm^2). To achieve maximum nanoparticle heating for a given pulse energy this relative absorption must be optimized. Here we use the strong optical field in the gap of a dimer composed of a high-plasma-frequency metal to drive the plasmon resonance of a smaller nanoparticle composed of a material with a lower plasma frequency.
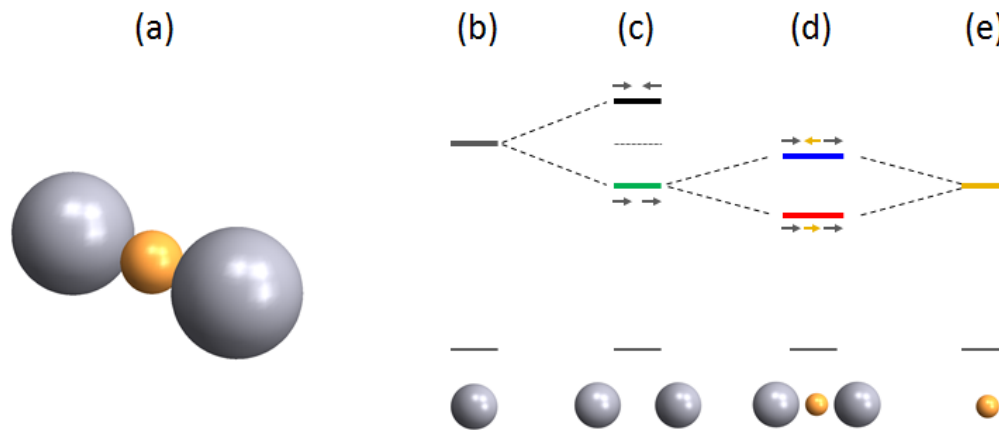
Figure 5.1: a) Schematic of a heterogeneous Ag-Au-Ag trimer, and energy diagrams showing b) the dipolar plasmon mode of an isolated silver nanoparticle, c) the bonding (green) and anti-bonding (black) resonance modes of a silver dimer, d) the bonding (red) and anti-bonding (blue) modes of an Ag-Au-Ag nanosphere trimer and e) the dipolar plasmon resonance mode of an isolated gold nanoparticle.

Figure 5.1(a) shows an illustration of the type of heterogeneous trimer structure under investigation. The trimer is bimetallic, and consists of a gold nanoparticle located between two silver nanoparticles. This system supports various coupled plasmon resonances which can be understood in terms of hybridization of modes of the separate elements in the structure, as schematically shown in Figures 5.1 (b-e). Figure 5.1 (b) and Figure 5.1 (e) show energy level diagrams corresponding to the dipolar plasmon resonance energies of isolated silver and gold nanospheres in water (n=1.33) which lie at 3.25 eV and 2.42 eV, respectively. Due to the large mismatch between these energies, Au and Ag nanoparticles are not expected to show strong plasmonic interaction. Figure 5.1 (c) shows the energies of coupled dipolar plasmon resonances

on a silver nanosphere dimer for modes polarized along the dimer axis. Near-field interactions between the closely spaced silver nanoparticles induce polarization dependent mode splitting, resulting in the development of a low-energy bonding mode where electrons in both particles oscillate in-phase, and a high-energy anti-bonding mode where the electrons in each particle oscillate in anti-phase[124]. For sufficiently strong inter-particle interaction (small spacing), the energy of the bonding silver dimer mode may approach the resonance energy of an isolated gold nanoparticle, as indicated schematically by the green horizontal line in Figure 5.1 (c). This type of near-field induced resonance shift of the silver dimer provides a method for achieving strong coupling between plasmon resonances in heterogeneous particle systems. Figure 5.1 (d) shows two anticipated coupled resonances when a trimer is composed of a gold nanosphere and the silver dimer from Figure 5.1 (c). Coupling between the bonding mode of the silver dimer and the dipolar resonance of the gold monomer is expected to lead to the development of hybridized modes, exhibiting a low-energy bonding mode where the dipole moment of all particles oscillates approximately in phase, and a higher energy anti-bonding mode where the Au dipole moment and Ag dipole moment oscillate in anti-phase, as indicated schematically by the arrows in Figure 5.1 (d). This coupling of a high-polarizability resonator to a low polarizability resonator is expected to produce large field enhancement factors and consequently large concentration of energy dissipation.

5.3. Point Dipole Model

To investigate the evolution of hybridized plasmon modes as a function of particle polarizability in heterogeneous trimer structures we first consider an analytical point dipole-dipole interaction model. Each particle in the trimer is modeled as a point dipole with polarizability $\alpha_i = 3\varepsilon_0\varepsilon_h V_i(\varepsilon_i - \varepsilon_h)/(\varepsilon_i + 2\varepsilon_h)$ where V_i is the volume of nanoparticle i, and ε_i and ε_h are the dielectric function of particle i and the host, respectively. The dipole moment of particle i at location $\mathbf{r_i}$ is given by $\mathbf{p_i} = \alpha_i \mathbf{E}_{loc}(\mathbf{r_i})$, where $\mathbf{E}_{loc}(\mathbf{r_i}) = \mathbf{E}_{inc}(\mathbf{r_i}) - \Sigma \mathbf{A_{ij}} \mathbf{p_j}$ represents the local field experienced by particle i due to the incident electric field $\mathbf{E}_{inc}(\mathbf{r_i})$ and neighboring dipoles j with $\mathbf{A_{ij}}$ the dipole-dipole interaction matrix between dipoles i and j. Here we consider a centrosymmetric linear trimer structure consisting of two identical outer particles 1 and 3 and a central particle 2, excited by light incident normal to the trimer axis and polarized along the trimer axis. Under these conditions we have $\alpha_1 = \alpha_3$ and $p_1 = p_3$, and scalar matrix elements A_{ij} given by

$$A_{ij} = \frac{e^{ikd_{ij}}}{2\pi\varepsilon_0\varepsilon_h}\left(\frac{ik}{d_{ij}^2} - \frac{1}{d_{ij}^3}\right) \tag{5.3}$$

where d_{ij} is the center-to-center separation between particles i and j, and k is the wavevector in the host medium. Solving for the dipole moment of the central particle (i=2) leads to

$$p_2 = \alpha_2 \frac{1 + \alpha_1 A_{13} - 2\alpha_1 A_{12}}{1 + \alpha_1 A_{13} - 2\alpha_1\alpha_2 A_{12}^2} E_{inc}. \tag{5.4}$$

The obtained dipole moment can be converted to a predicted internal field enhancement of particle 2 using its known field enhancement factor $g_{in,2} = E_{in,2}/E_{loc}(r_2) = 3\varepsilon_h/(\varepsilon_2 + 2\varepsilon_h)$ with $E_{in,2}$ the internal field in particle 2, resulting in

$$\frac{E_{in,2}}{E_{inc}} = \frac{1 + \alpha_1 A_{13} - 2\alpha_1 A_{12}}{1 + \alpha_1 A_{13} - 2\alpha_1\alpha_2 A_{12}^2} \, g_{in,2} \cdot \tag{5.5}$$

This equation is used to investigate mode hybridization and field enhancement factors in model trimers consisting of outer particles described by a Drude dielectric response with a high plasma frequency $\omega_{pA} = 9\times10^{15}$ rad/s and a low electron scattering rate $\gamma_A = 1\times10^{14}$ s^{-1} and a central particle with a lower plasma frequency $\omega_{pB} = 8\times10^{15}$ rad/s with a high electron scattering rate of $\gamma_B = 5\times10^{14}$ s^{-1}, embedded in an aqueous host with dielectric constant $\varepsilon_h = 1.77$. Figure 5.2 follows the same color coding as Figure 5.1, and shows the evolution of the obtained plasmon resonance energies of the symmetric bonding mode (all dipoles in-phase, red line) and the anti-bonding mode (central dipole in anti-phase with outer particles, blue line) in heterogeneous trimers where the diameter of the outer particles is set to 80 nm, the diameter of the central particle D_2 is varied from 0 to 80 nm, while the edge-to-edge spacing is held fixed at 5 nm. For comparison, the bonding resonance of the equivalent isolated dimers is included (green dotted line, top axis), as well as those of isolated outer and central particles (black and gold dashed horizontal lines respectively). The presence of a large central particle in the trimer is seen to lead to large mode splitting between the bonding and anti-bonding modes, approximately centered around the resonance energy of the isolated central particle (gold dashed line). This is the result of the strong interaction of the central particle with each outer particle, and the relatively weak interaction between the outer particles at the relatively large separation between particles 1 and 3 (d_{13}, top axis). As the diameter of the central particle is reduced, the influence of the central particle on the trimer resonances diminishes, causing the mode splitting to reduce while the central resonance moves closer to that of the isolated dimer. Note that for a central particle diameter of 3.45 nm, the small physical separation between

70

outer particles causes the dimer resonance to match that of an isolated central particle (level alignment as in Figure 5.1 (c)), while at the same time the small polarizability of the central particle leads to relatively small mode splitting. This condition leads to large field enhancement, as shown below.
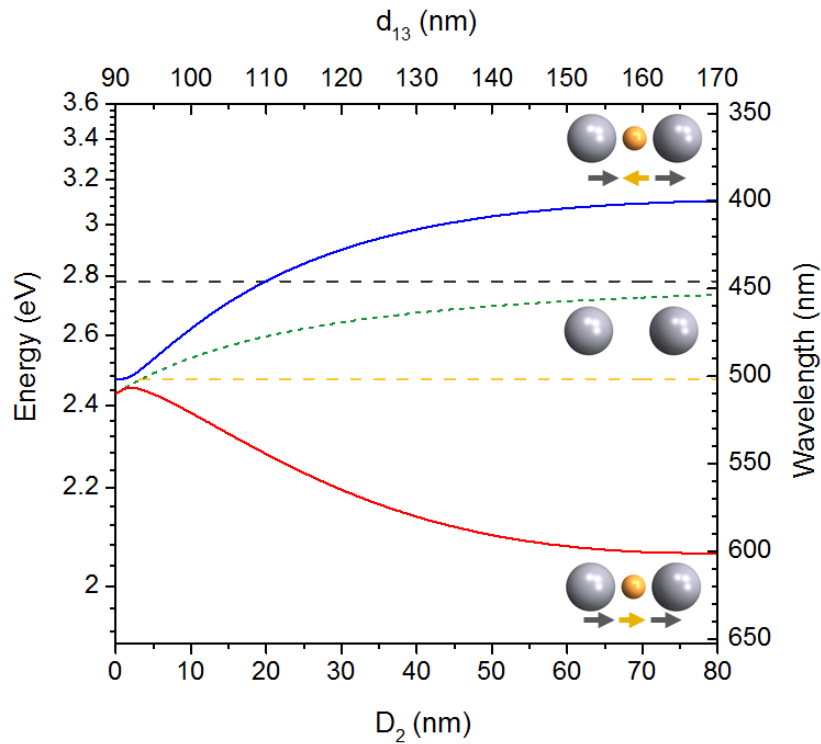
Figure 5.2: Plasmon resonance energies of a heterogeneous nanoparticle trimer composed of a high plasma frequency dimer and a low plasma frequency central particle, as well as the resonance energies of isolated outer (black dashed line) and central nanoparticles (gold line), and of the bonding mode of an isolated dimer (green dotted line).

Figure 5.3 shows the magnitude of the internal electric field enhancement factor in the central particle for the same parameters as used in Figure 5.2. At large volume of the central

particle, only moderate field enhancement values of the order of 10 are observed for both the bonding and the anti-bonding modes. As the volume of the central particle is reduced, the mode splitting decreases and the field enhancement rises dramatically. This can be understood by noting that for small central particle size, the dimer resonance matches the resonance of the central particle, while the high damping rate of the central particle has relatively little effect on the dimer resonance due to its small volume. Under these conditions the dimer acts as an excitation source for the smaller central particle, which in turn produces its own field enhancement. This effect is analogous to the 'plasmonic nanolens'[89], but extended to nanospheres with varying composition. Note that the bonding and anti-bonding modes cannot be distinguished for small central nanoparticle sizes due to the small mode splitting compared to their resonance linewidths.
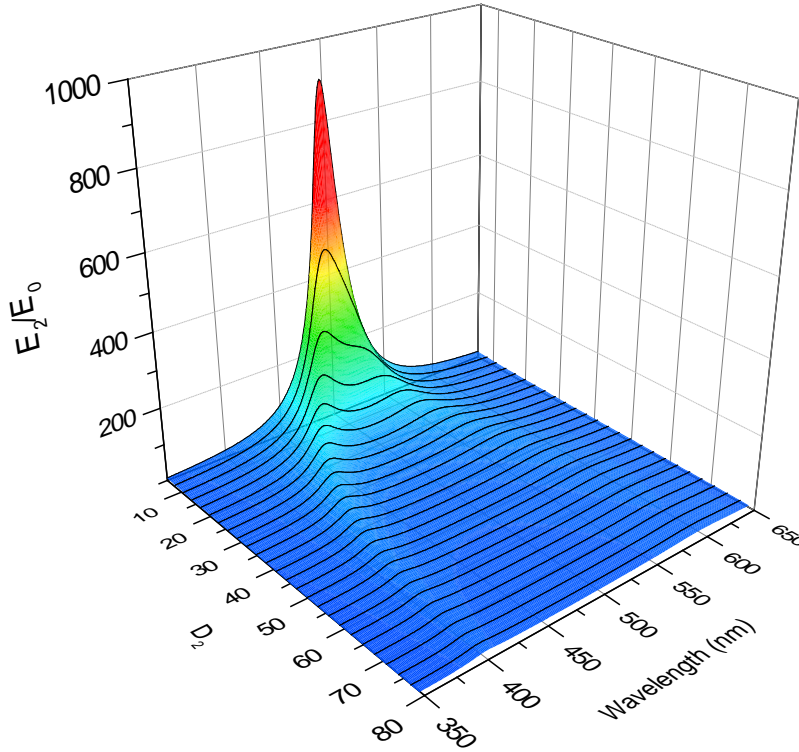
Figure 5.3: Internal field enhancement spectra of the central nanoparticle in heterogeneous nanoparticle trimers composed of a low-loss, high plasma frequency dimer, and a high loss, low plasma frequency central nanoparticle as a function of central particle diameter D2.

5.4. Results

To evaluate the feasibility of optimizing field enhancement and the photothermal response in realistic heterogeneous trimer structures we simulated the electric field distribution in Ag-Au-Ag trimers using the three-dimensional frequency domain finite integration technique[87]. This method takes into account radiative losses and allows for multipolar plasmons, aspects that are not included in the point-dipole model discussed above. A Drude fit to literature data was used

for the dielectric function of silver[145], while a polynomial fit to literature data for gold[103] was used to avoid simulation artifacts related to the relatively large noise in the experimental values for the imaginary part of ε_{Au}. The silver nanoparticle diameter and edge to edge spacing were held at 80 nm and 5 nm, while the gold nanoparticle diameter was varied between 5 nm and 80 nm. Note that these sizes and inter-particle spacings are experimentally achievable. The trimer is oriented along the x-axis and excited using an x-polarized plane wave with field amplitude E_0 and a wavevector normal to the dimer axis. Figure 5.4(a) shows the simulated internal field enhancement factor at the center of an 80 nm gold nanoparticle (solid line) in the trimer structure. The dashed line shows the field enhancement factor at the center of the gap of the corresponding isolated silver dimer, and the dotted line shows the internal field enhancement of the isolated gold nanoparticle. The dimer resonance and the gold particle resonance occur at different frequencies, leading to weak internal field enhancement in the central particle of the trimer. Figure 5.4(b) shows the corresponding results when the gold particle diameter is reduced to 40 nm. The field enhancement factor of the 40 nm diameter gold particle in the trimer structure is seen to increase significantly, which is attributed to an increased field strength from the dimer and a slight redshift of the dimer resonance toward the gold nanoparticle resonance. Figure 5.4(c) shows the results for a trimer containing a gold nanoparticle with a diameter of 10 nm. In this configuration the field enhancement at the center of the isolated dimer reaches a factor 11, and its resonance frequency closely matches that of an isolated 10 nm diameter gold nanoparticle. The internal field enhancement factor of the central particle in the trimer reaches 24, close to the product of the field enhancement from the isolated dimer and the internal field enhancement of the isolated monomer

74

of $11.9 \times 1.9 = 22.6$. In our prior work on single-composition dimers[107], we labeled this regime 'multiplicative cascading', referring to the fact that the field enhancement is well-described by the product of the enhancement factors provided by the individual elements of the structure.
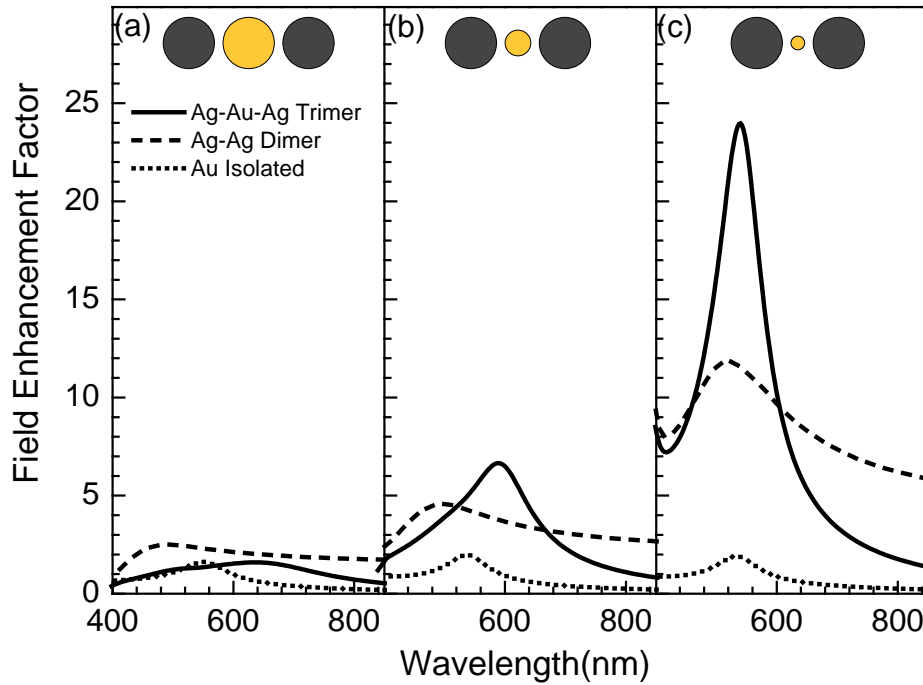
Figure 5.4: Electric field enhancement factor inside the gold nanoparticle in three Ag-Au-Ag trimer structures with a silver particle diameter of 80 nm and gold nanoparticle diameters of (a) 80 nm, (b) 40 nm, (c), and (c) 10 nm (solid lines), as well as the electric field enhancement factor in the gap of the corresponding silver dimers with the gold nanoparticle removed (dashed lines), and the electric field enhancement factor inside the corresponding gold monomers (dotted lines).

Based on the numerically simulated electric field distributions, the material-specific relative absorption coefficient σ_i/V_i can be extracted, where σ_i represents the ratio of the power dissipated in particle i to the incident irradiance on the trimer, leading to

$$\frac{\sigma_i}{V_i} = \frac{\omega\,\varepsilon_i''}{V_i n_h c} \int_{V_i} \frac{E^*(r)\cdot E(r)}{E_0^2} \, dr \, . \tag{5.6}$$

Figure 5.5 shows the thus obtained gold-related relative absorption for heterogeneous trimer structures with three different gold nanosphere sizes (solid lines), the corresponding result for the isolated gold nanoparticles at these sizes (dotted lines) as well as the silver-related relative absorption of isolated silver trimers at the same inter-particle spacings (dashed lines). The relative Au-related absorption of the trimer with an 80 nm diameter central particle (red solid line) shows a peak at 495 nm and a shoulder at ~675 nm, indicative of the previously discussed anti-bonding and bonding modes. The highest relative absorption of this structure is ~0.08 compared to 0.07 of the isolated gold particle. As the gold diameter in the trimer is reduced to 40 nm, the relative absorption is seen to increase by as much as an order of magnitude with a peak value of 0.65. Note that the corresponding results for the isolated gold particle increase by only a factor 1.4 for the same size reduction. The relative absorption spectrum of the trimer shows a peak at long wavelength and a shoulder at short wavelength. Two representative field snapshots corresponding to wavelengths λ_c = 570 nm and λ_d = 510 nm are shown in Figure 5.5 (c) and Figure 5.5 (d) respectively. At low frequency (λ_c) the field inside the silver particles and the gold particle are both seen to be positive, indicative of a bonding mode. At high frequency (λ_d) on the other hand, the field in the silver particles can be seen to be positive (green to yellow color), while the field

electric field inside the gold nanoparticle is negative (blue color), indicative of an anti-bonding mode. As the gold particle diameter is further reduced to 10 nm, the maximum relative absorption increases by another order of magnitude (blue solid line) with a maximum value of 12.7 at a wavelength of λ_b=530 nm. A snapshot of the corresponding electric field distribution at λ_b is shown in Figure 5.5 (b). Large electric field strength is observed inside the gold nanoparticle, resulting in the desired larger energy dissipation per unit volume. The response of the corresponding isolated gold particle remains unaltered for this size reduction. Continued size reduction (not shown) of the gold particle diameter D_{Au} while maintaining the chosen fixed edge-to-edge spacing of 5 nm leads to a gradual convergence to the limiting case of $(\sigma/V)_{Au} = (\omega\, \varepsilon_{Au}''/n_h c)\, \left|g_{gap}(\omega) \times g_{in,Au}(\omega)\right|^2$ where $g_{in,Au}$ is the theoretical internal field enhancement factor for a gold nanosphere in the quasi electrostatic limit, and g_{gap} represents the simulated field enhancement at the gap center of an isolated silver dimer with a 10 nm gap at this frequency. This limiting case is shown as the gray dashed line in Figure 5.5 (a). In this limit, the relative absorption of Au nanoparticles in the trimer structure exceeds that of isolated Au particles of the same size by a factor 470. Comparing these results with the previously calculated thermal sensitivity of $\Delta T/\varphi$ = 33 K / (μJ/mm^2) for isolated Au nanoparticles, the results in Fig. 5 indicate that a pulse fluence as small as 20 nJ/mm^2 at 530 nm could produce a temperature change of 100 K in these trimer structures.
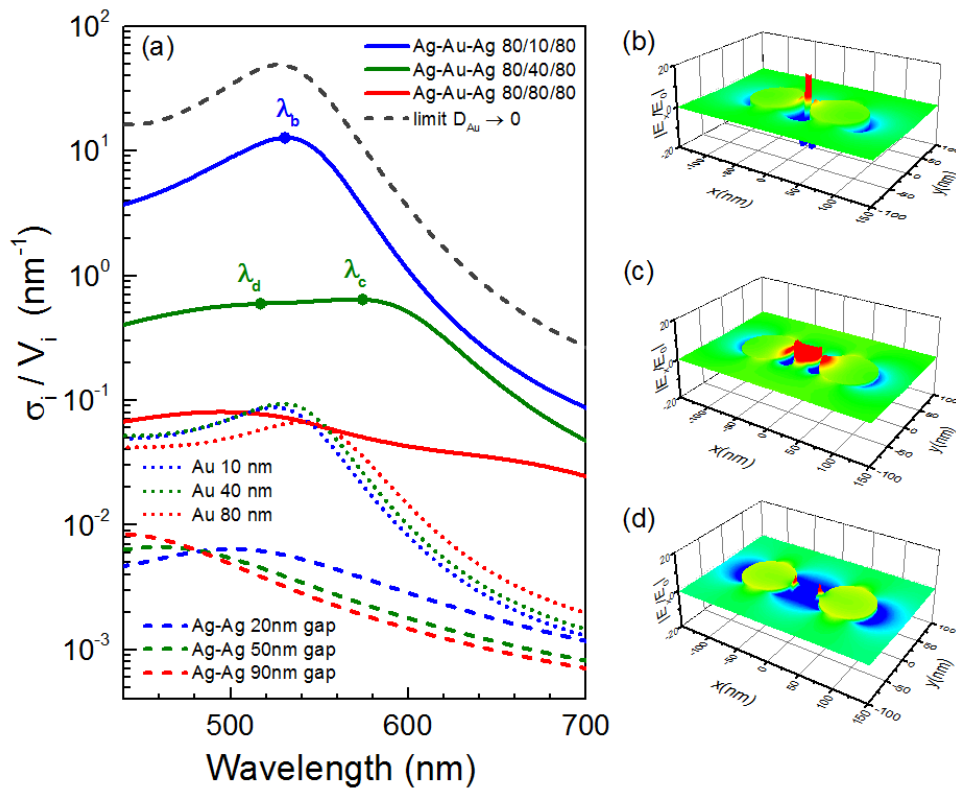
Figure 5.5: a) Gold-related relative absorption coefficient (solid lines) for nanoparticle trimers consisting of 80 nm diameter outer silver nanoparticles and a central gold nanoparticle with a diameter of 80 nm (red line), 40 nm (green line) and 10 nm (blue line) respectively, as well as the corresponding results for isolated gold particles with these same dimensions (dotted lines), and the silver-related relative absorption for the corresponding isolated silver dimers. The dashed gray line represents the analytically predicted limiting case for $D_{Au} \to 0$. b) Snapshot of the electric field distribution E_x corresponding to the case labeled λ_b in a) and the corresponding snapshots for (c) the bonding mode labeled λ_c and (d) the anti-bonding mode labeled λ_d.

78

The results presented above demonstrate that the relative absorption coefficient of gold nanoparticles can be enhanced by orders of magnitude using coupled resonances in heterogeneous or 'multi-material' few-particle structures. This optimized energy absorption in the gold nanoparticle in turn enables the achievement of rapid electron and lattice temperature changes, which is expected to lead to significantly enhanced thermal nonlinear optical response of the gold nanoparticle. In addition, the small size of the gold particles and the highly concentrated heat deposition in an otherwise non-absorbing host is anticipated to lead to rapid cooling after pulsed illumination, suggesting that any observed optical nonlinearities in such structures could occur on significantly faster time scale than commonly observed in thermal nonlinearities. The assumed particle shapes in the proposed structure are spherical, close to the thermodynamic equilibrium shape of the particles, suggesting that these structures could withstand relatively high temperatures without significant structural degradation. It should also be noted that the particle sizes simulated here are outside the regime where nonlocal and quantum effects start playing a significant role, perhaps with the exception of electronic surface scattering which is expected to introduce notable damping for Au nanoparticle diameters smaller than x nm. The latter effect was not included in the model simulations. The assumed gap size of 5 nm may be experimentally achieved using surface-charge based binding, or possibly using short organic linker molecules, potentially enabling solution processing of large quantities these photothermal plasmonic oligomers. The proposed structure may be used for the generation of nanoscale plasma, nanoscale bubbles, thermal radiation, the controlled initiation of high-temperature chemical reactions in an otherwise low-temperature host, or even the realization of unusual thermally quenched material phases as a result of the expected rapid cooling of these highly concentrated heat sources and their environment. The

proposed approach is not limited to gold and silver, and may be extended to more complex plasmonic oligomers.

5.5. Summary

In summary, we have presented a heterogeneous plasmonic trimer structure in which careful optimization of inter-particle spacing enables the overlapping of plasmon resonances associated with the different materials in the trimer. The general principle was demonstrated in a point dipole model, and the effect was evaluated using numerical simulation of structures with realistic and experimentally achievable dimensions. The proposed structure enables significantly increased field enhancement factors and consequently efficient and localized heat generation. The relative absorption coefficient of a gold nanoparticle in a heterogeneous Ag-Au-Ag trimer was found to exceed that of isolated gold nanoparticles by two orders of magnitude. The structure potentially allows heterogeneous plasmonic trimers to be used in photothermal applications at significantly reduced laser irradiance, and may enable the investigation of thermal effects and thermally assisted chemical effects on ultrashort time scales.

6. PHOTOTHERMAL NONLINEAR RESPONSE ENHANCEMENT IN HETEROGENEOUS PLASMONIC TRIMERS

6.1. Introduction

Nanoscale heat generation in metallic nanoparticle clusters under optical irradiation has received enormous attention due to the ability of plasmonic nanostructures to introduce large and extremely localized thermal gradients in a wide variety of host materials. Pulsed laser excitation of metallic nanoparticles produces an abrupt temperature rise inside the metallic nanoparticle and its immediate environment. This temperature rise introduces several photothermal and optoacoustic phenomena which can be used in bubble formation [74, 75, 146, 147], selective cell targeting [40, 148], optoacoustic imaging [34], nano-welding [43, 44] and photo-thermal modulation [149, 150]. Temperature changes inside the nanoparticles modify the electronic and physical structure of the metallic nanoparticles which in turn changes the dielectric function of the nanoparticles. The modification of the dielectric function due to the optical absorption and the associated temperature changes, known as the thermo-optic effect, leads to a modification in the often large optical absorption or scattering of plasmonic nanostructures. The small size of plasmonic structures and the localized nature of the heating on the other hand enables rapid changes in temperature. These two factors together make plasmonic structures and composites a promising tool in fast thermo-optical applications such as optical modulation, nanoscale bubble generation and thermally assisted chemical reactions.

In recent years, researchers have studied several ways of enhancing heat generation in plasmonic nanostructures. For example, Baffou and his co-workers found that the shape of isolated

gold nanoparticles affects the efficiency of heat generation [151]. In other studies it was also shown that patterned nanoholes in metal films can efficiently enhance the heat generation due to the larger interface of the metal with the environment [152]. Govorov *et al.* showed that the amplified field in the gap of a gold dimer can lead to three times larger heat generation in the smaller gold nanoparticle in the gap compared to that of the isolated one [153]. In addition to enhancement of the magnitude of the heat generation, spatial manipulation of heat generation was achieved by varying the illumination wavelength and angle of incidence in gold dimers [154], and by leveraging Fano-type resonances in complex nanostructures [155].

In Chapter 5 we demonstrated that heterogeneous plasmonic trimer structures composed of a gold nanoparticle between two silver nanoparticles can produce a heat dissipation densities that exceed that of isolated gold nanoparticles by two orders of magnitude. In this Chapter, we numerically investigate the thermal nonlinear optical response of such plasmonic nanostructures using combined full-field three-dimensional electromagnetic and transient thermal calculations. In particular, it is shown that in addition to the strength of the field enhancement and the magnitude of the heat dissipation, the specific location where heat is generated has a major impact on the attainable temperature changes, the heating and cooling rates, and the magnitude of the thermo-optic response. Our results demonstrate that the thermo-optic response of properly designed heterogeneous trimers under pulsed illumination is 44 times larger than that of isolated gold nanoparticles. The thermal relaxation time of these trimer structures is less than a nanosecond, suggesting that 1 GHz optical modulation rates can be achieved based on the thermal nonlinear optical response of plasmonic heterogeneous trimers.

6.2. Results

To evaluate the thermo-optic response of plasmonic nonlinear absorbers, we used a combination of three-dimensional frequency domain finite integration simulations [156] and time domain finite integration simulations [157]. We first consider three representative nanostructures: an isolated 10 nm diameter gold nanosphere, a dimer composed of two 80 nm diameter silver nanospheres, and a heterogeneous trimer structure composed of a 10 nm diameter gold nanosphere located between two 80 nm diameter silver nanospheres, all assumed to be embedded in water (n=1.33). The edge-to-edge spacing between adjacent nanoparticles is set to 5 nm. Linearly interpolated literature data was used for the dielectric function of silver [158], while a polynomial fit to literature data was used for gold [103].

The total energy deposition in a nanoparticle is linearly related to its optical absorption cross-section. To calculate the absorption cross-section of a given particle *i*, we first calculate the absorbed power P_i in particle i given by

$$P_i(\boldsymbol{\omega}) = \int_{V_i} Q(\boldsymbol{r}, \boldsymbol{\omega}) \, dr^3, \tag{6.1}$$

where $\boldsymbol{r}$ is the position, $\boldsymbol{\omega}$ is the angular frequency and $Q(\boldsymbol{r}, \boldsymbol{\omega})$ is the frequency dependent power dissipation density which can be obtained from the calculated electric field distributions $\boldsymbol{E}(r, \boldsymbol{\omega})$ using the relation:

$$Q(\mathbf{r}, \boldsymbol{\omega}) = \frac{1}{2} \, \omega \, \varepsilon_i''(\omega)\varepsilon_0 \, \mathbf{E}^*(\mathbf{r}, \boldsymbol{\omega}) \cdot \mathbf{E}(\mathbf{r}, \boldsymbol{\omega}), \tag{6.2}$$

where ω is the angular frequency, ε_i'' is the imaginary part of the dielectric function of material i, and ε_0 is the vacuum permittivity. We obtain the total absorption cross-section σ_{abs} of a trimer using the relation $\sigma_{abs}(\omega) = \sum_i P_i / I$ where I is the irradiance used in the simulation and where the summation runs over all particles in the trimer. Similarly we can also determine the *fractional absorption cross-section* $\sigma_{abs,Au}$ of the gold nanoparticle, which relates the power dissipated in the gold particle P_{Au} to the irradiance as $\sigma_{abs,Au}(\omega) = P_{Au}/I$. The structures are illuminated by light propagating along the z-direction with the electric field amplitude E_0 polarized along the x-axis, corresponding to polarization along the dimer and trimer axes respectively.
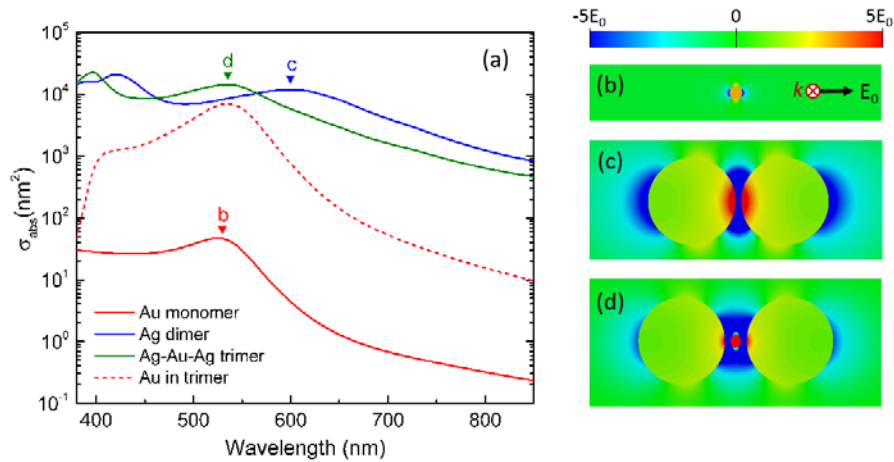
Figure 6.1: a) Absorption cross section spectra for a 10 nm diameter gold monomer (red solid line), a dimer composed of 80 nm diameter silver particles with gap of 5 nm (blue solid line) and a heterogeneous trimer composed of a 10 nm diameter gold nanoparticle between two 80 nm diameter silver nanospheres (green solid line). The dashed red line represents the fractional absorption cross-section $\sigma_{abs,Au}$ of the gold nanoparticle in the trimer structure. Electric field distribution for b) the gold monomer, c) the silver dimer, and d) the heterogeneous trimer, illuminated at the wavelengths indicated in (a).

Figure 6.1(a) shows the calculated absorption cross-section spectrum of the three different structures determined from the simulated electric field distributions. The absorption cross-section of the 10 nm diameter gold monomer (red line) shows a single absorption peak at 530 nm. Figure 6.1(b) shows a snapshot of the x-component of the simulated electric field distribution for the Au monomer at the peak wavelength in the plane normal to the light propagation direction. The field distribution is indicative of the well-known dipolar plasmon resonance mode, resulting in an electric field enhancement factor of 1.9 and consequently large optical dissipation. The cross-

section spectrum of the dimer composed of two 80 nm diameter silver particles (Figure 6.1(a), blue line) shows two peaks located at 420 nm and 600 nm respectively. Figure 6.1(c) shows the electric field distribution corresponding to the absorption peak at 600 nm. The field distribution is representative of a dipolar plasmon resonance with the fields on each nanoparticle having dipolar character. On other hand, the field distribution under excitation at 420 nm (not shown) reveals a hybridized mode where the fields on each nanoparticle having mixed multipolar and dipolar character. The appearance of multipolar contributions in this structure is predominantly due to the presence of the neighboring particle, breaking the rotational symmetry of the environment of each particle. The absorption cross-section of the trimer structure (green line) composed of two 80 nm diameter silver particles and a central 10 nm diameter gold particle shows two peaks located at 400 nm and 535 nm respectively. Figure 6.1(d) shows the field corresponding to the absorption peak at 535 nm, revealing a largely dipolar field distribution on each of the three nanoparticles, oscillating approximately in-phase, i.e. the internal electric field in adjacent particles has identical sign. At this excitation frequency the field enhancement in the Au particle is 25. This is a remarkably large value compared to the single particle enhancement factor of 1.9, which is the combined result of field concentration in the dimer gap and a multiplicative cascaded plasmon resonance, in which a high-polarizability resonator excites a smaller resonator without significant loss in quality factor [159]. The large field enhancement achieved in this case leads to a large power dissipation in the gold particle, described by the gold related fractional absorption cross-section $\sigma_{abs,Au}$ (dashed red line in Figure 6.1(a)). The maximum absorption cross-section of the gold particle inside the trimer structure is seen to be enhanced by two orders of magnitude

86

compared to that of the gold monomer. The dramatically enhanced cross-section of the Au nanoparticle suggests that the heterogeneous trimer will exhibit a large thermo-optic response observable as a light-induced change in the absorption cross-section.

In order to evaluate the thermal response of plasmonic structures under pulsed illumination we assume that the electron gas temperature and the lattice temperature of the particles equilibrate within 1 ps [160]. The nanostructures are illuminated by a 1 ps laser pulse at a fluence of 10 nJ/mm². The resulting temperature evolution is determined by numerically solving the heat-diffusion equation,

$$\rho(\boldsymbol{r}).c_p(\boldsymbol{r}).\frac{\partial T(r,t)}{\partial t} = Q(\boldsymbol{r}) + k(\boldsymbol{r})\nabla^2 T(\boldsymbol{r},t), \tag{6.3}$$

where T($\boldsymbol{r}$,t) is the time-dependent temperature distribution, ρ, c_p and k are position dependent density, specific heat capacity and thermal conductivity, respectively, all obtained from literature and assumed to be temperature independent for the pulse energies used and $Q(\boldsymbol{r})$ is the dissipated power density obtained from the simulated field distributions using Equation (6.2). Note that the pulse duration of 1 ps is much longer than the typical plasmon decay time of several fs, and therefore the continuous wave excited field distributions and dissipation distributions here are a good approximation of those obtained under true pulsed illumination. Figure 6.2(a) shows the calculated temperature evolution in the three different nanostructures relative to the background temperature, denoted as ΔT. For the isolated Au nanoparticle excited at 530 nm (Figure 6.2(a). red line) the maximum temperature rise measured at the center of the particle is 0.23 K immediately after the laser pulse (t=1 ps). The evolution of the temperature after the pulse can be well described by a stretched exponential function of the form $\Delta T(t) = \Delta T_0 e^{-(t/\tau)^\beta}$ with τ the 1/e relaxation time

and β a parameter that describes the degree of non-exponentiality [161]. A stretched exponential

fit to the temperature relaxation of the isolated particle yields τ = 14.2 ps.
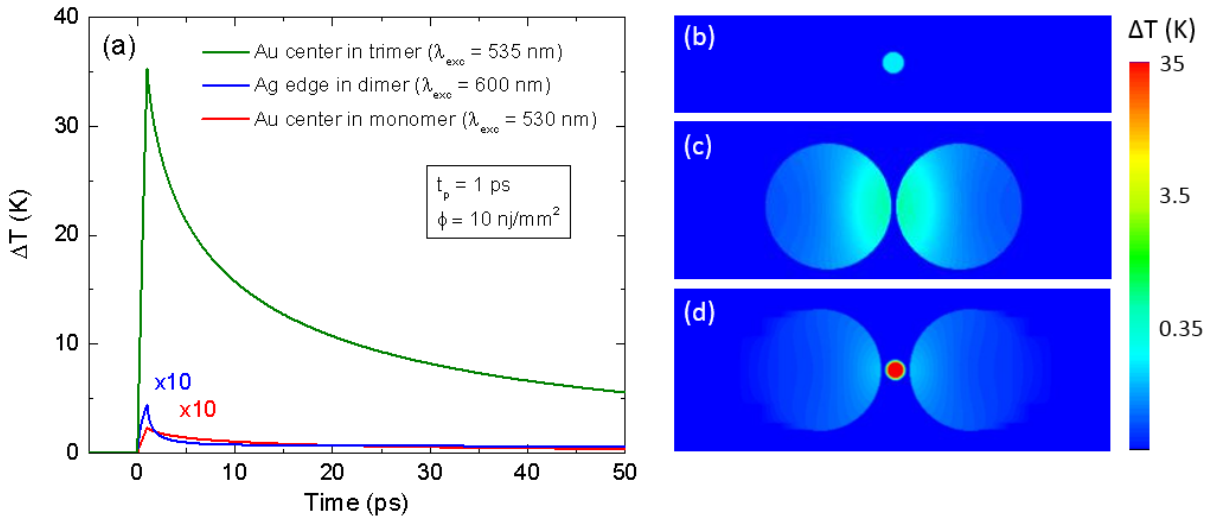
Figure 6.2: (a) Temperature rise inside a 10 nm diameter gold monomer under pulsed laser

illumination with a fluence of 10 nJ/mm2 and a pulse duration of 1 ps at 530 nm (red solid line),

near the surface of a 80 nm silver nanosphere in a dimer structure with a gap of 5 nm at 600 nm

(blue solid line) and inside a gold nanosphere in a heterogeneous trimer structure composed of a

10 nm diameter gold nanoparticle between two 80 nm silver nanospheres at 535 nm (green solid

line). Temperature distribution at t = 1 ps for (b) a gold monomer illuminated at 530 nm, (c) a

silver dimer illuminated at 600 nm and (d) a heterogeneous trimer illuminated at 535 nm.

For the silver dimer structure under excitation at 600 nm the largest temperature changes

occur at the edge of each silver particle near the gap. The blue curve in Figure 6.2(b) represents

the temperature evolution at this location, showing a maximum temperature change of 0.44 K

immediately after the laser pulse. The relaxation time in this case is found to be 0.94 ps, 15 times smaller than observed for the isolated gold nanoparticle. Finally, the temperature evolution at the center of the 10 nm gold nanosphere in the heterogeneous trimer structure excited at 535 nm (green line) shows a maximum temperature rise of 35 K after the 1 ps laser pulse with a relaxation time of 14.4 ps

The extremely short temperature relaxation time in the case of the silver dimer compared to the case of the Au monomer and the Ag-Au-Ag trimer can be understood by considering the optically induced temperature distributions at the end of the laser pulse, as shown in Figure 6.2(b-d). The temperature in the isolated particle (Figure 6.2(b)) is relatively low and homogeneously distributed throughout the particle. The thermal conductivity of gold is much higher than that of water, and consequently the temperature inside the gold nanoparticle will remain relatively homogeneous while cooling of the isolated gold nanosphere is governed by slow heat transfer to the surrounding water. In the case of silver dimer structure on the other hand (Figure 6.2(c)) the temperature distribution is seen to be highly inhomogeneous, due to the stronger optical dissipation near the gap. The initial cooling of the gap region therefore occurs by equilibrating the temperature within the particle, which is mediated by the high thermal conductivity of silver. Once an approximately homogeneous internal temperature distribution is achieved, further cooling takes place via the much slower heat transfer to the surrounding water.

By contrast, in the case of the trimer, immediately after the laser pulse the temperature in the central gold particle is high and relatively homogeneously distributed. In this case no initial internal equilibration takes place, and therefore the thermal relaxation is governed by the relatively slow thermal conduction into the surrounding water. Due to the high specific heat of the water, the

Au nanoparticle temperature decrease is largely determined by the immediate aqueous environment, with the Ag nanoparticles playing only a very minor role in the initial heat redistribution.

The observed large temperature changes in the heterogeneous trimer suggest that a large thermally induced change of the optical response may be achieved. To evaluate the maximum thermo-optic response of these structures under pulsed excitation, we consider the change in optical properties at the maximum achieved temperature, i.e. directly after the pulsed excitation. In order to estimate the maximum thermo optic response, several approximations were made. First, we assume that the bulk thermo-optic coefficients of the materials are valid on a picosecond time scale. In this case the temperature-induced change in the real and imaginary index is given by

$$\Delta n = \frac{dn}{dT}\Delta T \quad and \quad \Delta \kappa = \frac{d\kappa}{dT}\Delta T, \tag{6.4}$$

where dn/dT and dκ/dT are the first-order real and imaginary thermo-optical coefficients of the material. For time varying temperature distributions, determining the photo-thermal response would require coupled time domain electromagnetic and thermal calculations, i.e. considering a different refractive index distribution for each time step, and repeating this for each excitation wavelength of interest. To simplify this process, here we determine an upper limit to the induced photothermal response by assuming that the laser-induced temperature change inside the each nanoparticle is homogeneous and equal to the maximum internal temperature ΔT reached after pulsed excitation. This is a good approximation for the Au nanoparticles, however it will significantly overestimate the response of the silver dimer due to the highly inhomogeneous temperature distribution in the silver particles (see Figure 6.2(c)). The temperature change inside

90

the gold nanoparticle at each frequency follows the dissipated power spectra due to the fact that the field distribution and consequently the absorbed power distribution inside the gold nanoparticle is similar across the entire simulated frequency range. Consequently, one can predict the temperature change inside the gold particle for all frequencies based on the dissipated power spectra and the simulated temperature change at one frequency. However, the temperature change inside the silver nanoparticle does not follow the dissipated power spectra due to the significantly different field distributions that develop at different frequencies. To evaluate the temperature change inside silver nanoparticles for whole spectra, we therefore calculated the temperature change inside the silver nanoparticle at several key frequencies and used the simulated power dissipation spectra to interpolate the results.

Once the maximum light-induced temperature change has been determined, the thermally modified dielectric function of each material can be obtained from Equation (6.4) using literature data for the thermo-optical coefficients of gold [162] and silver [163] as shown in Figure 6.3.
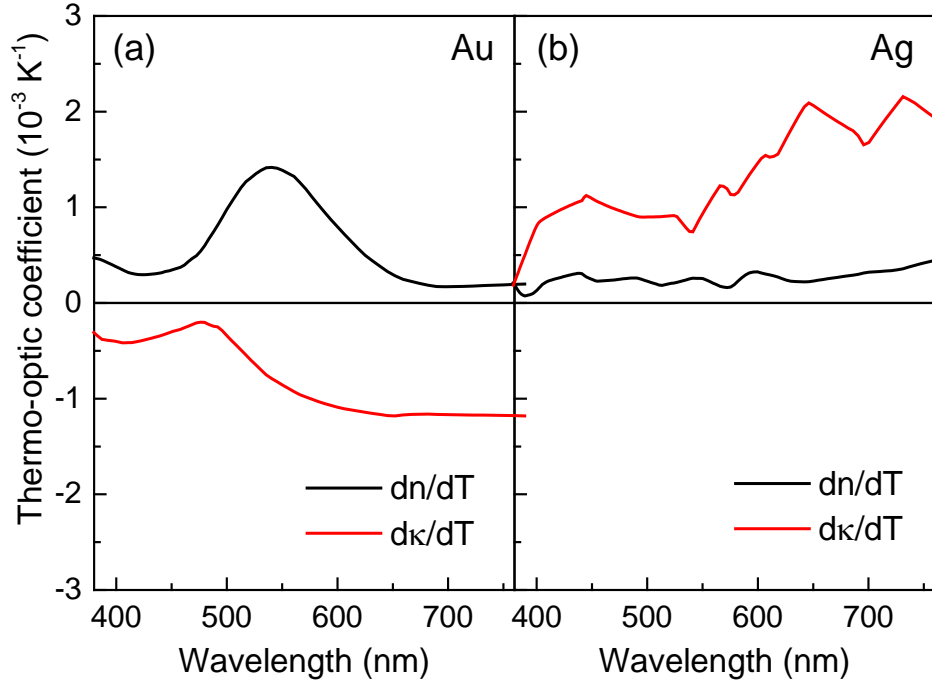
Figure 6.3: Real and imaginary parts of the thermo-optic coefficients for a) gold [162] and b) silver [163].

Repeating the cross-section calculation with these modified dielectric functions provides the wavelength dependent change in absorption cross-section $\Delta\sigma_{abs}$. To describe the nonlinear optical absorption performance of an aqueous suspension of these structures, we define a figure of merit (FOM) as

$$FOM \left(\frac{m^2}{J}\right) = \frac{\Delta\alpha}{\alpha \cdot \phi}, \tag{6.5}$$

where φ (J/m^2) is fluence and $\Delta\alpha$ (m^{-1}) and α (m^{-1}) are the nonlinear change to the absorption coefficient and the linear absorption coefficient, respectively. This parameter is large when a large

relative change in the absorption can be reached at low fluence, and mathematically corresponds to the inverse of the fluence required to obtain a thermal nonlinear absorption equal to the linear absorption for the assumed pulse duration of 1 ps. Since the absorption coefficient is linearly related to the absorption cross-section, the FOM is independent of particle concentration, and is given by $\Delta\sigma_{abs}/(\sigma_{abs}\, \varphi)$. To obtain the FOM spectrum we use the σ_{abs} values obtained in Figure 6.1(a) and the $\Delta\sigma_{abs}$ values calculated as described above. Note that these cross-section values assume that the excitation field is aligned along the dimer or trimer axis. Since the calculated absorption changes represent an upper limit, the obtained FOM values also represent an upper limit.

Figure 6.4 shows the obtained FOM for thermo-optically induced absorption in the silver dimer, the gold monomer, the heterogeneous trimer discussed in detail above, as well as for four additional trimers with varying Au nanoparticle diameters at the same edge-to-edge spacing. The FOM for isolated 10 nm gold nanospheres (purple line, scaled by a factor five) shows saturable absorption (negative FOM) and reverse saturable absorption (positive FOM) below and above the dipolar plasmon resonance wavelength of the isolated gold nanoparticle, respectively. The largest FOM for this structure is 0.043 mm^2/μJ, occurring at a wavelength of 560 nm. The FOM spectrum for the silver dimer structure (gray line) shows saturable and reverse saturable absorption below and above both the largely dipolar mode at 600nm and the hybridized mode at 420 nm, with a maximum magnitude of 0.3 mm^2/μJ at a wavelength of 435 nm, close the silver dimer hybridized mode in the saturable absorption region. The FOM spectrum for the heterogeneous trimer structure (blue line) shows a shape similar to that of the isolated gold nanoparticle. However, the peak FOM

achieved for the multi-material trimer structure is 1.9 mm^2/μJ, a factor 44 larger than that of the isolated gold nanoparticle. This enhancement of the thermal nonlinear optical response is due to the combination of two main factors. First, in the trimer structure a strong field enhancement is achieved inside the gold nanoparticle due to the multiplicative cascading effect, leading to large heat dissipation inside the gold nanoparticle. Second, the short pulse illumination combined with the low thermal conductivity of the surrounding medium (water) allows for large temperature changes with relatively small pulse energies, which in turn enables a large modification of the gold refractive index.
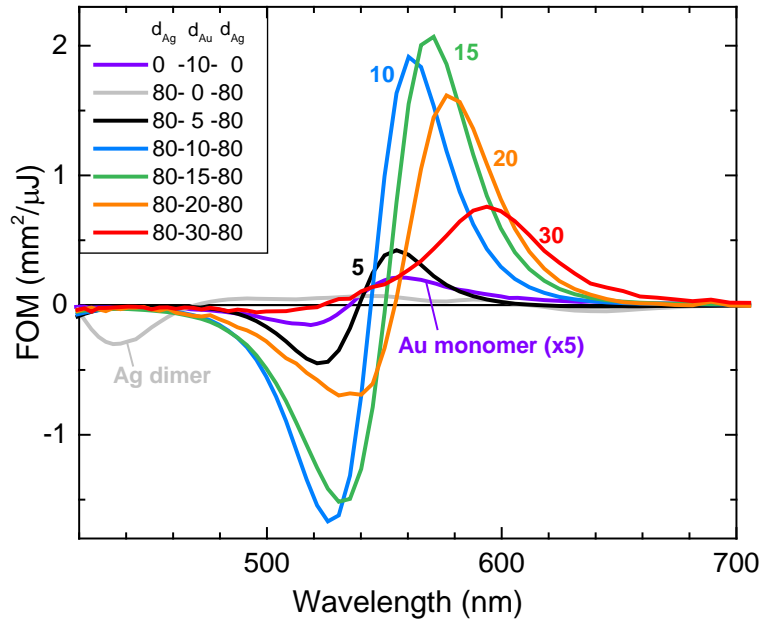
Figure 6.4: Figure of merit for thermo-optically induced absorption of a 10 nm gold monomer, an 80 nm diameter silver dimer structure, and five heterogeneous trimer structures composed of two 80 nm diameter silver particles and central gold nanoparticles with five different diameters of 5, 10, 15, 20, and 30 nm with an edge-to-edge spacing of 5 nm after a 1 ps laser pulse.

Additional FOM spectra were calculated for trimers with Au nanoparticle diameters of 5, 15, 20, and 30 nm while maintaining a 5 nm edge-to-edge spacing between all particles. The spectra all show similar features, with a maximum FOM of 2.07 mm^2/μJ observed for the trimer with a gold nanoparticle diameter of 15 nm. The existence of an optimum particle size for obtaining a maximum thermal nonlinear absorptive performance can be explained by considering two factors that play a significant role in determining the thermal nonlinear optical response. The first factor is the temperature change which is strongly dependent on the gold related fractional absorption

95

per unit volume, as explained in detail in Chapter 5. Decreasing the gold nanoparticle size increases the larger field enhancement factors achieved by the cascaded field enhancement effect at smaller volume of the gold particle. This increases the relative absorption per unit volume and therefore the temperature change which in turn increases the optically induced change in the gold dielectric function as the gold particle volume is reduced. The second factor is the volume dependent contribution of the gold nanoparticle to the total absorption cross-section. As the gold particle volume is reduced its contribution to the total absorption cross-section of the trimer reduces. Consequently, large optically induced changes in its dielectric properties will only weakly affect the total absorption spectrum, resulting in a vanishing FOM for small nanoparticle sizes. The optimum gold particle size for large thermal nonlinear absorption thus occurs for a particle size that is small enough to enable a strong field enhancement and a large temperature change, while being big enough to significantly affect the total absorption coefficient. The observed effect is not limited to the use of gold and silver specifically, and can be extended to clusters containing multiple particle shapes, sizes, and compositions.

6.3. Summary

In summary, we have investigated the thermal nonlinear optical response of plasmon resonant gold monomers, silver dimers and heterogeneous trimers using full-field electromagnetic and transient thermal simulations. It was shown that the attainable temperature change, the related thermal nonlinear optical response, and the response time of these structures depend not only on the maximum field enhancement factors, but also on the spatial distribution of the achieved

temperature changes and the thermal conductivity of the immediate surroundings. It was demonstrated that the figure of merit for thermo-optically induced absorption of a heterogeneous trimer structure is 44 times larger than that of an isolated gold nanoparticle. In addition, response times smaller than nanosecond were observed, making these structures a promising tool in fast thermo-optical applications like nanoscale bubble generation, optical signal modulation and heat assisted catalysis. Finally, extraordinarily large temperature changes as high as 35 K at a fluence as small as 10 nJ/mm^2 were predicted, making these structures of interest for low-power photothermal applications.

7. SUMMARY AND OUTLOOK

In summary, we used analytical and numerical methods to investigate the linear and nonlinear optical response of media containing coupled metallic nanoparticles. First we studied the linear response of coupled nanoparticles, especially the achievement of larger field enhancement factors in mono-material and multi-material coupled nanoparticles. Using these large field enhancement factors through careful engineered coupled nanoparticles, we studied the Kerr-type nonlinear and thermal nonlinear optical responses in the coupled plasmonic nanostructures.

In Chapter 2, we used a point dipole model to evaluate cascaded field enhancement in asymmetric silver nanosphere dimers. Field enhancement spectra were evaluated as a function of the particle size difference and inter-particle spacing. We observed three distinct regimes of cascaded field enhancement: hindered cascading, multiplicative cascading, and the ultimate cascading limit, depending on the dimer interaction strength. In the limit of weak-mutual coupling, analytical formulas were derived for the ultimate internal and external field enhancement factors in coupled nanosphere dimers. For silver dimers in a host with index 1.5 we obtain a maximum internal field enhancement of 2.9×10^3, a factor of 75 larger than that of an isolated silver nanoparticle. We show in chapter 4 how this coupling effects in asymmetrical mono-material dimer can be used to enhance the Kerr-type nonlinear response. We used a finite integration method and effective medium theory to discuss linear and nonlinear optical responses of a plasmonic metamaterial consisting of closely spaced nanoparticles with different sizes. We observed that the effective nonlinear optical absorption of such asymmetrical cascaded plasmonic nanostructures can be controlled by interplay between different plasmon resonance modes and

depends strongly on the volume ratio of adjacent nanoparticles as well as interparticle spacing between them. We show the attainable nonlinear susceptibility enhancement factors and figure of merit for nonlinear absorption can be increased in a cascaded plasmonic nanostructure consisting of metals with a positive imaginary third order nonlinear optical susceptibility. We observe a large *positive* enhancement factor in the cascaded nanostructure, despite, the imaginary or negative nature of that in the arrays containing a single particle size. This type of phase-optimized design of the nonlinear optical response enhancement in cascaded plasmon resonant metamaterials could lead to the development of new optical switching materials with a performance that dramatically exceeds that of their non-cascaded counterparts.

In Chapter 3, we demonstrate cascaded plasmon resonances in dimer nanoantennas consisting of near-field coupled ellipsoidal particles with identical thickness using analytical model and finite integration method. We used the identical thickness for nanoparticles to show that the cascaded plasmon resonances, described in Chapter 2, can be achieved in the nanostructures which are compatible with common top-down nanofabrication methods such as electron beam lithography and nano-imprint lithography. The field enhancement was evaluated as a function of the particle volume ratio and spacing, and shows the strongest cascaded field enhancement for the largest volume ratio. The largest field enhancement factors that can be achieved in the ultimate cascading limit are 5.7×10^3 for the internal field enhancement factor and 2.6×10^4 for the external field enhancement factor.

In Chapters 2-4, we studied the cascaded field enhancement and related nonlinear optical response in mono-material asymmetrical dimer and effective medium. We discussed the

limitations to achieve cascaded field enhancement in a dimer structure consisting of two nanoparticles with identical material. In Chapter 5, we describe the linear optical response of a heterogeneous plasmonic trimer structure to overcome these limitations. We analytically and numerically discuss the optical response of multi-material plasmonic trimer structures composed of a silver nanoparticle dimer and a central gold nanoparticle. We used a point dipole model to demonstrate the general principle and then used finite integration method to evaluate the cascaded field enhancement factors in a realistic and experimentally achievable dimensions. The resulting coupled plasmon resonance in the heterogeneous trimer structure is found to lead to an enhanced energy dissipation per unit volume which exceeds that of a single-particle system by two orders of magnitude which enables heterogeneous plasmonic trimers to be used in photothermal applications at significantly reduced laser irradiance, and may enable the investigation of thermal effects and thermally assisted chemical effects on ultrashort time scales. In Chapter 6, we discussed the applicability of described trimer structure in Chapter 5 in enhancing the thermal nonlinear optical response. We used frequency and time-domain finite integration method to investigate the transient thermal behavior and related thermal nonlinear optical response of the heterogeneous plasmonic nanostructures under short pulse laser illumination. We demonstrate that in addition to the magnitude of the field enhancement and related heat dissipation, the specific location where heat is generated has a major impact on the attainable temperature changes and thermo-optic response. It is shown that the thermal nonlinear optical response of properly designed heterogeneous trimer structures is 44 times larger than that of isolated gold nanoparticles.

The methods and results of this study can be extended to future research areas. Synthesizing and optically characterizing multi-material, multi-dimensional trimer structures and observing the

predicted effects is of great interest for photothermal applications. Chemical synthesis of these structures could lead to rapid and low-cost production of large quantities of these structures without the need for costly and time-consuming techniques such as electron beam lithography. In addition, new material combinations may be explored. Our work focused on gold and silver nanospheres, however trimers and other oligomers with different materials could extend the useful frequency range and possibly further improve field enhancement. These structures may also provide a new way to investigate fast temperature-dependent dynamics in metallic nanoparticles such as photoluminescence. The proposed cascaded structures may also be used for photo-thermal imaging and low-power photothermal therapy, based on the large temperatures that can be achieved at remarkably low pulse power. Finally, the structures may open new opportunities as a Surface Enhanced Raman Spectroscopy (SERS) platform because of the large predicted field enhancement factors. The small amount of gold used in these structures suggests that these trimers may provide a relatively low gold fluorescence background in SERS measurements, however more research is needed to verify this. Finally, it may be possible to selectively functionalize the central gold particle in the trimer structure in order to bind molecules of interest, potentially allowing for sensitive SERS measurements with a large signal to noise ratio.

APPENDIX A: IRRADIANCE-DEPENDENT REFRACTIVE INDEX

Kerr-type optical nonlinearity

An accurate description of light matter interaction in the presence of the strong optical fields requires the use of higher order electric susceptibilities in describing polarization. In this case the time dependent nonlinear polarization can be represented by a power expansion of the electric field and higher order susceptibilities as shown in Equation (A.1) [3],

$$\boldsymbol{P}(t) = \varepsilon_0\big[\chi^{(1)}\boldsymbol{E}(t) + \chi^{(2)}\boldsymbol{E}(t)\boldsymbol{E}(t) + \chi^{(3)}\boldsymbol{E}(t)\boldsymbol{E}(t)\boldsymbol{E}(t)\big] \qquad (A.1)$$

where $\chi^{(m)}$ are the mth order of the nonlinear susceptibilities which generally are $(m+1)^{th}$ rank tensors. Here the use of bold fonts indicates that the parameter is vectorial in nature. It should be noted that the definition in Equation (A.1) is applicable if the polarization at time t depends only on the instantaneous value of the electric field strength. This implies that the medium must be considered lossless and dispersionless and consequently the susceptibilities should be considered constant. In lossy and dispersive media, the material does not respond instantaneously to the electric field. In this case the susceptibilities become frequency-dependent complex quantities.

In macroscopically centrosymmetric and isotropic media the second order nonlinear susceptibility is zero, making the third order response the lowest-order nonlinear term. If we consider only nonlinear interactions that produce a polarization response at the same frequency as the incident field, necessary for nonlinear absorption and nonlinear refraction, the expression for the field-dependent polarization under illumination with a single monochromatic linearly polarized wave becomes

$$\boldsymbol{P}(\omega) = \varepsilon_0\left[\chi^{(1)}\boldsymbol{E}(\omega) + 3\chi^{(3)}|\boldsymbol{E}(\omega)|^2\boldsymbol{E}(\omega)\right] = \varepsilon_0\,\chi_{tot}\boldsymbol{E}(\omega) \qquad (A.2)$$

where $\chi^{(3)}$ represents the complex third-order nonlinear susceptibility, $\chi_{iiii}^{(3)}(\omega;\omega,\omega,-\omega)$. The factor 3 appears due to intrinsic permutation and is related to the fact that we cannot discriminate between $\chi_{iiii}^{(3)}(\omega;\omega,\omega,-\omega)$, $\chi_{iiii}^{(3)}(\omega;\omega,-\omega,\omega)$, and $\chi_{iiii}^{(3)}(\omega;-\omega,\omega,\omega)$ due to the undistinguishable resultant electric fields. In Equation (A.2), $\chi_{tot} = \chi^{(1)} + 3\chi^{(3)}|\vec{E}(\omega)|^2$ represents the total susceptibility of the material containing both linear and nonlinear terms. In general $\chi^{(1)}$ is a second rank tensor with up to $3^2 = 9$ unique nonzero terms and $\chi^{(3)}$ is a fourth rank tensor with up to $3^4 = 81$ unique nonzero terms. In this report, we consider isotropic materials, reducing the $\chi^{(1)}$ tensor to a scalar quantity and limiting the number of nonzero $\chi^{(3)}$ tensor elements to 21, of which only 3 are independent.

The second term in Equation (A.2) shows that the induced polarization in a nonlinear medium depends on the square of the electric field which leads to an irradiance-dependent refractive index in the presence of the strong optical fields which can be expressed as

$$\eta = \eta_0 + \eta_2 I, \qquad (A.3)$$

where η_0 and η_2 are the complex linear and nonlinear refractive index respectively. The complex nonlinear refractive index, η_2, follows from the third-order nonlinear susceptibility $\chi^{(3)}$, as discussed below. This expression neglects higher order nonlinear refractive index contributions originating from susceptibilities $\chi^{(5)}$ and higher that could lead to refractive index dependencies of

the order I^2 and higher. The complex refractive index in Equation (A.3) can be rewritten in the corresponding real part and imaginary part. The real part is given by

$$n = n_0 + n_2 I, \tag{A.4}$$

where n_0 and n_2 are the linear and the nonlinear refractive index respectively. Typically, optically induced changes of the real part of the refractive index, $n_2 I$, are called the optical Kerr effect, by analogy with the traditional Kerr electro-optic effect. The imaginary part of the nonlinear refractive index on the other hand leads to an irradiance-dependent absorption contribution, resulting in a total absorption coefficient of the form

$$\alpha = \alpha_0 + \beta I \tag{A.5}$$

where α_0 is the linear absorption coefficient given by $\alpha_0 = 2k_0\kappa_0$, in which k_0 is the wavevector in free space and κ_0 is the imaginary part of the linear refractive index. Analogously, β is the nonlinear absorption coefficient given by $\beta = 2\,k_0\,Im[\eta_2]$.

For media with negligible linear absorption, or $\alpha_0 \sim 0$, the real part of the nonlinear refractive index n_2 and the nonlinear absorption coefficient β are proportional to the real and imaginary part of third-order nonlinear susceptibility [3, 164]. The relation between the complex refractive index η and the total susceptibility follows from the relation $\eta^2 = 1 + \chi$ leading to

$$\eta^2 = (n_0 + \eta_2 I)^2 = 1 + \chi_{tot} = 1 + \chi^{(1)} + 3\chi^{(3)}\left|\vec{E}(\omega)\right|^2. \qquad \text{(A.6)}$$

By writing out the index squared term and separately equating terms that depend to the same order on the irradiance I, we obtain the following equations,

$$n_0{}^2 = 1 + \chi^{(1)}$$

$$\qquad \text{(A.7)}$$

$$2n_0\eta_2 I = 3\chi^{(3)}\left|\vec{E}(\omega)\right|^2.$$

The term proportional to I^2 is zero because nonlinearities higher than the third order have been ignored in this analysis. The second equation will lead to the equations below by using the relation between I and $|E(\omega)|^2$, $I = 2n_0 \varepsilon_0 c |E(\omega)|^2$ where $E(t)$ is considered to be of the form $E(\omega) e^{-i\omega t} +$ *c.c.* [3].

$$n_2 = \frac{3}{4n_0^2\varepsilon_0 c} Re\left[\chi^{(3)}\right]$$

$$\qquad \text{(A.8)}$$

$$\beta = \frac{3\pi}{\lambda_0 n_0^2 \varepsilon_0 c} Im\left[\chi^{(3)}\right]$$

Here ε_0, c and λ_0 are permittivity, light velocity and light wavelength in the free space, respectively.

In absorbing systems, the nonlinear absorption and refraction are each dependent on both the real and the imaginary parts of the first- and third-order susceptibilities. In this case, the relation between the nonlinear refractive index and the third order susceptibility in the SI unit system is given by [165]

$$n_2 = \frac{3}{4(n_0^2 + \kappa_0^2)\varepsilon_0 c} Re\left[\left(1 + i\,\frac{\kappa_0}{n_0}\right)\chi^{(3)}\right]$$

(A.9)

$$\beta = \frac{3\pi}{\lambda_0(n_0^2 + \kappa_0^2)\varepsilon_0 c} Im\left[\left(1 + i\,\frac{\kappa_0}{n_0}\right)\chi^{(3)}\right].$$

Photo-thermal nonlinearity

Thermal nonlinear optical effects can also lead to an irradiance-dependent refractive index, but, in contrast with Kerr-type effects, not to higher harmonic generation at optical frequencies. In thermal nonlinear optical materials, the temperature change due to the absorption incident light can lead to a modification of the refractive index. To first order the real and imaginary parts of the refractive index can be expressed as

$$n = n_0 + \frac{dn}{dT}\Delta T$$

(A.10)

$$\kappa = \kappa_0 + \frac{d\kappa}{dT}\Delta T,$$

where n_0 and κ_0 are the real and imaginary index before the temperature change ΔT and dn/dT and dκ/dT are the thermo-optic coefficients of the material. For a known dissipated power density Q the temperature change can be determined by solving the heat transfer equation

$$\rho \cdot c_p \cdot \frac{\partial T(t)}{\partial t} = Q + k\nabla^2 T(t), \qquad (A.\,11)$$

where T(t) is the time-dependent temperature distribution, ρ, c_p and k are density, specific heat

capacity and thermal conductivity, respectively, and Q is given by αI where α is the absorption

coefficient of the material and I is the intensity of the illumination laser.

APPENDIX B: LOCALIZED SURFACE PLASMONS

Field Enhancement

To understand the physics of the field enhancement, we consider a homogeneous, isotropic sphere of radius R located in a uniform electric field $\mathbf{E} = E_0\,\mathbf{z}$, as shown in Figure B.1. This nanosphere embedded in an isotropic and non-absorbing material with dielectric constant of ε_h, and the electric field lines are parallel to the z-direction at sufficient far distance from the sphere. The dielectric function of the metal sphere is described by $\varepsilon_m(\omega)$ which is a frequency-dependent complex number.
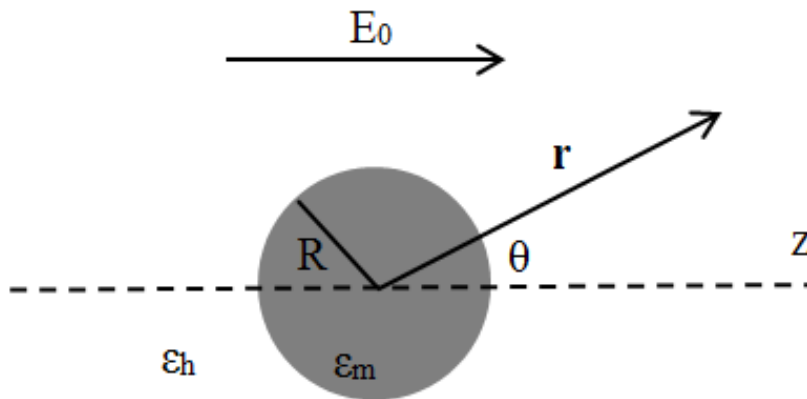
Figure B. 1: Sketch of a homogeneous sphere placed into an electrostatic field.

To calculate the electric field from the electric potential φ using $\mathbf{E} = -\nabla\varphi$, one needs a solution of the Laplace equation for the potential, $\nabla^2\varphi = 0$, satisfying the following boundary conditions. The external electrical potential, φ_{out}, at large distance from the particle must be $E_0 r\cos(\theta)$. In addition the internal and external electrical potential, φ_{in} and φ_{out}, should have the same value at the sphere surface, $r = R$. Finally the tangential component of the electric field and

the normal component of the electric displacement must be continuous at the particle surface. After applying these boundary conditions and solving equations for potentials, the electric field can be evaluated [106]. This leads to the following expressions for the internal and external electric field,

$$\mathbf{E_{in}} = \frac{3\varepsilon_h}{\varepsilon_m(\omega) + 2\varepsilon_h} \mathbf{E_0}$$

$$\mathbf{E_{out}} = \left(1 + 2\frac{\varepsilon_m(\omega) - \varepsilon_h}{\varepsilon_m(\omega) + 2\varepsilon_h} \frac{R^3}{|z|^3}\right) \mathbf{E_0}.$$

(B.1)

The corresponding external electric field on the metal nanoparticle surface at $|z| = R$ along the incident field direction is given by

$$\mathbf{E_{out}}(R\,\hat{z}) = \frac{3\varepsilon_m(\omega)}{\varepsilon_m(\omega) + 2\varepsilon_h} \mathbf{E_0}.$$

(B.2)

where $\hat{z}$ is the unit vector in the incident field direction. A dipolar resonance occurs at frequencies where the dominator in Equation (B.1) or (B.2) becomes minimum, or $\varepsilon_m(\omega) \approx -2\varepsilon_h(\omega)$. At this condition, known as the localized plasmon resonance frequency, both internal and external electric fields will be enhanced. The ratio of the plasmon enhanced electric field and the incident electric field is called the *field enhancement factor* in plasmonic nanostructures.

The model described above is correct in the quasi-electrostatic regime using the Drude model for the dielectric function of the metal. However, this model ceases to be valid when the size of nanoparticle becomes either too large or too small. In the large nanoparticle case, phase retardation leads to the excitation of higher order plasmon modes while the skin depth limits the

penetration of the electromagnetic field into the particle. On the other hand, when the nanoparticle size becomes similar to or smaller than the electron mean free path, the electron scattering rate Γ that is used in the Drude model to describe dissipative loss increases due to an additional electron scattering rate from the surface of nanoparticle. This effect can be described by introducing an additional damping term in the Drude model. The damping contribution related to surface scattering is approximately given by [166],

$$\Gamma_s = A \frac{v_f}{R} \tag{B.3}$$

where $v_f = 1.39 \times 10^6$ m/s is the Fermi velocity in silver[167] and A is a constant which is dependent on the electron scattering mechanism and has been experimentally determined to be of order 1 for small silver nanospheres [168].

Near-field interactions

This Thesis focuses on the optical response of structures composed of individual metal nanoparticles that interact through far-field and near-field coupling. To understand the basic types of interactions between these nanoparticles, we first consider coupled nanospheres that have a diameter much smaller than the wavelength of the exciting light, and that can approximately be described as electric point dipoles. Throughout this Thesis full-field numerical simulations are also carried out that include all the discussed coupling effects. The electric field at position r from a point dipole can be described by [169]

$$E(r) = \frac{1}{4\pi\varepsilon_0\varepsilon_h}\left[k^2(\hat{r}\times p)\times\hat{r}\,\frac{e^{ikr}}{r} + [3\,\hat{r}(\hat{r}.p) - p]\left(\frac{1}{r^3} - \frac{ik}{r^2}\right)e^{ikr}\right] \qquad \text{(B.4)}$$

where $\hat{r}$ is unit vector in the direction of r, r is the magnitude of r and p is the dipole moment. In the case of interacting sub-wavelength particles, two types of electromagnetic coupling can be distinguished: near-field and far-field dipolar interactions. Based on Equation (B.4), for particle spacings r larger than the wavelength of light, far-field dipolar interactions with an r^{-1} dependence dominate. For closely spaced particles, $r << \lambda$, near-field interactions with a distance dependence of r^{-3} dominate. Here, we briefly discuss the manifestations of near-field interactions between coupled nanoparticles. In the following we describe the consequences of inter-particle interaction using particle dimers as an example. Figure B. 2 schematically represents the near-field interaction of two metal nanoparticles for both transverse and longitudinal polarization excitation, where the term 'longitudinal' refers to fields oriented along the dimer axis.
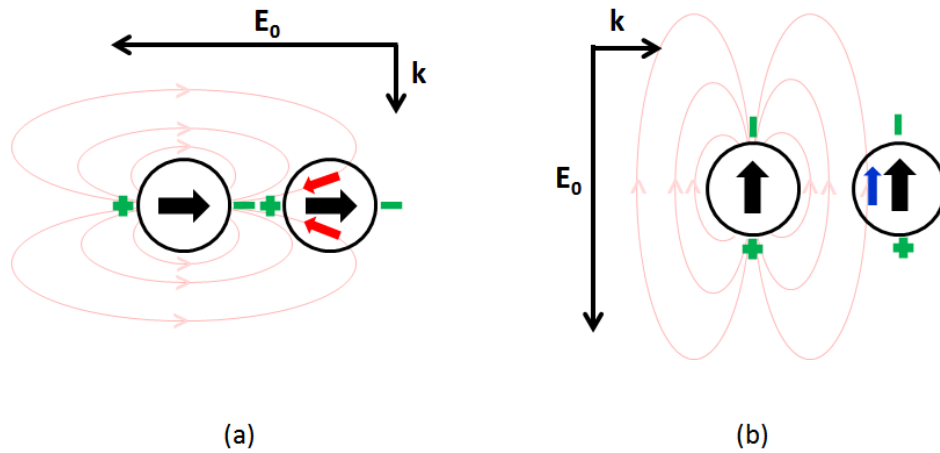
Figure B. 2: Schematic of near-field interaction of two metal nanoparticles for (a) longitudinal and (b) transverse polarization.

In the case of longitudinal excitation (electric field along the dimer axis), the dipolar near-field of the neighbor nanoparticle is opposite in sign compared to the field inside the nanoparticle which leads to a weakened induced polarization and consequently decreased plasmon resonance energy or red-shifted plasmon resonance. For transverse excitation, i.e. plane wave excitation with a field normal to the dimer axis, the dipolar near-field of neighbor metal nanoparticle is equal in sign compared to the induced field inside the nanoparticle which leads to strengthened internal fields and consequently an increased plasmon resonance energy or blue-shifted plasmon resonance. Figure B.3 shows the plasmon resonance wavelength of a dimer consisting of two 20 nm diameter silver nanoparticles for both longitudinal and transverse excitation as a function of the edge-to-edge spacing, calculated using the dipole-dipole interaction model described in Chapter 2.
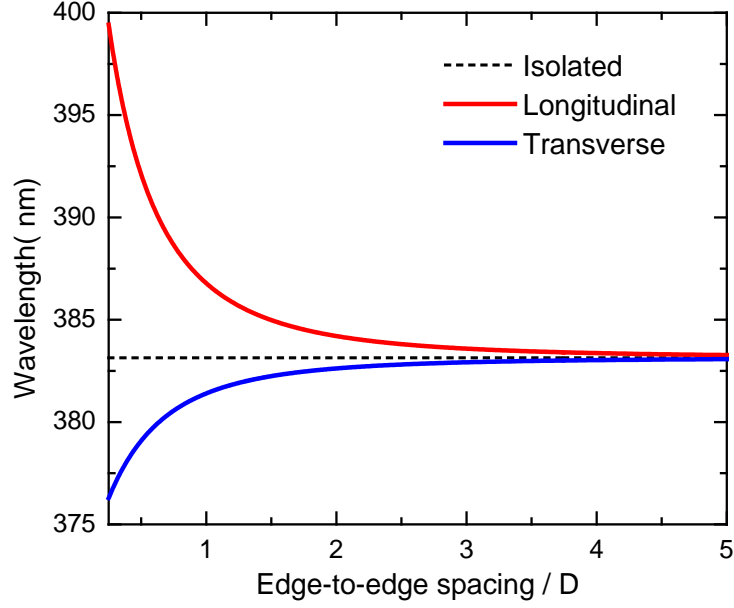
Figure B. 3: Particle spacing dependence of the plasmon resonance frequency for both the longitudinal and transverse modes in a silver dimer structure.

Point Dipole Model

In point dipole model, we consider each nanosphere as a point dipole with a polarizability α_i given by

$$\alpha_i = 3\varepsilon_0 \varepsilon_h \, V_i \, \frac{\varepsilon_m - \varepsilon_h}{\varepsilon_m + 2\varepsilon_h} \tag{B. 5}$$

where V_i, is the volume of nanosphere i. ε_0, ε_m and ε_h are the vacuum permittivity, the dielectric function of the metal and the dielectric function of the host, respectively. The dipole moment of a nanosphere located at position r_i, can be written as

$$\mathbf{p}_i = \alpha_i \mathbf{E}_{loc}(\mathbf{r}_i), \tag{B. 6}$$

where $\mathbf{E}_{loc}(\mathbf{r}_i)$ is the sum of the incident field $\mathbf{E}_{inc}(\mathbf{r}_i)$ and the local electric fields generated by all

the neighbor dipoles at locations $\mathbf{r}_i$, which itself is given by

$$\mathbf{E}_{loc}(\mathbf{r}_i) = \mathbf{E}_{inc}(\mathbf{r}_i) + \mathbf{E}_{dipole,j}(\mathbf{r}_i) = \mathbf{E}_0 \, e^{i\mathbf{k}_i \cdot \mathbf{r}_i} - \sum_{i \neq j} \mathbf{A}_{ij} \mathbf{p}_j, \tag{B. 7}$$

where $\mathbf{A}_{ij} \mathbf{p}_j$ is the electric field contribution of dipole j at the position of dipole i and is given by

$$\mathbf{A}_{ij}\mathbf{p}_j = \frac{e^{ikr_{ij}}}{4\pi\varepsilon_0\varepsilon_h r_{ij}^3} \left[k^2 \mathbf{r}_{ij} \times (\mathbf{r}_{ij} \times \mathbf{p}_j) + \frac{(1 - ikr_{ij})}{r_{ij}^2} \left(r_{ij}^2 \mathbf{p}_j - 3\mathbf{r}_{ij}(\mathbf{r}_{ij} \cdot \mathbf{p}_j) \right) \right] \quad \text{for } i \neq j \quad \text{(B. 8)}$$

where $\mathbf{r}_{ij} = \mathbf{r}_i - \mathbf{r}_j$, $r_{ij} = |\mathbf{r}_{ij}|$ and k is the magnitude of the wavevector in the host medium. For a

dimer structure illuminated with an electromagnetic wave polarized along the dimer axis, as shown

in Figure 2.1, the dipole-dipole interaction matrix, A_{ij}, can be written as

$$A_{12} = A_{21} = \frac{e^{ikd}}{2\pi\varepsilon_0\varepsilon_h} \left(\frac{ik}{d^2} - \frac{1}{d^3} \right), \tag{B. 9}$$

where d is the center-to-center separation of the two nanospheres in the dimer structure.

Substitution of equation (B.7) into equation (B.6) and considering a dimer structure excited with

longitudinal polarization in the quasi-electrostatic regime, leads to

$$p_1 = \alpha_1[E_{inc} - A_{12}p_2]$$

$$p_2 = \alpha_2[E_{inc} - A_{21}p_1]$$

The dipole moment of both nanoparticles can be obtained by solving these two linear equations, leading to

$$p_1 = \alpha_1 \frac{1 - \alpha_2 A_{12}}{1 - \alpha_1\alpha_2 A_{12}^2} E_{inc}$$

$$p_2 = \alpha_2 \frac{1 - \alpha_1 A_{12}}{1 - \alpha_1\alpha_2 A_{12}^2} E_{inc}$$

For a linear trimer structure consisting of two identical outer particles 1 and 3 and excited by light polarized along the trimer axis we have $\alpha_1 = \alpha_3$ and $p_1 = p_3$, and the matrix elements are given by

$$A_{12} = A_{21} = A_{23} = A_{32} = \frac{e^{ikd}}{2\pi\varepsilon_0\varepsilon_h} \left(\frac{ik}{d_{12}^2} - \frac{1}{d_{12}^3} \right)$$

$$A_{13} = A_{31} = \frac{e^{ikd}}{2\pi\varepsilon_0\varepsilon_h} \left(\frac{ik}{d_{13}^2} - \frac{1}{d_{13}^3} \right)$$

where d_{ij} is the center-to-center separation between particles i and j, and k is wavevector in the host medium. The dipole moment of nanoparticle i is thus given by:

$$p_i = \alpha_i[E_{inc} - A_{ij}p_j - A_{ik}p_k]$$

Under these assumptions the dipole moment of each nanoparticle can be obtained by solving these three linear equations,

117

$$p_1 = p_3 = \alpha_1 \frac{1}{1 + \alpha_1 A_{13}} \frac{1 + \alpha_1 A_{13} - \alpha_2 A_{12} - \alpha_1 \alpha_2 A_{12} A_{13}}{1 + \alpha_1 A_{13} - 2\alpha_1 \alpha_2 A_{12}^2} E_{inc}$$

(B. 14)

$$p_2 = \alpha_2 \frac{1 + \alpha_1 A_{13} - 2 \alpha_1 A_{12}}{1 + \alpha_1 A_{13} - 2\alpha_1 \alpha_2 A_{12}^2} E_{inc}$$

Using the known frequency-dependent polarizability, α, of the individual particles, the local electric field in position of each nanoparticle can be determined by $\mathbf{E}_{loc} = \mathbf{p} / \alpha$ and consequently the electric field inside the middle nanoparticle can be obtained by,

$$E_{in,2} = \frac{3\varepsilon_h}{\varepsilon_{m,2} + 2\varepsilon_h} E_{loc,2} = \frac{3\varepsilon_h}{\varepsilon_m + 2\varepsilon_h} \frac{1 + \alpha_1 A_{13} - 2 \alpha_1 A_{12}}{1 + \alpha_1 A_{13} - 2\alpha_1 \alpha_2 A_{12}^2} E_{inc}.$$

(B. 15)

APPENDIX C: NUMERICAL INTEGRATION METHOD

The effective nonlinear response in Chapter 4 was obtained using numerical integration of simulated field distributions. The procedure used is described below. In the presence of an anisotropic metal inside an isotropic host, the local electrical displacement can be written in form of the linear and nonlinear contributions of the susceptibilities.

$$\mathbf{d_i}(r,\omega) = \varepsilon_{ij}(r,\omega)\,\mathbf{e_j}(r,\omega) + \chi_{ijkl}^{(3)}(r,\omega)\,\mathbf{e_j}(r,\omega)\mathbf{e_k}^*(r,\omega)\,\mathbf{e_l}(r,\omega) \qquad \text{(C. 1)}$$

where $\varepsilon_{ij}(r,\omega)$ and $\chi_{ijkl}^{(3)}(r,\omega)$ are the permittivity of anisotropic dielectric constant of the material and the third-order nonlinear susceptibility, respectively. $\mathbf{d_i}(r,\omega)$ and $\mathbf{e_i}(r,\omega)$ are the i$^{\text{th}}$ component of the local electrical displacement and electric field in the position of r and the frequency of ω. The first term is the linear response and the second term represents the nonlinear response. We can define the linear dielectric displacement like)

$$\mathbf{d_{i,L}}(r,\omega) = \varepsilon_{ij}(r,\omega)\,\mathbf{e_j}(r,\omega) \qquad \text{(C.2)}$$

The electrical energy resulting from the linear response inside the composite can be written as

$$W_{i,L}(\omega) = \int \mathbf{e_i}(r,\omega)\cdot\mathbf{d_{i,L}}(r,\omega)\,dV = \sum_m \int \varepsilon_{ij,m}(r,\omega)\,\mathbf{e_i}(r,\omega)\mathbf{e_j}(r,\omega)dV_m \qquad \text{(C.3)}$$

where m represents different components of the composite. In effective medium theory, the electrical energy in a composite with an effective permittivity, $\varepsilon_{ij,c}(\omega)$, is defined as

$$W_{i,L}(\omega) = \int \mathbf{e_i}(r,\omega)\cdot\mathbf{d_{i,L}}(r,\omega)\,dV \equiv \varepsilon_{ij,c}(\omega)\int \mathbf{e_i}(r,\omega)\mathbf{e_j}(r,\omega)\,dV_c \qquad \text{(C.4)}$$

where V_c is the volume of the composite. The effective permittivity constant of the composite can be determined using the Equation (C.3) and Equation (C.4):

$$\varepsilon_{ij,c}(\omega) = \frac{\sum_m \int \varepsilon_{ij,m}(r,\omega) \; \mathbf{e_i}(r,\omega)\mathbf{e_j}(r,\omega)dV_m}{\int \mathbf{e_i}(r,\omega)\mathbf{e_j}(r,\omega) \; dV_c} \tag{C.5}$$

In an isotropic composite, which contains isotropic components in the isotropic distribution, illuminated with a single beam the effective permittivity will be

$$\varepsilon_c(\omega) = \frac{\sum_m \int \varepsilon_m(r,\omega) \; \mathbf{e}(r,\omega)^2 \; dV_m}{\int \mathbf{e}(r,\omega)^2 \; dV_c} \tag{C.6}$$

Now, we just consider the nonlinear part in following calculations. The total electrical displacement for a composite can be defined like

$$\mathbf{d_{i,NL}}(\omega) = \chi_{ijkl}^{(3)}(r,\omega) \; \mathbf{e_j}(r,\omega)\mathbf{e_k}^*(r,\omega) \; \mathbf{e_l}(r,\omega) \tag{C.7}$$

We will omit the position argument in the following calculations. The electrical energy, the nonlinear response contribution, inside the composite can be written as

$$W_{i,NL}(\omega) = \int \mathbf{e_i}(\omega) \cdot \mathbf{d_{i,NL}}(\omega) \; dV = \sum_m \int \chi_{ijkl,m}^{(3)}(\omega) \; \mathbf{e_i}(\omega)\mathbf{e_j}(\omega)\mathbf{e_k}^*(\omega) \; \mathbf{e_l}(\omega) \; dV_m \tag{C.8}$$

where m represents different components of the composite. In addition, according to the effective media, the electrical energy in composite can be defined as

$$W_{i,NL}(\omega) = \int \mathbf{e_i}(\omega) \cdot \mathbf{d_{i,NL}}(\omega) \; dV = \chi_{ijkl,c}^{(3)}(\omega) \int \mathbf{e_i}(\omega)\mathbf{e_j}(\omega)\mathbf{e_k}^*(\omega) \; \mathbf{e_l}(\omega) \; dV_c \tag{C.9}$$

where $\chi^{(3)}_{ijkl,c}(\omega)$ is the effective third-order nonlinear susceptibility of the composite. Using the Equation (C.8) and Equation (C.9), the effective third-order nonlinear susceptibility of the composite can be determined as

$$\chi^{(3)}_{ijkl,c}(\omega) = \frac{\sum_m \int \chi^{(3)}_{ijkl,m}(\omega)\, \mathbf{e_i}(\omega)\mathbf{e_j}(\omega)\mathbf{e_k}^*(\omega)\, \mathbf{e_l}(\omega)\; dV_m}{\int \mathbf{e_i}(\omega)\mathbf{e_j}(\omega)\mathbf{e_k}^*(\omega)\, \mathbf{e_l}(\omega)\; dV} \tag{C.10}$$

Or

$$\chi^{(3)}_{ijkl,c}(\omega) = f g^{(3)}_{in}(\omega)\chi^{(3)}_{ijkl,in}(\omega) + (1-f)g^{(3)}_{h}(\omega)\, \chi^{(3)}_{ijkl,h}(\omega) \tag{C.11}$$

Where f is fill fraction and $g^{(3)}_{in}(\omega)$ and $g^{(3)}_{h}(\omega)$ are the enhancement factor of the third-order nonlinear susceptibility of the metal and host respectively.

$$g^{(3)}_{m}(\omega) = \frac{\int \mathbf{e_i}(\omega)\mathbf{e_j}(\omega)\mathbf{e_k}^*(\omega)\, \mathbf{e_l}(\omega)\; dV_m}{\int \mathbf{e_i}(\omega)\mathbf{e_j}(\omega)\mathbf{e_k}^*(\omega)\, \mathbf{e_l}(\omega)\; dV} \tag{C.12}$$

In an isotropic composites, which consists isotropic elements in an isotropic arrangement, illuminated with a single beam the Equation (C.12) can be rewritten

$$g^{(3)}_{m}(\omega) = \frac{\int |\mathbf{e}(r,\omega)|^2 \mathbf{e}(r,\omega)^2\; dV_m}{\int |\mathbf{e}(r,\omega)|^2 \mathbf{e}(r,\omega)^2\; dV} \tag{C.13}$$

APPENDIX D: LIST OF PUBLICATIONS

1) S. Toroghi, C. Lumdee and P. G. Kik "Photothermal nonlinear response enhancement in heterogeneous plasmonic trimers" to be submitted.

2) S. Toroghi and P. G. Kik "Photothermal response enhancement in heterogeneous plasmon resonant nanoparticle trimers" Physical Review B 90, 205414, 2014.

3) S. Toroghi and P. G. Kik "Cascaded field enhancement in plasmon resonant dimer nanoantennas compatible with two-dimensional nanofabrication methods" Applied Physics Letters 101(1), 013116, 2012.

4) S. Toroghi and P. G. Kik "Cascaded plasmon resonant field enhancement in nanoparticle dimers in the point dipole limit" Applied Physics Letters 100, 183105, 2012.

5) S. Toroghi and P. G. Kik "Cascaded plasmonic metamaterials for phase-controlled enhancement of nonlinear absorption and refraction" Physical Review B 85, 045432, 2012.

6) C. Lumdee, S. Toroghi, and P. G. Kik "Post-Fabrication Voltage Controlled Resonance Tuning of Nanoscale Plasmonic Antennas" ACS Nano 6(7), pp.6301-6307, 2012.

REFERENCES

1. Maiman, T.H., *Optical and Microwave-Optical Experiments in Ruby.* Physical Review Letters, 1960. **4**(11): p. 564-566.
2. Franken, P.A., et al., *Generation of Optical Harmonics.* Physical Review Letters, 1961. **7**(4): p. 118-119.
3. Boyd, R.W., *Nonlinear Optics.* 2003.
4. Lhuillier, A. and P. Balcou, *High-Order Harmonic-Generation in Rare-Gases with a 1-Ps 1053-Nm Laser.* Physical Review Letters, 1993. **70**(6): p. 774-777.
5. Macklin, J.J., J.D. Kmetec, and C.L. Gordon, *High-Order Harmonic-Generation Using Intense Femtosecond Pulses.* Physical Review Letters, 1993. **70**(6): p. 766-769.
6. Hernandez, F.E., et al., *Dual focal plane visible optical limiter.* Journal of Nonlinear Optical Physics & Materials, 2000. **9**(4): p. 423-440.
7. Eggleton, B.J., C.M. deSterke, and R.E. Slusher, *Nonlinear pulse propagation in Bragg gratings.* Journal of the Optical Society of America B-Optical Physics, 1997. **14**(11): p. 2980-2993.
8. Heebner, J.E. and R.W. Boyd, *Enhanced all-optical switching by use of a nonlinear fiber ring resonator.* Optics Letters, 1999. **24**(12): p. 847-849.
9. Johnson, T.J., M. Borselli, and O. Painter, *Self-induced optical modulation of the transmission through a high-Q silicon microdisk resonator.* Optics Express, 2006. **14**(2): p. 817-831.
10. Sheng, Y., S.M. Saltiel, and K. Koynov, *Cascaded third-harmonic generation in a single short-range-ordered nonlinear photonic crystal.* Optics Letters, 2009. **34**(5): p. 656-658.
11. Otto, A., et al., *Surface-Enhanced Raman-Scattering.* Journal of Physics-Condensed Matter, 1992. **4**(5): p. 1143.
12. Kneipp, K., et al., *Single molecule detection using surface-enhanced Raman scattering (SERS).* Physical Review Letters, 1997. **78**(9): p. 1667-1670.
13. Moskovits, M., *Surface-enhanced spectroscopy.* Reviews of Modern Physics, 1985. **57**(3): p. 783-826.
14. Nie, S.M. and S.R. Emery, *Probing single molecules and single nanoparticles by surface-enhanced Raman scattering.* Science, 1997. **275**(5303): p. 1102-1106.
15. Nylander, C., B. Liedberg, and T. Lind, *Gas-Detection by Means of Surface-Plasmon Resonance.* Sensors and Actuators, 1982. **3**(1): p. 79-88.
16. Haes, A.J., et al., *A localized surface plasmon resonance biosensor: First steps toward an assay for Alzheimer's disease.* Nano Letters, 2004. **4**(6): p. 1029-1034.
17. Homola, J., S.S. Yee, and G. Gauglitz, *Surface plasmon resonance sensors: review.* Sensors and Actuators B-Chemical, 1999. **54**(1-2): p. 3-15.
18. Willets, K.A. and R.P. Van Duyne, *Localized surface plasmon resonance spectroscopy and sensing*, in *Annual Review of Physical Chemistry*. 2007, Annual Reviews: Palo Alto. p. 267-297.
19. Hartschuh, A., et al., *High-resolution near-field Raman microscopy of single-walled carbon nanotubes.* Physical Review Letters, 2003. **90**(9).

20.   Frey, H.G., et al., *High-resolution imaging of single fluorescent molecules with the optical near-field of a metal tip.* Physical Review Letters, 2004. **93**(20).

21.   Ishi, T., et al., *Si nano-photodiode with a surface plasmon antenna.* Japanese Journal of Applied Physics Part 2-Letters & Express Letters, 2005. **44**(12-15): p. L364-L366.

22.   Tang, L., et al., *Nanometre-scale germanium photodetector enhanced by a near-infrared dipole antenna.* Nature Photonics, 2008. **2**(4): p. 226-229.

23.   Nikolajsen, T., K. Leosson, and S.I. Bozhevolnyi, *Surface plasmon polariton based modulators and switches operating at telecom wavelengths.* Applied Physics Letters, 2004. **85**(24): p. 5833-5835.

24.   Pacifici, D., H.J. Lezec, and H.A. Atwater, *All-optical modulation by plasmonic excitation of CdSe quantum dots.* Nature Photonics, 2007. **1**(7): p. 402-406.

25.   Cai, W.S., J.S. White, and M.L. Brongersma, *Compact, High-Speed and Power-Efficient Electrooptic Plasmonic Modulators.* Nano Letters, 2009. **9**(12): p. 4403-4411.

26.   Muskens, O.L., et al., *Strong enhancement of the radiative decay rate of emitters by single plasmonic nanoantennas.* Nano Letters, 2007. **7**(9): p. 2871-2875.

27.   Taminiau, T.H., et al., *Optical antennas direct single-molecule emission.* Nature Photonics, 2008. **2**(4): p. 234-237.

28.   Atwater, H.A. and A. Polman, *Plasmonics for improved photovoltaic devices.* Nature Materials, 2010. **9**(3): p. 205-213.

29.   Pala, R.A., et al., *Design of Plasmonic Thin-Film Solar Cells with Broadband Absorption Enhancements.* Advanced Materials, 2009. **21**(34): p. 3504-+.

30.   Boyer, D., et al., *Photothermal imaging of nanometer-sized metal particles among scatterers.* Science, 2002. **297**(5584): p. 1160-1163.

31.   Cognet, L., et al., *Single metallic nanoparticle imaging for protein detection in cells.* Proceedings of the National Academy of Sciences of the United States of America, 2003. **100**(20): p. 11350-11355.

32.   Cognet, L., et al., *Photothermal methods for single nonluminescent nano-objects.* Analytical Chemistry, 2008. **80**(7): p. 2288-2294.

33.   Copland, J.A., et al., *Bioconjugated gold nanoparticles as a molecular based contrast agent: Implications for imaging of deep tumors using optoacoustic tomography.* Molecular Imaging and Biology, 2004. **6**(5): p. 341-349.

34.   Mallidi, S., et al., *Molecular specific optoacoustic imaging with plasmonic nanoparticles.* Optics Express, 2007. **15**(11): p. 6583-6588.

35.   Lal, S., S.E. Clare, and N.J. Halas, *Nanoshell-Enabled Photothermal Cancer Therapy: Impending Clinical Impact.* Accounts of Chemical Research, 2008. **41**(12): p. 1842-1851.

36.   Huang, X.H., et al., *Plasmonic photothermal therapy (PPTT) using gold nanoparticles.* Lasers in Medical Science, 2008. **23**(3): p. 217-228.

37.   Urban, A.S., et al., *Single-Step Injection of Gold Nanoparticles through Phospholipid Membranes.* Acs Nano, 2011. **5**(5): p. 3585-3590.

38.   Skirtach, A.G., et al., *The role of metal nanoparticles in remote release of encapsulated materials.* Nano Letters, 2005. **5**(7): p. 1371-1377.

39.   Timko, B.P., T. Dvir, and D.S. Kohane, *Remotely Triggerable Drug Delivery Systems.* Advanced Materials, 2010. **22**(44): p. 4925-4943.

40. Pitsillides, C.M., et al., *Selective cell targeting with light-absorbing microparticles and nanoparticles.* Biophysical Journal, 2003. **84**(6): p. 4023-4032.

41. Lapotko, D., et al., *Method of laser activated nano-thermolysis for elimination of tumor cells.* Cancer Letters, 2006. **239**(1): p. 36-45.

42. Loo, C., et al., *Immunotargeted nanoshells for integrated cancer imaging and therapy.* Nano Letters, 2005. **5**(4): p. 709-711.

43. Garnett, E.C., et al., *Self-limited plasmonic welding of silver nanowire junctions.* Nature Materials, 2012. **11**(3): p. 241-249.

44. Liu, L., et al., *Highly localized heat generation by femtosecond laser induced plasmon excitation in Ag nanowires.* Applied Physics Letters, 2013. **102**(7).

45. Bozhevolnyi, S.I., J. Beermann, and V. Coello, *Direct observation of localized second-harmonic enhancement in random metal nanostructures.* Physical Review Letters, 2003. **90**(19).

46. Shalaev, V.M. and A.K. Sarychev, *Nonlinear optics of random metal-dielectric films.* Physical Review B, 1998. **57**(20): p. 13265-13288.

47. Simon, H.J., D.E. Mitchell, and J.G. Watson, *Optical Second-Harmonic Generation with Surface Plasmons in Silver Films.* Physical Review Letters, 1974. **33**(26): p. 1531-1534.

48. Wysin, G.M., H.J. Simon, and R.T. Deck, *Optical Bistability with Surface-Plasmons.* Optics Letters, 1981. **6**(1): p. 30-32.

49. Stegeman, G.I., et al., *Nonlinear S-Polarized Surface-Plasmon Polaritons.* Solid State Communications, 1984. **52**(3): p. 293-297.

50. Quail, J.C., J.G. Rako, and H.J. Simon, *Long-Range Surface-Plasmon Modes in Silver and Aluminum Films.* Optics Letters, 1983. **8**(7): p. 377-379.

51. Renger, J., R. Quidant, and L. Novotny, *Enhanced nonlinear response from metal surfaces.* Optics Express, 2011. **19**(3): p. 1777-1785.

52. Sipe, J.E. and R.W. Boyd, *Nonlinear Susceptibility of Composite Optical-Materials in the Maxwell Garnett Model.* Physical Review A, 1992. **46**(3): p. 1614-1629.

53. Ricard, D., P. Roussignol, and C. Flytzanis, *Surface-Mediated Enhancement of Optical-Phase Conjugation in Metal Colloids.* Optics Letters, 1985. **10**(10): p. 511-513.

54. Hache, F., D. Ricard, and C. Flytzanis, *Optical Nonlinearities of Small Metal Particles - Surface-Mediated Resonance and Quantum Size Effects.* Journal of the Optical Society of America B-Optical Physics, 1986. **3**(12): p. 1647-1655.

55. Hache, F., et al., *THE OPTICAL KERR EFFECT IN SMALL METAL PARTICLES AND METAL COLLOIDS - THE CASE OF GOLD.* Applied Physics a-Materials Science & Processing, 1988. **47**(4): p. 347-357.

56. Agarwal, G.S. and S.S. Jha, *Surface-Enhanced 2nd-Harmonic Generation at a Metallic Grating.* Physical Review B, 1982. **26**(2): p. 482-496.

57. Nahata, A., et al., *Enhanced nonlinear optical conversion from a periodically nanostructured metal film.* Optics Letters, 2003. **28**(6): p. 423-425.

58. Airola, M., Y. Liu, and S. Blair, *Second-harmonic generation from an array of sub-wavelength metal apertures.* Journal of Optics a-Pure and Applied Optics, 2005. **7**(2): p. S118-S123.

59. Fan, W., et al., *Second harmonic generation from a nanopatterned isotropic nonlinear material.* Nano Letters, 2006. **6**(5): p. 1027-1030.

60. Lesuffleur, A., L.K.S. Kumar, and R. Gordon, *Enhanced second harmonic generation from nanoscale double-hole arrays in a gold film.* Applied Physics Letters, 2006. **88**(26).

61. van Nieuwstadt, J.A.H., et al., *Strong modification of the nonlinear optical response of metallic subwavelength hole arrays.* Physical Review Letters, 2006. **97**(14).

62. Kim, S., et al., *High-harmonic generation by resonant plasmon field enhancement.* Nature, 2008. **453**(7196): p. 757-760.

63. Xu, T.J., X.J. Jiao, and S. Blair, *Third-harmonic generation from arrays of sub-wavelength metal apertures.* Optics Express, 2009. **17**(26): p. 23582-23588.

64. Genevet, P., et al., *Large Enhancement of Nonlinear Optical Phenomena by Plasmonic Nanocavity Gratings.* Nano Letters, 2010. **10**(12): p. 4880-4883.

65. Hajisalem, G., et al., *Plasmon hybridization for enhanced nonlinear optical response.* Optics Express, 2012. **20**(28): p. 29923-29930.

66. Poutrina, E., et al., *Enhancing four-wave-mixing processes by nanowire arrays coupled to a gold film.* Optics Express, 2012. **20**(10): p. 11005-11013.

67. Kohlgraf-Owens, D.C. and P.G. Kik, *Structural control of nonlinear optical absorption and refraction in dense metal nanoparticle arrays.* Optics Express, 2009. **17**(17): p. 15032-15042.

68. Bouhelier, A., et al., *Near-field second-harmonic generation induced by local field enhancement.* Physical Review Letters, 2003. **90**(1).

69. Danckwerts, M. and L. Novotny, *Optical frequency mixing at coupled gold nanoparticles.* Physical Review Letters, 2007. **98**(2).

70. Lippitz, M., M.A. van Dijk, and M. Orrit, *Third-harmonic generation from single gold nanoparticles.* Nano Letters, 2005. **5**(4): p. 799-802.

71. Pu, Y., et al., *Nonlinear Optical Properties of Core-Shell Nanocavities for Enhanced Second-Harmonic Generation.* Physical Review Letters, 2010. **104**(20).

72. Harutyunyan, H., et al., *Enhancing the Nonlinear Optical Response Using Multifrequency Gold-Nanowire Antennas.* Physical Review Letters, 2012. **108**(21).

73. Li, K., M.I. Stockman, and D.J. Bergman, *Enhanced second harmonic generation in a self-similar chain of metal nanospheres.* Physical Review B, 2005. **72**(15): p. 153401.

74. Vogel, A., et al., *Femtosecond-laser-induced nanocavitation in water: Implications for optical breakdown threshold and cell surgery.* Physical Review Letters, 2008. **100**(3).

75. Lukianova-Hleb, E., et al., *Plasmonic Nanobubbles as Transient Vapor Nanobubbles Generated around Plasmonic Nanoparticles.* Acs Nano, 2010. **4**(4): p. 2109-2123.

76. Lukianova-Hleb, E.Y., et al., *Transient Photothermal Spectra of Plasmonic Nanobubbles.* Langmuir, 2012. **28**(10): p. 4858-4866.

77. Boulais, E., R. Lachaine, and M. Meunier, *Plasma-Mediated Nanocavitation and Photothermal Effects in Ultrafast Laser Irradiation of Gold Nanorods in Water.* Journal of Physical Chemistry C, 2013. **117**(18): p. 9386-9396.

78. Boulais, E., et al., *Plasmonics for pulsed-laser cell nanosurgery: Fundamentals and applications.* Journal of Photochemistry and Photobiology C-Photochemistry Reviews, 2013. **17**: p. 26-49.

79. Neumann, O., et al., *Solar Vapor Generation Enabled by Nanoparticles.* Acs Nano, 2013. **7**(1): p. 42-49.

80. Fang, Z.Y., et al., *Evolution of Light-Induced Vapor Generation at a Liquid-Immersed Metallic Nanoparticle.* Nano Letters, 2013. **13**(4): p. 1736-1742.

81. Cao, L., et al., *Plasmon-assisted local temperature control to pattern individual semiconductor nanowires and carbon nanotubes.* Nano Letters, 2007. **7**(11): p. 3523-3527.

82. Challener, W.A., et al., *Heat-assisted magnetic recording by a near-field transducer with efficient optical energy transfer.* Nature Photonics, 2009. **3**(4): p. 220-224.

83. Liu, G.L., et al., *Optofluidic control using photothermal nanoparticles.* Nature Materials, 2006. **5**(1): p. 27-32.

84. Donner, J.S., et al., *Plasmon-Assisted Optofluidics.* Acs Nano, 2011. **5**(7): p. 5457-5462.

85. S. A. Maier, *Plasmonics: fundamentals and applications.* 2007.

86. Kelly, K.L., et al., *The optical properties of metal nanoparticles: The influence of size, shape, and dielectric environment.* Journal of Physical Chemistry B, 2003. **107**(3): p. 668-677.

87. Microwave Studio, Computer Simulation Technology, Darmstadt, Germany, 2012.

88. Krenn, J.R., et al., *Squeezing the optical near-field zone by plasmon coupling of metallic nanoparticles.* Physical Review Letters, 1999. **82**(12): p. 2590-2593.

89. Li, K., M.I. Stockman, and D.J. Bergman, *Self-Similar Chain of Metal Nanospheres as an Efficient Nanolens.* Physical Review Letters, 2003. **91**(22): p. 227402.

90. Zou, S.L. and G.C. Schatz, *Silver nanoparticle array structures that produce giant enhancements in electromagnetic fields.* Chemical Physics Letters, 2005. **403**(1-3): p. 62-67.

91. Brongersma, M.L., J.W. Hartman, and H.A. Atwater, *Electromagnetic energy transfer and switching in nanoparticle chain arrays below the diffraction limit.* Physical Review B, 2000. **62**(24): p. 16356-16359.

92. Quinten, M., *The color of finely dispersed nanoparticles.* Applied Physics B-Lasers and Optics, 2001. **73**(4): p. 317-326.

93. Sweatlock, L.A., et al., *Highly confined electromagnetic fields in arrays of strongly coupled Ag nanoparticles.* Physical Review B, 2005. **71**(23).

94. Sun, G., J.B. Khurgin, and A. Bratkovsky, *Coupled-mode theory of field enhancement in complex metal nanostructures.* Physical Review B, 2011. **84**(4): p. 045415.

95. Sun, G. and J.B. Khurgin, *Optimization of the nanolens consisting of coupled metal nanoparticles: An analytical approach.* Applied Physics Letters, 2011. **98**(15): p. 153115.

96. Puech, K., et al., *Investigation of the Ultrafast Dephasing Time of Gold Nanoparticles Using Incoherent-Light.* Chemical Physics Letters, 1995. **247**(1-2): p. 13-17.

97. Perner, M., et al., *Optically induced damping of the surface plasmon resonance in gold colloids.* Physical Review Letters, 1997. **78**(11): p. 2192-2195.

98. Inouye, H., et al., *Ultrafast dynamics of nonequilibrium electrons in a gold nanoparticle system.* Physical Review B, 1998. **57**(18): p. 11334-11340.

99. Rashidi-Huyeh, M. and B. Palpant, *Thermal response of nanocomposite materials under pulsed laser excitation.* Journal of Applied Physics, 2004. **96**(8): p. 4475-4482.

100. Schoenlein, R.W., et al., *FEMTOSECOND STUDIES OF NONEQUILIBRIUM ELECTRONIC PROCESSES IN METALS.* Physical Review Letters, 1987. **58**(16): p. 1680-1683.

101. Kravets, V.G., et al., *Cascaded Optical Field Enhancement in Composite Plasmonic Nanostructures.* Physical Review Letters, 2010. **105**(24): p. 246806.

102. Li, K.R., et al., *Surface plasmon amplification by stimulated emission in nanolenses.* Physical Review B, 2005. **71**(11): p. 115409.

103. Johnson, P.B. and R.W. Christy, *OPTICAL CONSTANTS OF NOBLE METALS.* Physical Review B, 1972. **6**(12): p. 4370-4379.

104. Maier, S.A., et al., *Observation of near-field coupling in metal nanoparticle chains using far-field polarization spectroscopy.* Physical Review B, 2002. **65**(19): p. 193408.

105. Toroghi, S. and P.G. Kik, *Design of cascaded plasmon resonances for ultrafast nonlinear optical switching* Proc. SPIE, 2011. **8054**: p. 80540E.

106. Bohren, C.F. and D.R. Huffman, *Absorption and scattering of light by small particles.* 1983, New York: Wiley. xiv, 530 p.

107. Toroghi, S. and P.G. Kik, *Cascaded plasmon resonant field enhancement in nanoparticle dimers in the point dipole limit.* Applied Physics Letters, 2012. **100**(18): p. 183105.

108. Lepeshkin, N.N., et al., *Optical nonlinearities of metal-dielectric composites.* Journal of Nonlinear Optical Physics & Materials, 1999. **8**(2): p. 191-210.

109. Kohlgraf-Owens, D.C. and P.G. Kik, *Numerical study of surface plasmon enhanced nonlinear absorption and refraction.* Optics Express, 2008. **16**(14): p. 16823-16834.

110. Piredda, G., et al., *Nonlinear optical properties of a gold-silica composite with high gold fill fraction and the sign change of its nonlinear absorption coefficient.* Journal of the Optical Society of America B, 2008. **25**(6): p. 945-950.

111. Uchida, K., et al., *Optical Nonlinearities of a High-Concentration of Small Metal Particles Dispersed in Glass - Copper and Silver Particles.* Journal of the Optical Society of America B-Optical Physics, 1994. **11**(7): p. 1236-1243.

112. Kim, K.H., A. Husakou, and J. Herrmann, *Linear and nonlinear optical characteristics of composites containing metal nanoparticles with different sizes and shapes.* Optics Express, 2010. **18**(7): p. 7488-7496.

113. Liao, H.B., W. Wen, and G.K.L. Wong, *Preparation and characterization of Au/SiO 2 multilayer composite films with nonspherical Au particles.* Applied Physics A: Materials Science & Processing, 2005. **80**(4): p. 861-864.

114. Pinçon, N., et al., *Third-order nonlinear optical response of Au:SiO 2 thin films: Influence of gold nanoparticle concentration and morphologic parameters.* The European Physical Journal D - Atomic, Molecular, Optical and Plasma Physics, 2002. **19**(3): p. 395-402.

115. Falcao-Filho, E.L., et al., *Nonlinear susceptibility of colloids consisting of silver nanoparticles in carbon disulfide.* Journal of the Optical Society of America B-Optical Physics, 2005. **22**(11): p. 2444-2449.

116. Maruyama, O., Y. Senda, and S. Omi, *Non-linear optical properties of titanium dioxide films containing dispersed gold particles.* Journal of Non-Crystalline Solids, 1999. **259**(1-3): p. 100-106.

117. Ma, G., et al., *Size and dielectric dependence of the third-order nonlinear optical response of Au nanocrystals embedded in matrices.* Optics Letters, 2002. **27**(12): p. 1043-1045.

118. Jayabalan, J., et al., *Ultrafast third-order nonlinearity of silver nanospheres and nanodiscs.* Nanotechnology, 2007. **18**.

119. Fernandez-Dominguez, A.I., S.A. Maier, and J.B. Pendry, *Collection and Concentration of Light by Touching Spheres: A Transformation Optics Approach.* Physical Review Letters, 2010. **105**(26).

120. Bergman, D.J., *Dielectric-Constant of a 2-Component Granular Composite - Practical Scheme for Calculating the Pole Spectrum.* Physical Review B, 1979. **19**(4): p. 2359-2368.

121. Bergman, D.J., *Dielectric-Constant of a Simple Cubic Array of Identical Spheres.* Journal of Physics C-Solid State Physics, 1979. **12**(22): p. 4947-4960.

122. Zhang, X., et al., *Interparticle coupling effects on plasmon resonances of nanogold particles.* Nano Letters, 2003. **3**(8): p. 1087-1090.

123. Leitner, A., et al., *Optical properties of two interacting gold nanoparticles.* Optics Communications, 2003. **220**(1-3): p. 137-141.

124. Nordlander, P., et al., *Plasmon hybridizaton in nanoparticle dimers.* Nano Letters, 2004. **4**(5): p. 899-903.

125. Wei, A., et al., *Resonant field enhancements from metal nanoparticle arrays.* Nano Letters, 2004. **4**(1): p. 153-158.

126. Nurmikko, A.V., T. Atay, and J.H. Song, *Strongly interacting plasmon nanoparticle pairs: From dipole-dipole interaction to conductively coupled regime.* Nano Letters, 2004. **4**(9): p. 1627-1631.

127. Garcia de Abajo, F.J., S. Riikonen, and I. Romero, *Plasmon tunability in metallodielectric metamaterials.* Physical Review B, 2005. **71**(23).

128. Hohenester, U. and J.R. Krenn, *Surface plasmon resonances of single and coupled metallic nanoparticles: A boundary integral method approach.* Physical Review B, 2005. **72**(19).

129. Aubry, A., et al., *Interaction between Plasmonic Nanoparticles Revisited with Transformation Optics.* Physical Review Letters, 2010. **105**(23).

130. Li, K., M.I. Stockman, and D.J. Bergman, *Li, Stockman, and Bergman Reply.* Physical Review Letters, 2006. **97**(7): p. 079702.

131. Zhang, S., et al., *Plasmon-Induced Transparency in Metamaterials.* Physical Review Letters, 2008. **101**(4): p. 047401.

132. Yannopapas, V., E. Paspalakis, and N.V. Vitanov, *Electromagnetically induced transparency and slow light in an array of metallic nanoparticles.* Physical Review B, 2009. **80**(3): p. 035104.

133. Liu, N., et al., *Plasmonic analogue of electromagnetically induced transparency at the Drude damping limit.* Nature Materials, 2009. **8**(9): p. 758-762.

134. Hao, F., et al., *Tunability of Subradiant Dipolar and Fano-Type Plasmon Resonances in Metallic Ring/Disk Cavities: Implications for Nanoscale Optical Sensing.* Acs Nano, 2009. **3**(3): p. 643-652.

135. Verellen, N., et al., *Fano Resonances in Individual Coherent Plasmonic Nanocavities.* Nano Letters, 2009. **9**(4): p. 1663-1667.

136. Lassiter, J.B., et al., *Fano Resonances in Plasmonic Nanoclusters: Geometrical and Chemical Tunability.* Nano Letters, 2010. **10**(8): p. 3184-3189.

137. Luk'yanchuk, B., et al., *The Fano resonance in plasmonic nanostructures and metamaterials.* Nature Materials, 2010. **9**(9): p. 707-715.

138. Sonnefraud, Y., et al., *Experimental Realization of Subradiant, Superradiant, and Fano Resonances in Ring/Disk Plasmonic Nanocavities.* Acs Nano, 2010. **4**(3): p. 1664-1670.

139. Bachelier, G., et al., *Fano Profiles Induced by Near-Field Coupling in Heterogeneous Dimers of Gold and Silver Nanoparticles.* Physical Review Letters, 2008. **101**(19).

140. Sheikholeslami, S., et al., *Coupling of Optical Resonances in a Compositionally Asymmetric Plasmonic Nanoparticle Dimer.* Nano Letters, 2010. **10**(7): p. 2655-2660.

141. Larsson, E.M., et al., *Nanoplasmonic Probes of Catalytic Reactions.* Science, 2009. **326**(5956): p. 1091-1094.

142. Liu, N., et al., *Nanoantenna-enhanced gas sensing in a single tailored nanofocus.* Nature Materials, 2011. **10**(8): p. 631-636.

143. Shegai, T., et al., *A bimetallic nanoantenna for directional colour routing.* Nature Communications, 2011. **2**.

144. Shegai, T., et al., *Directional Scattering and Hydrogen Sensing by Bimetallic Pd-Au Nanoantennas.* Nano Letters, 2012. **12**(5): p. 2464-2469.

145. Toroghi, S. and P.G. Kik, *Cascaded plasmonic metamaterials for phase-controlled enhancement of nonlinear absorption and refraction.* Physical Review B, 2012. **85**(4): p. 045432.

146. Lapotko, D., *Optical excitation and detection of vapor bubbles around plasmonic nanoparticles.* Optics Express, 2009. **17**(4): p. 2538-2556.

147. Keblinski, P., et al., *Limits of localized heating by electromagnetically excited nanoparticles.* Journal of Applied Physics, 2006. **100**(5).

148. Garwe, F., et al., *Optically controlled thermal management on the nanometer length scale.* Nanotechnology, 2008. **19**(5).

149. Weeber, J.C., et al., *Nanosecond thermo-optical dynamics of polymer loaded plasmonic waveguides.* Optics Express, 2013. **21**(22): p. 27291-27305.

150. Kaya, S., et al., *Photo-thermal modulation of surface plasmon polariton propagation at telecommunication wavelengths.* Optics Express, 2013. **21**(19): p. 22269-22284.

151. Baffou, G., R. Quidant, and C. Girard, *Heat generation in plasmonic nanostructures: Influence of morphology.* Applied Physics Letters, 2009. **94**(15).

152. Baffou, G., C. Girard, and R. Quidant, *Mapping Heat Origin in Plasmonic Structures.* Physical Review Letters, 2010. **104**(13).

153. Govorov, A.O., et al., *Gold nanoparticle ensembles as heaters and actuators: melting and collective plasmon resonances.* Nanoscale Research Letters, 2006. **1**(1): p. 84-90.

154. Baffou, G., R. Quidant, and F.J.G. de Abajo, *Nanoscale Control of Optical Heating in Complex Plasmonic Systems.* Acs Nano, 2010. **4**(2): p. 709-716.

155. Baldwin, C.L., N.W. Bigelow, and D.J. Masiello, *Thermal Signatures of Plasmonic Fano Interferences: Toward the Achievement of Nanolocalized Temperature Manipulation.* Journal of Physical Chemistry Letters, 2014. **5**(8): p. 1347-1354.

156. *Microwave Studio, Computer Simulation Technology, Darmstadt, Germany.* 2013.

157. *Multiphysics Studio, Computer Simulation Technology, Darmstadt, Germany.* 2013.
158. Palik, E.D., *Handbook of Optical Constants of Solids.* Academic Press, New York, 1985.
159. Toroghi, S. and P.G. Kik, *Cascaded plasmon resonant field enhancement in nanoparticle dimers in the point dipole limit.* Applied Physics Letters, 2012. **100**(18).
160. Hodak, J.H., A. Henglein, and G.V. Hartland, *Electron-phonon coupling dynamics in very small (between 2 and 8 nm diameter) Au nanoparticles.* Journal of Chemical Physics, 2000. **112**(13): p. 5942-5947.
161. Hu, M. and G.V. Hartland, *Heat dissipation for Au particles in aqueous solution: Relaxation time versus size.* Journal of Physical Chemistry B, 2002. **106**(28): p. 7029-7033.
162. Rashidi-Huyeh, M. and B. Palpant, *Counterintuitive thermo-optical response of metal-dielectric nanocomposite materials as a result of local electromagnetic field enhancement.* Physical Review B, 2006. **74**(7).
163. Sundari, S.T., S. Chandra, and A.K. Tyagi, *Temperature dependent optical properties of silver from spectroscopic ellipsometry and density functional theory calculations.* Journal of Applied Physics, 2013. **114**(3).
164. R. L. Sutherland, *Handbook of Nonlinear Optics.* 1996.
165. del Coso, R. and J. Solis, *Relation between nonlinear refractive index and third-order susceptibility in absorbing media.* Journal of the Optical Society of America B-Optical Physics, 2004. **21**(3): p. 640-644.
166. Genzel, L., T.P. Martin, and U. Kreibig, *Dielectric Function and Plasma Resonances of Small Metal Particles.* Zeitschrift Fur Physik B-Condensed Matter, 1975. **21**(4): p. 339-346.
167. Ashcroft, N.W. and N.D. Mermin, *Solid State Physics.* 1976.
168. Apell, P. and D.R. Penn, *Optical-Properties of Small Metal Spheres - Surface Effects.* Physical Review Letters, 1983. **50**(17): p. 1316-1319.
169. J .D. Jackson, *Classical electrodynamics.* 1999.